The Role of Surfactants in Jet Break-Up for Inkjet Printing

Evangelia Antonopoulou

Declaration

The candidate confirms that the work submitted is her own, except where work which has formed part of jointly authored publications has been included. The contribution of the candidate and the other authors to this work has been explicitly indicated below. The candidate confirms that appropriate credit has been given within the thesis where reference has been made to the work of others.

The work presented in chapter 3 resulted in the following publication:

Antonopoulou, E., Harlen, O. G., Walkley, M. A., & Kapur, N. (2020). Jetting behavior in drop-on-demand printing: Laboratory experiments and numerical simulations. *Physical Review Fluids*, 5(4), 043603. https://doi.org/10.1103/PhysRevFluids.5.043603

I am the principal author of this paper. I ran simulations with the code presented in Morrison and Harlen (2010) and conducted experiments in Ricoh UK, Telford. I discussed the idea with my supervisors, Dr Oliver Harlen, Dr Mark Walkley and Prof Nikil Kapur, who provided guidance and comments on the drafts.

The work presented in chapter 5 has been submitted for publication:

Antonopoulou, E., Harlen, O. G., Rump, M., Segers, T., & Walkley, M. A. (2020). The effect of surfactants on jet break-up in drop-on-demand inkjet printing. *Journal of Fluid Mechanics*

I am the principal author of this paper. I ran simulations with the code presented in this thesis and conducted experiments in Physics of Fluids group in University of Twente. Maaike Rump and Dr Tim Segers contributed on the experimental part of the work. I discussed the idea with my supervisors, Dr Oliver Harlen, Dr Mark Walkley, who provided guidance and comments on the drafts, as well as Maaike Rump and Dr Tim Segers.

To my mum, Elena...

Acknowledgements

First and foremost, I would like to thank my supervisor Oliver Harlen for his continuous support throughout my studies. He was always there to hear my questions and thoughts and provided me with excellent and valuable feedback, even if it required a bit of a nudge. His constant encouragement to attend meetings and conferences helped me develop my presentational and networking skills. Oliver's guidance during my PhD helped me as a researcher and will be remembered throughout my academic career.

I also want to thank my co-supervisors Mark Walkley and Nik Kapur. Mark's computational skills and availability to answer all of my FORTRAN questions was pivotal to my development and gave me confidence in aiming for optimisation in numerics. Nik's intuition and physical understanding of fluid dynamics gave a different perspective to my research. Without him, I would not be able to interact with my experimental collaborators effectively.

A big thank you to my industrial collaborator Ricoh and the inkjet printing lab in Telford, more specifically Martin Ball, Helen Zhou and Ling He. Everyone in the lab made my trips to Telford the easiest they could be, both professionally and personally. Ricoh's support throughout the project gave me the opportunity to work within a world-leading company. I enjoyed being a part of the research and development department and doing some interdisciplinary cutting-edge research.

Peter Jimack was very important, he believed in me and offered support towards any of my concerns during my time with the CDT. For this, I thank him. His support motivated me to try new things and this helped to establish collaborations with universities and leading groups both inside and outside UK. This work was supported by the UK Engineering and Physical Sciences Research Council Centre for Doctoral Training in Fluid Dynamics at the University of Leeds under Grant No. EP/L01615X/1. I would also like to thank UK Fluids Network, UKFN Special Interest Group in Droplets and the Hellenic Society of Rheology for aid in attending multiple national and international conferences.

During my one-month research visit to Physics of Fluids group in University of Twente, I worked with Maaike Rump and I would like to thank her as well as Tim Segers and Detlef Lohse for their hospitality. Our inspiring conversations, insight and integration of their experimental data with my work, gave us the opportunity to consider different aspects of inkjet printing with surfactants. The group provided me a social and friendly environment to work within and I thoroughly enjoyed my

time in the Netherlands thanks to all the students in the group.

I want to thank my mentor and friend Kostas Housiadas from the University of the Aegean for his constant support since my undergraduate studies. He helped me not only in my research but gave me opportunities to attend and organise conferences from which I met future collaborators and leading experts in our field. Our discussions always give me motivation to do more and hopefully one day, we will work on something together.

Finally, I would like to thank my family for their love and support during this up-and-down and sometimes stressful period of my life. Last but not least, my crew in Leeds who have made my time there a truly amazing and unforgettable experience.

Thank you.

Abstract

Surfactants are often present in fluids used in inkjet printing technology. There is therefore a need to develop a better understanding of the mechanisms underlying the surfactant transport and their effect on the drop formation and jet break-up, in the inkjet printing timescales, which are usually less than a microsecond.

The effects of surfactants are modelled by introducing a surface tension force in the boundary condition at the free surface that depends upon the surfactant concentration, which in turn requires an additional equation for the surfactant transport at the surface. This transport equation is coupled with a surface tension isotherm, which captures the dependence of the surface tension on the surfactant concentration.

The diffusion of the surfactants on the interface is relatively slow compared to new surface generation and the advection of surfactants by surface flows. As a consequence, surfactants become localised to the front of the ejected fluid with low concentration in the trailing ligament. This non-uniformity of the surfactants along the droplet interface gives rise to surface tension gradients and therefore strong Marangoni forces which have big impact on the jet break-up and drop behaviour.

The strength of the surfactant is defined by how much the surface tension can be reduced depending on the concentration. Our results show that a stronger surfactant can prevent satellite formation for viscous fluids. This is a consequence of the effect the surfactants have on the thinning rate of the jet neck. We investigate the scaling laws for the jet break-up for different surfactant strengths and our results show that the break-off time of the neck increases with an increasing surfactant strength.

All these results are validated with experiments. We use high-speed video experimental observations to capture the subtle changes to the jetting behaviour at the sub-millisecond timescale of the jet break-up.

We also use our model for the surfactant distribution and the surface tension computation to study the effect of surfactants on the oscillation of the drop after break-off. The frequency and decay of these oscillations provide a method for measuring dynamic surface tension. We find an important effect of surfactants on the attenuation of oscillations of droplets, due to the rigidification of the surface. This requires careful interpretation of oscillation results in determining bulk viscosity and surface tension.

Contents

List of Figures

Nomenclature

List of Abbreviations

CDT   Centre for Doctoral Training

CIJ   Continuous Inkjet printing

CMC   Critical Micelle Concentration

DOD   Drop-on-Demand

POF   Physics of Fluids group

Greek Letters

α Mesh refinement parameter

β Surfactant strength

$\boldsymbol{\sigma}$ Stress tensor

Γ Surfactant concentration on the surface

γ Surface tension

γ_p Surface tension of pure solvent

γ_{eq} Equilibrium surface tension

Γ_{eq} Equilibrium concetration of surfactants on the surface

Γ_∞ Maximum packing concentration of surfactants on the surface

κ Mean curvature

Λ_D Depletion depth ratio

μ Dynamic viscosity

Ω_l^* Lamb's angular frequency of the lth oscillation mode

Ω_l	Angular frequency of the lth oscillation mode
ϕ	Velocity basis function
ψ	Pressure basis function
ρ	Density
τ_D	Decay time
τ_l	Diffusion timescale
$\tau_{D,p}$	Planar diffusion timescale
$\tau_{D,s}$	Spherical diffusion timescale

Latin Letters

$\bar{r}$	Average jet neck thickness
ℓ	Mesh resolution parameter
$\mathcal{R}$	Gas constant
$\dot{\jmath}$	Fickian flux
θ	Azimuthal coordinate
$\mathbf{f}$	Unit vector for gravitational force
$\mathbf{n}$	Normal unit vector
$\mathbf{t}$	Tagential unit vector
$\mathbf{u}$	Velocity
A	Surface area
a_l	Instaneous amplitude of lth oscillation mode
B	Dimensionless bulk exchange rate
b	Net flux of surfactants
C	Dimensionless surfactant concentration on the surface
c_M	Molar concentration
c_{bulk}	Surfactant concentration in the bulk

D Surfactant diffusivity

D_s Surfactant surface diffusivity

g Gravitational force

h Depletion depth

h_p Planar depletion depth

h_s Spherical depletion depth

J Surface flux

K ratio of equilibrium to maximum packing surfactant concentration

l Oscillatory mode

L_M Maximum mesh length

L_m Minimum mesh length

N Number of surfactant molecules

N_p Number of pressure nodes

N_u Number of velocity nodes

p Pressure

P_l Legendre polynomial of order l

r Radial coordinate

R_0 Initial radius of the cylinder or droplet

R_N Nozzle radius

$R_{\min}$ Minimum neck radius

S Free surface boundary of the domain

s Arc length along the curve

T Temperature

t Time

t_b Capillary break-off time

T_M Marangoni stress

t_p Pinch-off time

t_R Characteristic timescale of break-up

U Velocity scale

u Radial velocity component

V Region of (r, z) space correspondind to domain

W Work

w Axial velocity component

z Axial coordinate

Chapter 1

Introduction

Inkjet technology has grown beyond printing of images and includes manufacture of displays (Quintans Carou et al., 2007), metals (Lee et al., 2008), ceramics (Ainsley et al., 2002), polymers (Hoath et al., 2007) and more recently printing of biological structures (Mandrycky et al., 2016). A key challenge in developing new applications of inkjet technology is to produce "inks" that can be jetted to form individual droplets reliably (termed "jettable" fluids) to transport the functional components needed for the application. The development of mathematical models that allow fluid jetting behaviour to be determined as a function of fluid properties would allow optimisation to be carried out in-silico before creating the inks and verifying the performance. This would have a huge impact on the speed of development of inks (and print-heads) within industry.

Ink formulations are complex and often contain surface active compounds called surfactants that lower the surface tension. For example, one of the most important application of surfactants in inkjet printing is in bioprinting, an aspiring technology with the goal of building tissues in the laboratory and implantable organs (Roth et al., 2004; Tekin et al., 2008; Tasoglu and Demirci, 2013; Murphy and Atala, 2014). Cellular material has highly non-Newtonian properties that affect jetting. Since surfactants cannot be measured directly in jetting experiments, their distribution must be inferred from their effect on the dynamics. This requires a model that incorporates both the mechanics of surfactant transport coupled to the dynamical effect of surfactants on the underlying flow.

This chapter introduces the jetting mechanisms used in inkjet printing and in particular the droplet formation process. We describe the jetting instability framework which is the base for the jet break-up into droplets. Finally, a brief

introduction of surfactants theory is presented, outlining the basic concepts that our model is based upon.

1.1   Inkjet Technology

In inkjet printing, the printed pattern is progressively built up directly on to the substrate by the deposition of a large number of individual, tiny drops of ink. Each droplet is created and deposited under digital control and hence the pattern printed can be easily adjusted.

Industrial inkjet printing requires precise control of the formation and jetting of small droplets of a liquid ink. A typical industrial drop-on-demand print-head contains hundreds to thousands of nozzles arranged in an array, such that each nozzle can be independently controlled. Nozzle diameters range from 10 to 100 µm in diameter generating drops with volume from 0.5 to 500 pl at speeds typically between 5 and $10 \, \mathrm{m \, s^{-1}}$ (Hoath, 2016; Martin et al., 2008).

There is an increasing fraction of industrial activity that uses inkjet printing in manufacturing as inkjet printing has a number of advantages over direct or contact printing methods. First, the patterns are defined digitally and thus can be represented by digital data files, not as physical master templates and so can be very easily changed. This decreases the set-up costs and times needed. The reliability and robustness of the process is another feature that attracts industry. In inkjet printing, we need to optimise the control we have on the droplet size and speed and the total behaviour of the ejected fluid. The run lengths and the number of repeated copies at which inkjet competes with more conventional process in terms of cost have also increased, as well as the resolution and the quality of the image.

However, there are important limitations to the use of inkjet printing, such as the resolution, precision and material properties. The resolution depends on the size of the printed drop after drying, as well as the deposition precision. This achievable precision is limited not only by the movement of the print head or the substrate, but also by the aerodynamic and electrostatic effects on the drop whilst in flight. The drop placement accuracy is currently approximately several micrometers with a lower size of $\approx 10 \, \mu m$, showing the limit of features that can be printed by a drop-on-demand printer (Hutchings and Martin, 2012). Another important limitation in current inkjet printing technology is the restricted range of fluids properties based upon established 'well behaved' inks. Systematic studies

of printability as a function of fluids properties, such as viscosity, surface tension, molecular concentration and solvent characteristics are necessary in order to widen this range.

Inkjet technology is highly adaptable, allowing different kind of inks and substrate to be used. However, the printing speed is still slow compared with direct printing. Inkjet technology has the potential to revolutionise manufacturing process, if it can be extended to attain the speed and coverage of conventional methods. For that, we need a better understanding of the science behind the formation and behaviour of small liquid drops in any jetting technique, particularly for more complex fluids.

1.1.1 Continuous inkjet method

The *Continuous Inkjet* (**CIJ**) printing method was developed in the 1960s (Hoath, 2016) and it is widely used as the standard equipment in factories worldwide. One of the big advantages of this method is the speed and reliability of printing, however, the quality of the printing is low. Common applications can be found in the printing of barcodes or larger coloured backgrounds, as well as printing "use by" or "best before" dates.

A continuous stream of liquid emerging from a nozzle is inherently unstable and will eventually break up into a stream of droplets under the influence of surface tension forces. This process has been studied by Savart (1833) (Alart et al., 2006) and analysed by Rayleigh (1879). Rayleigh showed that the wavelength of the most rapidly growing disturbance in the jet (and thus the distance between the centres of the resulting drops) was about 4.5 times the diameter of the jet, a phenomenon which is often called the *Rayleigh break-up*. It was first employed as the basis for a CIJ printer by Sweet at Stanford University in the 1960s (Basaran et al., 2013).

Sweet's design suggested the key concept of stimulating jet break-up by modulating it at an appropriate frequency and using electrostatic forces to deflect the drops (Le, 1998). In the modern CIJ printing, the drops to be printed on to the substrate are usually steered electrostatically. Each drop detaches from the end of the continuous stream and then an electric charge is induced on it. When the drop subsequently passes through a fixed electric field, it is deflected by the correct amount to land at the right place on the substrate. In contrast, drops with no charge are arranged to land in a gutter from which the surplus ink can be recovered and recycled back to the nozzle, see figure 1.1. In this way, a stream of drops from a
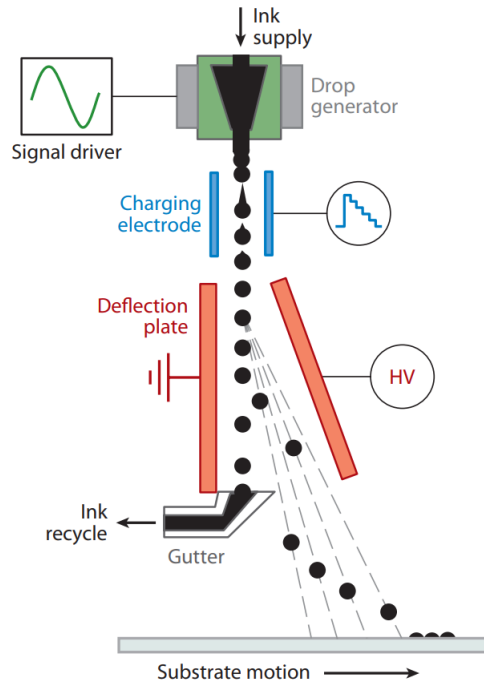
Figure 1.1: Schematic of continuous inkjet printing with the Sweet method. Republished with permission of Annual Reviews, Inc., from (Basaran et al., 2013); permission conveyed through Copyright Clearance Center, Inc.

single nozzle, in combination with a moving substrate, can be used to print a swathe of text or an image.

1.1.2   Drop-On-Demand method

The *Drop-On-Demand* (**DOD**) printing method was developed in the 1970s (Kyser and Sears, 1976; Zoltan, 1972). With this method, much higher resolutions have been achieved compared to CIJ printing and also provided digital reproduction of text and images at low cost in the domestic and small office environment.

In industrial DOD applications, many nozzles, from hundreds to thousands, are arranged in an array in each printhead, with each nozzle contributing to one line of printed drops. The position at which each drop lands on the substrate is controlled by the relative motion between the drop and the substrate and by the timing of the drop ejection, as well as by the selection of the appropriate nozzle from the array.

There are two different methods used to generate the pressure pulse, needed to eject an ink drop: piezoelectric and thermal-based (Hoath, 2016). Here we focus on piezoelectric DOD driving. These printers use a piezolectric ceramic element that changes shape in response to an electric current, creating a pressure pulse via direct
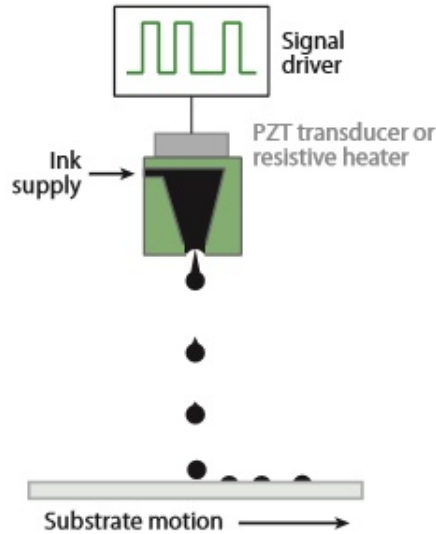
Figure 1.2: Schematic of Drop-On-Demand printing. Republished with permission of Annual Reviews, Inc., from (Basaran et al., 2013); permission conveyed through Copyright Clearance Center, Inc.

mechanical actuation. Other printers use the thermal inkjet method, called bubble jet, where there is an expansion of a small bubble of vapour produced by the action of a small electric heating element on the liquid.

The shape that we commonly observe for a single drop upon its exit is a nearly spherical head with a trailing ligament (Martin et al., 2008). The drop diameters range from 10 to 100 µm with a drop volume from 0.5 to 500 pl. The drop speeds are between 5 to $8\,\mathrm{m\,s^{-1}}$ for DOD printing (10 to $20\,\mathrm{m\,s^{-1}}$ for CIJ printing) (Hoath, 2016).

Drop size and velocity can be varied by using different nozzle sizes but also by using different driving strategies. At a low amplitude of the driving waveform, the ligament pinches off at the nozzle while the head is still close to the nozzle. The droplet that forms due to the capillary contraction of the ligament (tail droplet) has sufficient velocity to catch up the head droplet and merges to form a single drop. At a high amplitude of the driving waveform, the head droplet velocity is too high for the tail droplet to reach the head droplet before the tail breaks up, due to the Rayleigh-Plateau instability. For some applications, such as printing of random patterns on ceramic floor tiles, the presence of satellite droplets (see §1.2.1) is not an issue. However, for functional printing, e.g. conductive wires, satellite droplets are unacceptable.

Therefore, although an increase in the droplet velocity can increase printing accuracy and productivity, it also increases the number of satellite droplets gener-

ated. A challenge in DOD inkjet printing research is to find nozzle geometries and actuation signals that result in fast, accurate deposition of drops without satellite droplets.

1.2 Jet Break-Up and Droplet Formation

1.2.1 Droplet formation in Drop-On-Demand

The jet break-up and drop generation in inkjet printing of a Newtonian fluid are controlled by three fluid properties: the surface tension, the viscosity and the density. Surface tension is crucial to the process: at the first stage the fluid is ejected through a nozzle in a cylindrical shape, however, surface tension drives the break-up of this jet into spherical drops that can be used for printing. This mechanism is known as the *Rayleigh-Plateau* or *capillary instability* (Plateau, 1873; Rayleigh, 1878)

The forces resisting the contraction of a liquid jet into droplets have two origins: the inertia of the liquid and its viscosity. For the simple case of the Newtonian fluids, the frictional resistance to deformation is characterised by a single parameter, the viscosity. However for non-Newtonian fluids, the stress-strain relationship is non-linear and so the viscosity is a function of the deformation rate and also of the accumulated strain experienced by the fluid (Morrison and Harlen, 2010).

Figure 1.3: Comparison of drop formation in axisymmetric simulations and large-scale experiments, where the nozzle diameter is 2 mm. Reprinted figure with permission from Castrejón-Pita et al. (2011) Copyright 2011 by the American Physical Society.

As illustrated in figure 1.3, in DOD jetting, the pressure pulse generates a flow of ink out of the nozzle. The front of this pulse forms into the main drop, which initially is connected to the fluid remaining in the nozzle by a ligament, which is called the tail. The tail connects the droplet with the nozzle until the radius of

the tail decreases to zero somewhere. When the radius decreases to zero near the nozzle or the head droplet, we say that there is a *pinch-off*. The possible subsequent break-up of the tail into smaller drops, called *satellite drops*, is called *tail break-up*.

Assume now that the tail first pinches off at the nozzle, before it pinches off at the head droplet and before it breaks up. The rear end of the tail contracts and forms a droplet, the tail droplet, which advances into the tail. If the head droplet velocity is low enough, the tail droplet merges with the head droplet, sweeping up the entire tail in the process. Hence, all the jetted ink forms into a single spherical droplet. This is usually the desired outcome in inkjet printing.

However, a low droplet velocity is not always acceptable. Increasing the amplitude of the pulse results in a higher drop speed, but also a longer ligament. Since such ligaments are unstable to the Rayleigh-Plateau instability (Plateau, 1873; Rayleigh, 1878) longer ligaments (above a critical aspect ratio) break-up into smaller satellite drops (Hoath et al., 2013). Whilst some, faster moving, satellite drops will catch up and merge with the main drop, satellite drops that do not merge tend not to land at the desired location and so are detrimental to print quality. Even worse, due to the tail break-up, the exact droplet size distribution depends on noise sources, giving a variability between successive drops which is undesirable. Therefore, although increasing the speed of the main drop improves both printing accuracy and productivity, it can also lead to an increase in satellite drop generation. Hence, the challenge in DOD printing is to identify the combinations of print-head design, actuation signals and fluid properties that allow high-speed drop generation with minimal satellite drop generation.

To summarise, the DOD drop formation can be described with the three separate phenomena:

- head droplet formation;

- tail formation;

- pinch-off and tail break-up.

1.2.2   Dimensionless groups in inkjet printing

For Newtonian fluids, the formation of droplets from jets can be characterised by two dimensionless groups comparing the importance of surface tension, viscosity and inertia. These are:

- the *Reynolds number*, Re: the ratio between inertial and viscous forces in a moving fluid,

$$\text{Re} = \frac{\rho U R_N}{\mu},$$

where ρ is the ink density, U is the drop speed, R_N is the nozzle radius and μ is the ink viscosity, and

- the *Weber number*, We: the ratio between inertia and surface tension,

$$\text{We} = \frac{\rho U^2 R_N}{\gamma},$$

where γ is the ink surface tension.

However, these two dimensionless groups can be combined to form a further group, the Ohnesorge number (McKinley and Renardy, 2011), which is independent of drop speed and depends only on the physical properties of the liquid and the dimensions of the jet or the drop,

- *Ohnesorge number*, Oh ,

$$\text{Oh} \ = \frac{\sqrt{\text{We}}}{\text{Re}} = \frac{\mu}{\sqrt{\gamma \rho R_N}} \, .$$

The Ohnesorge number is independent of the driving conditions, which control the velocity. It represents the balance between viscous and inertial forces at the characteristic flow rate driven by surface tension. Therefore, it characterises both the capillary driven break-off of a liquid bridge, which causes the pinch-off of the jet from the nozzle and the Rayleigh-Plateau instability of an infinite jet, which is the key mechanism for satellite drop formation. In particular, Derby (2010) suggests that DOD printing requires the value of the Ohnesorge number to be in the range 0.1 to 1. For Oh > 1, viscosity delays the pinch-off of the jet from the nozzle, while for Oh < 0.1, the ligament will break up to form a large number of satellite droplets. Whilst this criterion is a useful guide in the development of inks, it does not take account of the effects of drop speed on ligament length which in turn affects the formation of satellites (Hoath et al., 2013).
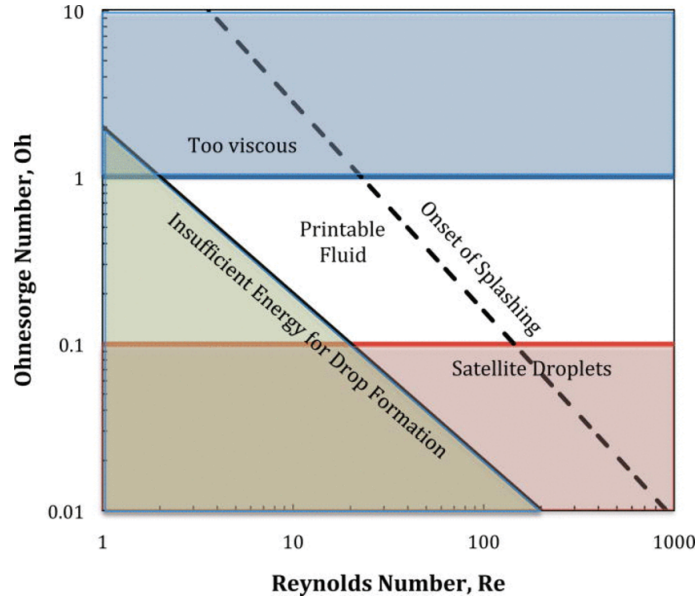
Figure 1.4: Schematic diagram showing the operating regime for stable DOD inkjet printing, in terms of Oh and Re Reprinted from (McKinley and Renardy, 2011) with the permission of AIP Publishing.

Using these dimensionless groups, the conditions for a fluid to be printable can be presented using a phase diagram. A common diagram is the Ohnesorge against Reynolds number diagram, as shown in figure 1.4. When Oh > 1, considered as too high, the viscosity delays the break-off of a drop. When Oh < 0.1, considered as too low, the ligament will break up to form a large number of satellite droplets. In the range in between, there is a satisfactory performance of a fluid in DOD printing since there is an appropriate combination of the physical properties which also depends on the droplet size and velocity (through Re and We).

1.2.3 Jetting instability

The forces at an interface between two media were studied and solved by Laplace (1805) and Young et al. (1805). They showed the importance of mean curvature in the form of the Laplace pressure

$$\Delta p = \gamma \left(\frac{1}{R_1} + \frac{1}{R_2} \right) = \gamma \kappa \,, \tag{1.1}$$

where Δp is the pressure difference across the interface, κ is the mean curvature with R_1 and R_2 being the principle radii of curvature and acts to minimise the interfacial area. From this decomposition of the curvature, we may observe that surface tension can act in two different ways. In the case of a hanging drop, there

is an elastic membrane action which means that surface tension is stabilising and resisting the gravitational force. On the other hand, when the jet forms a cylindrical shape, the radial curvature acts as the driving force to destabilise the free surface and hence leads to the detachment of the drop.

Early experimental work of Savart (1833) in the study of jet break-up showed that the break-up of a jet into droplets occurs spontaneously and is governed by laws independent of the conditions under which the jet is produced, such as nozzle size, jet speed and the amplitude of the initial perturbation. Therefore, the thinning and break-up behaviour is an intrinsic process common to all jets. Another important note from this work is the existence of smaller satellite drops in between the main drops of fluid which is a non-linear characteristic of jet break-up.

The role of surface tension was truly recognised in the full mathematical theory developed by Plateau (1856) and Rayleigh (1878, 1892). Plateau (1856) was first to recognise that small perturbations that reduce the surface area can make the jet unstable and suggested that there exists a critical wavelength below which jets are always unstable. It was Rayleigh (1878) who introduce a method of linear stability analysis in order to quantify the critical wavelength, first for inviscid fluids in a vacuum and a few years later for a viscous cylinder (Rayleigh, 1892). In the case of large perturbations though, the non-linear effects become important and they then dominate the break-up, where Rayleigh's linear stability analysis is no longer valid.

For low Ohnesorge numbers (Oh $\ll$ 1), the fluid viscosity can be neglected and the thinning can be described exclusively from the inviscid dynamics. In the inviscid flow, the pinch-off region takes the form of a double cone due to an overturning profile. This cone has an order one angle and therefore the break-off has to be examined using the full inviscid equations rather than the one-dimensional thin filament approximation. Balancing the surface tension and inertia, with a dimensional analysis, the natural length scale for break-up is given by

$$\left(\frac{\gamma t^2}{\rho}\right)^{1/3},$$

and therefore the *Rayleigh characteristic timescale of break-up* is given by

$$t_R = \sqrt{\frac{\rho R_0^3}{\gamma}}, \tag{1.2}$$

where R_0 is the initial radius of the cylinder (Eggers, 1997). At the pinch point,

the radius of curvature tends to zero and the small amount of fluid left in the pinch region is driven by increasingly strong forces. Hence, the velocity goes to infinity and the separation of a drop corresponds to a singularity of the equations of motion, in which the velocity and gradients of the local radius diverge. Day et al. (1998) derived a similarity solution that has a double-cone shape and the minimum jet radius is given by

$$h_{\min} = 0.7 \left(\frac{\gamma}{\rho}\right)^{1/3} (t_R - t)^{2/3},$$
(1.3)

which is independent of initial conditions. The pinching is also asymmetric occuring near to the end-drops so that a satellite drop is produced at break-up.

For the opposite limit of large Ohnesorge number, Papageorgiou (1995) was first to examine the thinning properties of a viscous thread and obtained an asymptotic solution based on Stokes equations for viscous flow under the slender-jet approximation. The equations are solved numerically and it was shown that the jet radius vanishes after a finite time, with the minimum radius decreasing as

$$h_{\min} = 0.0709 \left(\frac{\gamma}{\mu}\right) (t_R - t).$$

For the case where viscosity, inertia and surface tension are of equal importance, Eggers (1993) has developed a theory for drop formation based on flow close to break-up. Using asymptotics and the long-wavelength description of the jet, he showed that close to the singularity this slender-jet description gives the exact asymptotic representation of the full governing equations. In addition, in the pinch region, the radius and the velocity are expected to obey power laws with some similarity functions. The system has many solutions, which correspond to a discrete sequence of self-similar profiles for increasingly small radii. In order to obtain a unique physical solution, matching to the conditions of the flow away from the singularity is required. Based on numerical simulations, Eggers (1993) suggested that only the first solution in the sequence, which gives the thickest minimum radius is stable. The minimum jet radius predicted from this stable similarity solution is

$$h_{\min} = 0.0304 \left(\frac{\gamma}{\mu}\right) (t_R - t).$$
(1.4)
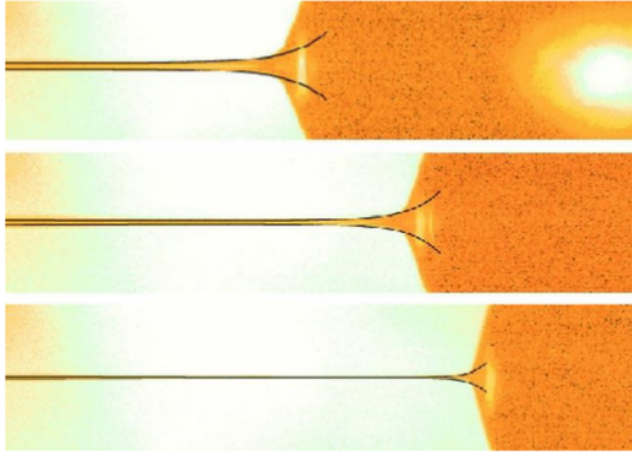
Figure 1.5: A sequence of free-surface profiles of a jet of glycerol close to the point of break-up compared to the self-similar solution (1.4). Reprinted from (Eggers and Villermaux, 2008) with the permission of IOP Publishing.

Figure 1.5 shows that the similarity solution (1.4) appears increasingly elongated, leading to a thin filament connected to the main drop and hence the solution is highly asymmetric, since the steep side merges onto the drop whereas the other takes the form of a thin thread.

Eggers argues that in the final stages of break-up, inertia and viscosity become equally important and so the minimum radius should follow the universal similarity (1.4). However in practice, the length scale at which this occurs for a high viscosity fluid can be less than $1\,nm$ where the continuum approximation no longer holds.

1.3 Surfactants and Dynamic Surface Tension

1.3.1 What are surfactants?

A surface active agent or *surfactant* is a molecule which is characterised by its tendency to adsorb at surfaces and interfaces. They are amphilic, meaning that they consist of at least two parts: a part that is soluble in a specific fluid, the lyophilic or hydrophilic part and an insoluble lyophobic or hydrophobic part. These separate regions are often referred to as the head group and the tail, respectively. At sufficiently high concentrations, surfactants can aggregate into micelles. In a micelle, the hydrophobic group is directed towards the interior of the cluster and the polar head group is directed towards the solvent. By removing hydrophobic

groups from contact with the solvent, the free energy of the system is reduced.

Surfactants are commonly used in chemical formulations. Their versatility makes them very useful in such diverse products as the motor oils found in automobiles, pharmaceutical products, detergents in laundry and house cleaning products, the drilling muds used in prospecting for petroleum and the flotation agents used in benefication of ores. Surfactants influence film thicknesses in coating flows (Quéré, 1999; Shen et al., 2002; Scheid et al., 2010), the dispersion of surface waves (Lucassen and Hansen, 1966), the dynamics and thicknesses of spreading films (Troian et al., 1990; Darhuber and Troian, 2005) and the lifetime of foams and emulsions (Cohen-Addad et al., 2013). In the recent decades, the applications of surfactants have been extended to high-technology areas such as electronic printing, magnetic recording, biotechnology, micro-electronics and viral research (Rosen and Kunjappu, 2012).

Surfactants are classified by the charge of the polar head group, as being anionic, where the head is negatively charged; cationic, where the head is positively charge; non-ionic, where the head is not charged and zwitterionic, where there are separate regions of positive and negative charge within the head group. The hydrophobic part is usually an alkyl chain, which can be linear or branched and whose length is typically between 8 and 18 carbon atoms. The degree of the chain branching, the position of the polar group and the length of the chain are important parameters for the physicochemical properties of the surfactant.

The choice of the surfactant depends on the application and requires knowledge of:

- the characteristic features of the currently available surfactants (general physical and chemical properties),

- the interfacial phenomena involved in the application and the role of the surfactant in these phenomena, and

- the surface chemical properties of the various structural types of surfactants and the relation of the structure of a surfactant to its behaviour in various interfacial phenomena.

Research studies have looked at the effect of surfactants on a range of different flow geometries, including on drop deformation (Eggleton et al., 1999; Milliken et al., 1993; Milliken and Leal, 1994; Stone and Leal, 1990), liquid bridges and threads (Ambravaneswaran and Basaran, 1999; Liao et al., 2004, 2006), filaments

(Kamat et al., 2018), repeated thread formation (Kamat et al., 2018; McGough and Basaran, 2006) and thin film flows (Kalogirou, 2018). In the last decades, there has been an increased focus on the pinch-off (Notz et al., 2001; Craster et al., 2002; Roché et al., 2009). Although these works present mathematical models of the surfactant transport and effect they have on the surface tension, none have considered the effects on inkjet printing.

Another important characteristic of surfactants is their solubility. Soluble surfactants can exist both on the interface and on the bulk. Therefore, when the surfactants behaviour is studied, the constant exchange between bulk and interface needs to be considered. In the insoluble surfactants case, the surfactants only exist on the interface. This behaviour can be observed either by the surfactant nature itself, or when the diffusion and exchange timescales are very small compared to the interface generation. In the latter case, the surfactants act as effectively insoluble. This is seen in the inkjet printing case, see §5.1.2.

1.3.2   Surfactants and surface tension

The interfacial free energy is the minimum amount of work required to expand the interface. The surface or interfacial tension of a liquid is the interfacial free energy per unit area of the boundary between the liquid and the air around it. This is also a measure of the difference in nature of the two phases meeting at the interface (a boundary between any two immiscible phases) or the surface (an interface where one phase is a gas, usually air). The greater the dissimilarity in the interfacial free energy, the greater the interfacial or surface tension. Here we will always refer to this as surface tension.

When an interface is expanded, the minimum work required to create the additional surface area (A) of that interface is the product of the surface tension γ and the increase of the interface; $W = \gamma \times \Delta A$. When surfactants are adsorbed at the surface, they significantly change the amount of work required to expand this surface and usually act to lower the interfacial free energy. Solvent molecules at a surface have higher potential energies than those in the interior, because they interact more strongly with the molecules in the interior of the substance than they do with the wide-spaced gas molecules above, see figure 1.6 Therefore, work is required to bring a molecule from the interior to the surface.

When a surfactant is dissolved in an aqueous solution, the presence of the hydrophobic group may cause a distortion of the water structure by breaking
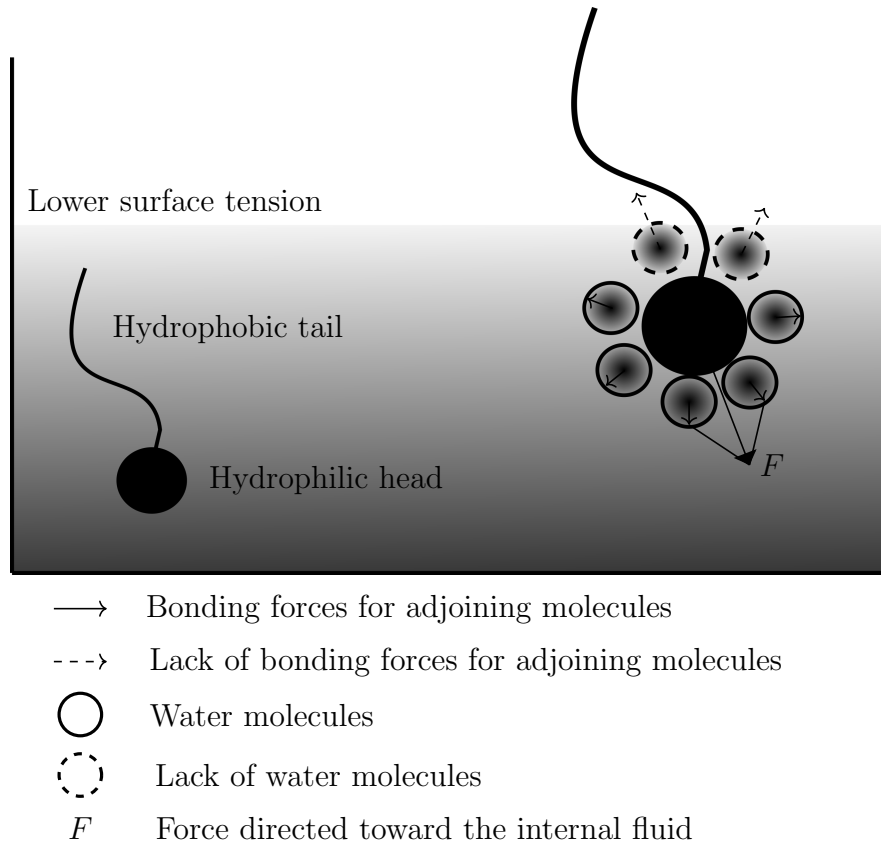
Figure 1.6: Diagram illustrating how surfactants act to lower surface tension.

hydrogen bonds between the water molecules and by structuring the water in the vicinity of the hydrophobic group. Some of the surfactant molecules are expelled to the surface and the hydrophobic groups are oriented in a way to minimise the contact with the water molecules. Then the surface of the water becomes covered with a single layer of surfactant molecules with their hydrophobic groups oriented toward the air. Therefore, the surfactant concentration at the surface is higher than the bulk.

This decrease in the dissimilarity (air molecules and hydrophobic group are non-polar) of the two phases at the surface results in a decrease in the surface tension or, in other words, since less work is now needed to bring molecules to the surface, this decreases the work needed to create a unit area of surface, the surface tension. Note that the presence of the hydrophilic group prevents the surfactant from being expelled completely from the solvent as a separate phase, since that will require dehydration of the hydrophilic group. The amphipathic structure of the surfactant therefore causes:

- concentration of the surfactants at the surface,

- reduction of the surface tension of the water,

- orientation of the molecule at the surface with its hydrophilic group in the aqueous phase and its hydrophobic group oriented away from it.

The surface tension of water with air is relative high compared to that of organic solvents. In order to reduce surface tension in the aqueous inks used for inkjet printing, surfactants are added. Drop formation from an inkjet nozzle leads to the growth and deformation of a liquid-gas interface in less than 1 µs and is faster than the time required for the surfactant molecules to reach an equilibrium distribution. As a consequence, the surface tension can differ from its equilibrium value. This property is often referred to as the *dynamic surface tension* and is a result of the transient adsorption and distribution of surfactant molecules on the interface. There are a variety of methods for measuring dynamic surface tension at liquid-liquid or liquid-gas interfaces (Franses et al., 1996), however many are unsuitable for inkjet printing applications, because they measure changes on too long a timescale. For example, the growing-drop method (Basaran et al., 2013) relies on simultaneously measuring the pressure, $p(t)$, inside and the radius, $R(t)$, of a drop that is grown at the tip of a capillary tube. This method uses the Young-Laplace equation, $p(t) = 2\gamma(t)/R(t)$ and can only measure surface tension, γ, on timescales of milliseconds.

Gradients of surfactant concentration lead to gradients in surface tension that in turn drive flows on the surface. These phenomena are called *Marangoni flows*. The importance of the Marangoni effect depends upon the sensitivity of the surface tension to changes in surfactant concentration and the magnitude of the surface tension in the absence of surfactant, since this controls the maximum possible variation in surface tension over the surface. In liquid-gas or liquid-liquid systems, the surface tension decreases as local surfactant concentration increases.

There are several different transport processes for surfactants that control their local concentration. Surfactants are transported around the free surface through advection by the surface velocity and surface diffusion. In addition, there is also an exchange between surfactant molecules on the surface and those in the bulk. Some approximate model calculations of the physical effects of Marangoni forces are given by Davis and Acrivos (1966); Holbrook and Levan (1983a). However, analytic examples are rare due to the complexity of the surfactant transport problem and the coupling between surfactant transport and fluid motion.

1.3.3 Adsorption at the liquid-gas interface

The determination of the amount of surfactant molecules adsorbed per unit area of liquid-gas interface is difficult since we have to isolate the interfacial region from the bulk phase(s) for purposes of analysis. Hence instead, the amount of material adsorbed per unit area of interface is calculated indirectly from surface measurements. Therefore, a plot of surface tension, γ, as a function of (equilibrium) concentration of surfactant in the liquid phase, c, is generally used to describe adsorption at this interface. Changes to the surface tension at the interface are given by the *Gibbs adsorption equation*:

$$d\gamma = -\sum_i \Gamma_i d\mu_i \,,$$

where $d\gamma$ is the change in surface tension of the solution, Γ_i is the surface excess concentration of solute per unit area of surface or interface ($\mathrm{mol\,cm^{-2}}$) and $d\mu_i$ is the change in chemical potential of the solute in the solution. At equilibrium between the interfacial and bulk phase concentrations $d\mu_i = \mathcal{R}Td\ln a_i$ where $\mathcal{R}$ is the gas constant ($8.314 \times 10^{-7}\mathrm{J\,mol^{-1}\,K^{-1}}$), T is the absolute temperature (K) and a_i is the activity of solute in the solution. Thus

$$d\gamma = -\sum_i \Gamma_i d\mu_i = -\mathcal{R}T\sum_i \Gamma_i d\ln a_i = -\mathcal{R}T\sum_i \Gamma_i d(\ln x_i + \ln f_i)\,,$$

where x_i is the mole fraction of solute in the bulk phase and f_i is its activity coefficient.

For a dilute solution (10^{-2}M or less, where a M=$\mathrm{mol\,l^{-1}}$) containing only one type of non-ionic surfactant (10^{-2}M or less) and no other solutes, the activity coefficient of surfactant can be considered to be constant and the mole fraction can be replaced by its molar concentration, c_M

$$d\gamma = -\mathcal{R}T\Gamma d\ln c_M\,.$$

Hence for the surface tension to be reduced with the addition of a solute (surfactant), then $\Gamma > 0$, i.e. the concentration of the solute at the solution surface is higher than in the bulk liquid.

For a dilute solution containing one ionic surfactant that completely dissociates (A^+B^-), the Gibbs adsorption equation becomes

$$d\gamma = -\mathcal{R}T(\Gamma_A d\ln a_A + \Gamma_B d\ln a_B)\,.$$

and since $\Gamma_A = \Gamma_B$ due to electroneutrality and $a_A = a_B$, we obtain,

$$d\gamma = -2\mathcal{R}T\Gamma d\ln c_b\,.$$

For an ionic surfactant solution in the presence of an electrolyte, e.g. sodium chloride, the Gibbs adsorption equation is

$$d\gamma = -f\mathcal{R}T\Gamma d\ln c_b\,,$$
$$f = 1 + \frac{c_b}{c_b + c_{\text{NaCl}}}\,. \tag{1.5}$$

Hence, in general the surface excess concentration can be determined from the gradient of γ with respect to $\ln c$ at constant temperature as

$$\Gamma = -\frac{1}{f\mathcal{R}T}\frac{\partial \gamma}{\partial \ln c_b}\,, \tag{1.6}$$

where f is equal to one for a non-ionic surfactant and given by Equation (1.5) for an ionic surfactant.

The relationship between the surface concentration Γ and bulk concentration c_b is complex due to the effects of crowding and the formation of micelles. At very low concentrations, Γ is proportional to c_b as the surfactant molecules in the bulk are in monomeric form and there is plenty of room at the free surface.

However, as the surface becomes covered with surfactant, the rate of increase of Γ with c_b decreases, until a maximum surface concentration Γ_∞ is achieved. With equation (1.6) and a proper $\Gamma(c)$ isotherm, we can derive a corresponding surface equation of state $\gamma(\Gamma)$. The most commonly used non-linear isotherm is the Langmuir isotherm (Langmuir, 1918; Chang and Franses, 1995)

$$\Gamma = \frac{\Gamma_\infty c_b}{c_b + a}\,, \tag{1.7}$$

where Γ_∞ is the maximum surface concentration of the surfactant at infinite dilution (mol cm^{-2}); c_b is the surfactant concentration in the bulk (mol l^{-1}), a is a constant$[= 55.3\exp(\Delta G^\circ/RT)]$ (mol l^{-1}), where ΔG° is the free energy of adsorption at infinite dilution. This gives a linear relationship between Γ and c_b at low concentrations but saturates to give $\Gamma \to \Gamma_\infty$ as $c_b \to \infty$.

This is the basis of various empirical formulae relating Γ and c_b, which can be derived by using equation (1.6) and equation (1.7). The more commonly used

ones include,

1. **Szyszkowski equation** (von Szyszkowski, 1908)

$$\gamma = \gamma_p - \mathcal{R}T\Gamma_\infty \ln(1 + ac),$$

   relates surface tension and bulk concentration.

2. **Frumkin equation** (Frumkin, 1925)

$$\gamma = \gamma + \mathcal{R}T\Gamma_\infty \ln\left(1 - \frac{\Gamma}{\Gamma_\infty}\right). \tag{1.8}$$

which are used to fit experimental measurements. In this thesis, we will use the Langmuir-Frumkin surface equation of state (1.8) for the sake of simplicity.

1.3.4 Diffusion and surfactants

The timescales for the surface surfactant concentration to reach equilibrium is governed by the transport, diffusion and adsorption processes occurring in fluid close to the free surface during droplet formation. This timescale can be estimated from the diffusion-limited transport of soluble surfactants from solution onto a planar interface (Eastoe and Dalton, 2000; Liao et al., 2006, 2004). The characteristic timescale for transport via diffusion is given by,

$$\tau_D = \frac{l^2}{D},$$

where l is the distance across which diffusion must occur and D is the diffusion coefficient. Hence the relevant distance is the depletion depth h_p (figure 1.7) which is found by equating the number of molecules accumulated at equilibrium on the interface with the number of molecules of that species available in a volume element of the bulk solution. At equilibrium the number of surfactant molecules adsorbed on a planar area element dA is given by $\Gamma_{eq} \, dA$ where Γ_{eq} is the surface concentration of surfactant in equilibrium. In order to estimate the depletion depth for a bulk concentration c_b, we consider the mass in the volume element dV below the interface $c_b \, dV = c_b \, h_p \, dA$. By equating this expression to the adsorbed molecules, the depletion depth is given by:

$$h_p = \frac{\Gamma_{eq}}{c_b}. \tag{1.9}$$

The depletion depth for common surfactants can be on the order of metres for dilute concentrations of insoluble surfactants and can reduce to between $10^{-5} - 10^{-3}$ m for concentration approaching the critical micelle concentration (CMC) (Ferri and Stebe, 1999).

At higher concentrations, the surface concentration is bounded by the maximum packing concentration Γ_∞ so that h_p varies inversely with bulk concentration. Therefore, the characteristic diffusion timescale $\tau_{D,p}$ decreases as concentration increases and the adsorption time becomes limited by other processes such as the break-up of micelles above CMC.
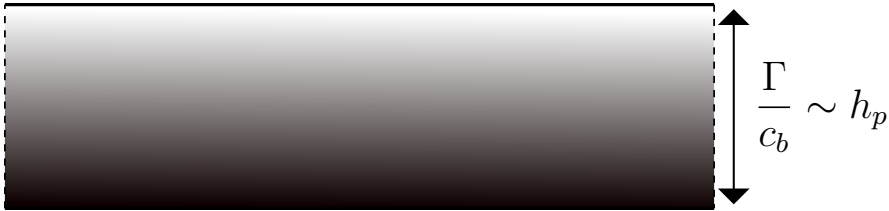
Figure 1.7: Schematic representation of the depletion depth for a planar interface, h_p.

For curved interfaces such as droplets, the diffusion process is also affected by the relative size of the depletion depth to the drop radius R_0,

$$\Lambda_d = \frac{h_p}{R_0} .\tag{1.10}$$

For droplets with radii much larger than the depletion depth ($\Lambda_d \ll 1$), the diffusion timescales the results follow for planar interfaces.

For the case of a bubble of radius R surrounded by a liquid with a dissolved surfactant, Alvarez et al. (2010) and Jin et al. (2004) showed that in the limit $R/h_p \ll 1$ (or $\Lambda_d \gg 1$), that the characteristic timescale for diffusion is given by,

$$\tau_{D,s} = \frac{h_p R}{D} .\tag{1.11}$$

This expression suggests that the diffusion is faster for increasing curvature or smaller radius. This radial dependence of the diffusion-limited timescale can be explained by the fact that the ratio of solution volume to surface area increases with decreasing radius. Hence, a smaller radius bubble reaches equilibrium faster, see figure 1.8. However, in the jetting case where a drop is formed, we have the opposite case: the surfactants are in the interior phase as seen in figure 1.9. In this case, the diffusion process will be slower than for a planar interface as the surfactants will need to diffuse over a distance greater than Γ/c_b in order to resupply the interface.
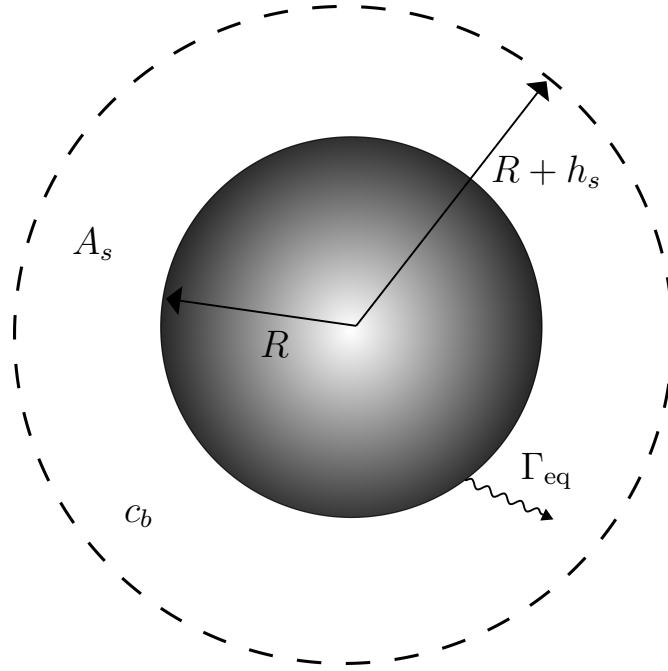
Figure 1.8: Schematic representation of the depletion depth for a spherical interface, h_s.
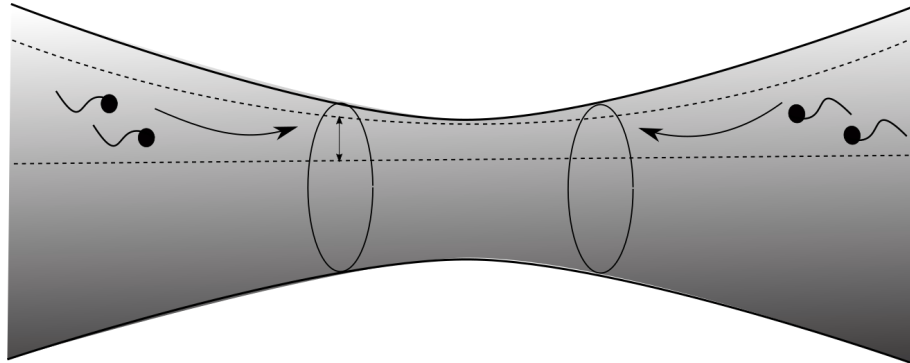
Figure 1.9: Surfactant in a jet and depletion depth in the axisymmetric case.

Therefore the results for a planar interface will be a lower bound on the adsorption timescale.

1.4   Aims and Thesis Outline

The aim of this thesis is to develop a mathematical model to simulate the effect of surfactants on jetting and drop formation in inkjet printing. However before exploring the effects of surfactants, we visit the base case of the DOD jetting of a simple Newtonian fluid with constant surface tension. In chapter 2, we will present the governing equations which form the base for our model and code for the forthcom-

ing surfactant addition. The numerical method and the finite element formulation is also presented.

In chapter 3, we present the results of this numerical model as well as experimental observations for fluids with constant surface tensions. A parameter space for the jetting behaviour given different properties of the fluid is presented as well as well comparison with high-speed video experiments on drop formation in an industrial print-head.

Having established that our model predicts the Newtonian jetting behaviour accurately, we add surfactants to the problem. In chapter 4, we present the governing equations for the surfactant transport and the surface equation of state used along with the finite element formulation and the code adaptations for these additions.

The results from this model are presented in chapter 5, where we study both the surfactant distribution and its effects on the jetting behaviour and jetting properties, such as the thinning rate of the neck.

Finally, we consider the effect of surfactants on the shape oscillation of the main drop once it has detached from the ligament. These oscillations are used experimentally to determine the instantaneous viscosity and surface tension. In chapter 6, we review the literature detailing key experimental attempts and mathematical advances in capturing the drop oscillation. We then discuss the effect of surfactants on the effective viscosity of the in-flight droplet.

Chapter 2

Mathematical framework of Drop-On-Demand problem

In this chapter, we present the governing equations and the numerical method used to solve the DOD problem. The finite element formulation is derived in detail both for the flow equation and the surface boundary condition. We present the discretised linearised system which our code is based on. Finally, a DOD simulation with the initial condition is shown and explained at each stage.

2.1 Mathematical Formulation

Equations of motion describing the physics governing fluid motion can be derived by analysing the fluid at either the molecular or the continuum level. The molecular description is appropriate when the dimensions of a system are comparable to or smaller than the mean free path of the fluid molecules. In liquids, this length scale is a few nanometres. In most conventional fluidic applications, such as inkjet printing, the relevant length scales are several orders of magnitude greater than this - typical nozzle diameters are $30\,\mu m$. For such applications, the discrete molecular nature of a liquid is ignored and instead a continuum approximation is adopted, wherein properties such as density, pressure and velocity are well-defined within infinitesimally small volumes and vary continuously from point to point.

The continuum equations governing the fluid flow can be derived from the fundamental conservation laws for mass, linear momentum and energy combined with constitutive relations between stress and strain within the fluid (Batchelor, 2000; Leal, 1992). While the conservation laws apply broadly to all fluids, the

constitutive relations are fluid-dependent.

For incompressible Newtonian flows the momentum conservation is given by the Navier-Stokes equation,

$$\rho \left(\frac{\partial \mathbf{u}}{\partial t} + (\mathbf{u} \cdot \nabla)\mathbf{u} \right) = -\nabla p + \mu \nabla \cdot \left(\nabla \mathbf{u} + (\nabla \mathbf{u})^T \right) + \rho g \mathbf{f} \,,$$

where $\mathbf{u}$ is the fluid velocity, p is the pressure in the fluid, μ is the dynamic viscosity of the fluid, g is the gravitational force and $\mathbf{f}$ is the unit vector where gravity is acting on its direction.

As the temperature of the fluid in the print-head is maintained at a constant value, there are no significant temperature variations during the jetting process and hence the viscosity and surface tension can be assumed to be constant. We can also neglect the effects of gravity due to the small scales involved (Morrison and Harlen, 2010), as the Stokes number given by

$$\mathrm{St} = \frac{\rho g R^2}{\mu U} \,,$$

is of order of $\mathcal{O}(10^{-5})$ in our case. Hence for a Newtonian fluid the dynamics are described by the following equations,

$$\rho \frac{\mathrm{D}\mathbf{u}}{\mathrm{D}t} = -\nabla p + \mu \nabla \cdot \left(\nabla \mathbf{u} + (\nabla \mathbf{u})^T \right) \,, \tag{2.1}$$

where the convective derivative is given by

$$\frac{\mathrm{D}}{\mathrm{D}t} = \frac{\partial}{\partial t} + (\mathbf{u} \cdot \nabla) \,,$$

together with the condition of incompressibility,

$$\nabla \cdot \mathbf{u} = 0 \,. \tag{2.2}$$

We assume that the contact line is pinned at the nozzle outlet and that no-slip occurs at the nozzle walls, where conditions of zero velocity are imposed ($\mathbf{u} = 0$). At the free surface, we assume that the drag on a droplet due to air resistance is negligible (Li et al., 2008) and impose a boundary condition on the stress,

$$\boldsymbol{\sigma} = -p\mathbf{I} + \mu \left[\nabla \mathbf{u} + (\nabla \mathbf{u})^T \right] \,, \tag{2.3}$$

due to surface curvature,

$$[\boldsymbol{\sigma} \cdot \mathbf{n}]_{\text{air}}^{\text{jet}} = -\gamma \left(\nabla_s \cdot \mathbf{n}\right) \mathbf{n}\,. \tag{2.4}$$

Here γ is the coefficient of surface tension, $\mathbf{n}$ is the unit vector normal to the free surface (directed outward from the jet), and the surface divergence operator is given by $\nabla_s \cdot := \nabla \cdot (\mathbf{I} - \mathbf{nn})$. $\nabla_s \cdot \mathbf{n}$ is the local curvature of the surface and can be written as

$$\nabla_s \cdot \mathbf{n} = \left(\frac{1}{R_1} + \frac{1}{R_2}\right)\,, \tag{2.5}$$

where R_1, R_2 are the principle radii of curvature (Leal, 1992).

The equations can be put into dimensionless form by scaling lengths with the nozzle outlet radius R_N, velocities by the drop speed U and pressure and stress by ρU^2. These scalings yield the dimensionless governing equations for the fluid domain Ω

$$\frac{\text{D}\mathbf{u}}{\text{D}t} - \nabla \cdot \boldsymbol{\sigma} = 0\,, \tag{2.6}$$

$$\nabla \cdot \mathbf{u} = 0\,. \tag{2.7}$$

We note that we use non-dimensional quantities from now on without changing the notation therefore t, $\mathbf{u}$, p and $\boldsymbol{\sigma}$ are now the dimensionless time, velocity, pressure and stress, respectively, with the stress tensor now given by

$$\boldsymbol{\sigma} = -p\mathbf{I} + \frac{1}{\text{Re}}\left[\nabla \mathbf{u} + (\nabla \mathbf{u})^T\right]\,. \tag{2.8}$$

The dimensionless interface boundary condition on the free surface S is given by

$$[\boldsymbol{\sigma} \cdot \mathbf{n}]_{\text{air}}^{\text{jet}} = -\frac{1}{\text{We}}\left(\nabla_s \cdot \mathbf{n}\right) \mathbf{n}\,. \tag{2.9}$$

Again, the dimensionless numbers Re and We are of the form

$$\text{Re} = \frac{\rho U R_N}{\mu}\,,$$

$$\text{We} = \frac{\rho U^2 R_N}{\gamma}\,.$$

2.2 Finite Element Formulation for Surface Tension Driven Flows

The equations (2.6) and (2.7) are solved using an Eulerian-Langrangian moving grid finite-element method, which was first developed for the study of creeping flow of dilute polymer solutions (Harlen et al., 1995) and extended to model DOD printing of both Newtonian (Castrejón-Pita et al., 2011) and viscoelastic inks (Morrison and Harlen, 2010).

2.2.1 Mesh generation

In this method, the finite-element mesh is Lagrangian, which means that the nodes advect with the fluid flow, so the mesh naturally follows the evolution of the free-surface. By allowing the finite elements to deform with the fluid velocity, the constitutive equation can be solved in the co-deforming frame. This method can naturally capture the free-surface shape in free-surface problems such as inkjet printing. Further details of the numerical scheme can be found in Morrison and Harlen (2010); Harlen et al. (1995); Westborg and Hassager (1989).

A drawback of the purely Lagrangian approach is that the mesh deforms with the fluid causing velocity gradients which distort the mesh reducing the accuracy of the finite-element solution. To prevent this, it is necessary to limit the mesh distortion by introducing a re-meshing algorithm to maintain element-shape quality. In order to do that, the nodes are retained as material points and reconnected in order to produce the best triangulation via the process of Delaunay triangulation. A simple algorithm for reconnecting an existing mesh to obtain a Delaunay triangulation is presented in Harlen et al. (1995).

In addition to reconnecting existing points, an adaptive mesh resolution algorithm is also employed to provide higher resolution in the thin neck regions in the ligament behind the main drop. Points are added or removed based on the length of mesh edges where the maximum and minimum edge lengths are set by the jet radius at that point. We compute the length for each edge and compare check whether or not is it greater than the maximum mesh length (L_M) or less than the minimum mesh length (L_m). So

$$(r_1 - r_2)^2 + (z_1 - z_2)^2 \begin{cases} < L_m^2, \\ > L_M^2. \end{cases}$$

The minimum and maximum length are determined at the beginning of each simulation by

$$
\begin{aligned}
L_m &= 0.008\alpha \,, \\
L_M &= 0.04\alpha \,,
\end{aligned}
$$

where $\alpha = \ell\mathcal{H}$, where

$$
\mathcal{H} = R_N \sqrt{\frac{\bar{r}}{R_N}} \,,
$$

where $\bar{r}$ is the average thickness of the jet in the vicinity of the point and R_N is the nozzle radius, with ℓ the mesh grade parameter chosen at the beginning of each simulation. This provides a local refinement of the mesh in regions where near the thinning neck. A smaller ℓ (e.g. 0.5) leads a finer mesh while a larger ℓ (e.g. 1.5) will result to a coarser mesh. We follow this process at each time step after computing the new velocity and make sure that the new mesh is used for the next time step.

The break-off of the jet occurs when the neck radius, i.e. the height of the jet neck, is less than a percentage of the nozzle radius. In this work, 1% of the nozzle radius is considered for the break-off. This value was chosen to match better with the experimental results (presented in §3.3) for the first (main) break-off of the head droplet from the ligament.

2.2.2 Weak formulation

We discretise equations (2.6) and (2.7) in space using the finite element method (Gresho and Sani, 1998). We define ϕ_i and ψ_j as the linear basis functions for the velocity and pressure finite element spaces respectively. To develop the finite element approximation, we obtain the weak formulation of the equations by multiplying each of the components of the momentum equation (2.6) with ϕ_i and equation (2.7) with ψ_j and integrating over the spatial domain Ω.

The surface divergence theorem (Deen, 1998), implies

$$
\int_\Omega \phi \nabla \cdot \boldsymbol{\sigma} \, \mathrm{d}\Omega = \int_S \phi \boldsymbol{\sigma} \cdot \mathbf{n} \, \mathrm{d}S - \int_\Omega \nabla\phi \cdot \boldsymbol{\sigma} \, \mathrm{d}\Omega \,. \tag{2.10}
$$

Therefore, we have

$$
\int_\Omega \phi_i \frac{\mathrm{D}\mathbf{u}}{\mathrm{D}t} \, \mathrm{d}\Omega + \int_\Omega \nabla\phi_i \cdot \boldsymbol{\sigma} \, \mathrm{d}\Omega = \int_S \phi_i \boldsymbol{\sigma} \cdot \mathbf{n} \, \mathrm{d}S \,, \ i = 1, \ldots, N_u \,, \tag{2.11}
$$

$$\int_{\Omega} \psi_j \left(\nabla \cdot \mathbf{u} \right) d\Omega = 0 \,, \ j = 1, \ldots, N_p \,, \tag{2.12}$$

where S is the boundary of the domain Ω and N_u and N_p are the number of non-Dirichlet velocity and pressure nodes respectively. Applying the free-surface boundary condition equation (2.9) to the surface integral in equation (2.11), gives

$$\int_{S} \left(\phi_i \boldsymbol{\sigma} \cdot \mathbf{n} \right) dS = - \int_{S_f} \phi_i \frac{1}{We} \left(\nabla_s \cdot \mathbf{n} \right) \mathbf{n} \, dS \,, \tag{2.13}$$

as the velocity satisfies a Dirichlet condition on the remaining portion of the boundary. Hence using equation (2.9) the weak form of the momentum equation is given by

$$\int_{\Omega} \rho \frac{D\mathbf{u}}{Dt} \phi_i \, d\Omega + \int_{\Omega} \nabla \phi_i \cdot \boldsymbol{\sigma} \, d\Omega = - \int_{S_f} \frac{1}{We} \left(\nabla_s \cdot \mathbf{n} \right) \mathbf{n} \, dS \,, \tag{2.14}$$

where S_f is the portion of the boundary composed on the fluid interface, i.e. the fluid free surface.

2.2.3   Surface tension and interfacial boundary condition

The discrete interfacial boundary condition is treated using the method presented by Westborg and Hassager (1989). From equation (2.4) the surface force density on the free surface is given by $\boldsymbol{\sigma} \cdot \mathbf{n} = -\gamma \kappa \mathbf{n}$, where κ is the mean curvature given by,

$$\kappa = \frac{1}{R_1} + \frac{1}{R_2} \,,$$

and R_1 and R_2 are the principle radii of curvature as in equation (2.5). For an axisymmetric jet where R_1 is the radius of curvature along the interface, we can obtain R_1 by using the Serret-Frenet formula

$$\frac{d\mathbf{t}}{ds} = -\frac{1}{R_1} \mathbf{n} \,,$$

where s denotes the arc length along the curve, $\mathbf{t}$ the unit tangent vector in the direction of s and $\mathbf{n} = (n_z, n_r)$.

Hence performing the azimuthal integral along a section of the free surface in equation (2.13), we obtain

$$- \int_{S_{AB}} \phi_i \frac{1}{We} \left(\nabla_s \cdot \mathbf{n} \right) \mathbf{n} \, dS = \frac{2\pi}{We} \int_{s_B}^{s_A} \left(\frac{d\mathbf{t}}{ds} - \kappa_\theta \mathbf{n} \right) \phi_i r \, ds \,, \tag{2.15}$$

where s_A, s_B are the values of s at the endpoint of the interface boundary and κ_θ

is the curvature on the θ-direction,

$$\kappa_\theta = \frac{\mathrm{d}z}{\mathrm{d}s}\frac{1}{r}\,.$$

Integrating by parts we get,

$$-\int_{S_{AB}} \phi_i \frac{1}{We}\left(\nabla_s \cdot \mathbf{n}\right)\mathbf{n}\,\mathrm{d}S = \frac{2\pi}{We}\left[\mathbf{t}\phi_i r\right]\bigg|_{s_B}^{s_A} - \frac{2\pi}{We}\int_{s_B}^{s_A}\left(\mathbf{t}\frac{\mathrm{d}}{\mathrm{d}s}(r\phi_i) + \mathbf{n}\phi_i r\kappa_\theta\right)\mathrm{d}s\,.$$

(2.16)

With this formulation, we can represent the interface with standard finite element functions requiring only C^0-continuity. The contribution from the ends vanishes if the surface is pinned since the contact line is a Dirichlet boundary. However, this integral must be included when considering a dynamic contact line.

2.3   Finite Element Discretisation

2.3.1   Axisymmetric elements

The weak formulation is based on the axisymmetric assumption where we have assumed a symmetry about the horizontal axis. A cylindrical system of coordinates is used (r, θ, z) and since we have a rotational geometry, there is no θ-dependence. Here, the velocity components are written as $\mathbf{u} = (u, 0, w)$, since we are assuming no swirl.

The stress tensor components are

$$\sigma_{rr} = -p + 2\mu\frac{\partial u}{\partial r}\,,$$
$$\sigma_{\theta\theta} = -p + 2\mu\frac{u}{r}\,,$$
$$\sigma_{zz} = -p + 2\mu\frac{\partial w}{\partial z}\,,$$
$$\sigma_{r\theta} = \sigma_{\theta r} = 0\,,$$
$$\sigma_{\theta z} = \sigma_{z\theta} = 0\,,$$
$$\sigma_{rz} = \sigma_{zr} = \mu\left(\frac{\partial u}{\partial z} + \frac{\partial w}{\partial r}\right)\,.$$

We now construct the discretised system for governing equations using the weak formulation given in equation (2.14). In cylindrical coordinates, the divergence

of the stress is given by

$$\nabla \cdot \boldsymbol{\sigma} = \begin{pmatrix} \frac{1}{r}\frac{\partial}{\partial r}(r\sigma_{rr}) + \frac{\partial \sigma_{rz}}{\partial z} - \frac{\sigma_{\theta\theta}}{r} \\ \frac{1}{r}\frac{\partial}{\partial r}(r\sigma_{rz}) + \frac{\partial \sigma_{zz}}{\partial z} \end{pmatrix}. \tag{2.17}$$

Multiply with ϕ_j and integrating over Ω

$$\int_{\Omega} (\nabla \cdot \boldsymbol{\sigma})\, \phi_j \, \mathrm{d}\Omega = 2\pi \int_{V} (\nabla \cdot \boldsymbol{\sigma})\, \phi_j r \, \mathrm{d}r \, \mathrm{d}z\,, \tag{2.18}$$

where $V(r, z)$ is the region of (r, z) space corresponding to Ω. Thus the z-component of this integral is

$$I_z = \int_{V} \left(\frac{1}{r}\frac{\partial}{\partial r}(r\sigma_{rz}) + \frac{\partial \sigma_{zz}}{\partial z} \right) \phi_j r \, \mathrm{d}r \, \mathrm{d}z = $$
$$\int_{V} \phi_j \frac{\partial}{\partial r}(r\sigma_{rz}) \, \mathrm{d}r \, \mathrm{d}z + \int_{V} \phi_j r \frac{\partial \sigma_{zz}}{\partial z} \, \mathrm{d}r \, \mathrm{d}z\,. \tag{2.19}$$

Integrating by parts

$$I_z = -\int_{V} r\sigma_{rz}\frac{\partial \phi_j}{\partial r} \, \mathrm{d}r \, \mathrm{d}z - \int_{V} r\sigma_{zz}\frac{\partial \phi_j}{\partial z} \, \mathrm{d}r \, \mathrm{d}z+$$
$$+ \int_{s_A}^{s_B} r\sigma_{rz}n_r \, \mathrm{d} + \int_{s_A}^{s_B} r\sigma_{zz}n_z \, \mathrm{d}s\,, \tag{2.20}$$

where s is the coordinate along the free surface.

Similarly for the equation in the r-direction

$$I_r = \int_{V} \left(\frac{1}{r}\frac{\partial}{\partial r}(r\sigma_{rr}) + \frac{\partial \sigma_{rz}}{\partial z} - \frac{\sigma_{\theta\theta}}{r} \right) \phi_j r \, \mathrm{d}r \, \mathrm{d}z =$$
$$-\int_{V} r\sigma_{rr}\frac{\partial \phi_j}{\partial r} \, \mathrm{d}r \, \mathrm{d}z - \int_{V} r\sigma_{rz}\frac{\partial \phi_j}{\partial z} \, \mathrm{d}r \, \mathrm{d}z - \int_{V} \sigma_{\theta\theta}\phi_j \, \mathrm{d}r \, \mathrm{d}z$$
$$+ \int_{s_A}^{s_B} r\sigma_{rr}n_r \, \mathrm{d}s + \int_{s_A}^{s_B} r\sigma_{rz}n_z \, \mathrm{d}s\,. \tag{2.21}$$

We now introduce a finite element approximation for the position and the velocity vectors as

$$z = \sum_{j=1}^{N_u} z_j\phi_j\,, \tag{2.22}$$

$$r = \sum_{j=1}^{N_u} r_j\phi_j\,, \tag{2.23}$$

where (r_j, z_j) are the nodal coordinates at time t, N_u is the number of nodes and ϕ_j are the basis functions. The corresponding velocities are defined by

$$w = \sum_{j=1}^{N_u} w_j \phi_j \,, \tag{2.24}$$

$$u = \sum_{j=1}^{N_u} u_j \phi_j \,, \tag{2.25}$$

where $w_j = \dfrac{\mathrm{D}z_j}{\mathrm{D}t}$ and $u_j = \dfrac{\mathrm{D}r_j}{\mathrm{D}t}$. The pressure field is approximated as

$$p = \sum_{k=1}^{N_p} p_k \psi_k \,, \tag{2.26}$$

where p_k are the nodal values, N_p is the number of pressure nodes and ψ_j are the basis functions.

Hence the stress tensor is now given by

$$\sigma_{rr} = \sum \left(-p_i \psi_i \right) + 2\mu \left(\sum \frac{\partial \phi_i}{\partial r} u_i \right) , \tag{2.27}$$

$$\sigma_{rz} = \mu \left(\sum \left[\frac{\partial \phi_i}{\partial z} u_i + \frac{\partial \phi_i}{\partial r} w_i \right] \right) , \tag{2.28}$$

$$\sigma_{zz} = \sum \left(-p_i \psi_i \right) + 2\mu \sum \left(\frac{\partial \phi_i}{\partial z} w_i \right) , \tag{2.29}$$

$$\sigma_{\theta\theta} = \sum -p_i \psi_i + 2\mu \sum \frac{\phi_i u_i}{r} \,. \tag{2.30}$$

Since the nodes of the finite elements are material points

$$\frac{\mathrm{D}\phi_i}{\mathrm{D}t} = \frac{\partial \phi_i}{\partial t} + \mathbf{u} \cdot \nabla \phi_i = 0 \,. \tag{2.31}$$

Therefore

$$\int_\Omega \phi_j \frac{\mathrm{D}\mathbf{u}}{\mathrm{D}t} \, \mathrm{d}\Omega = 2\pi \int_V \sum_i \phi_j \phi_i \frac{\mathrm{d}\mathbf{u}_i}{\mathrm{d}t} r \, \mathrm{d}r \, \mathrm{d}z \,. \tag{2.32}$$

Now

$$\sum_i \int_V r\phi_i \phi_j \frac{\mathrm{d}w_i}{\mathrm{d}t} \,\mathrm{d}r\,\mathrm{d}z - \sum_i \left[\int_V r\mu \left(\frac{\partial \phi_j}{\partial r} \frac{\partial \phi_i}{\partial z} \right) u_i \,\mathrm{d}r\,\mathrm{d}z \right]$$

$$- \sum_i \left[\int_V r\mu \left(\frac{\partial \phi_j}{\partial r} \frac{\partial \phi_i}{\partial r} \right) w_i \,\mathrm{d}r\,\mathrm{d}z \right] - \sum_i \left[\int_V r \left(2\mu \frac{\partial \phi_j}{\partial z} \frac{\partial \phi_i}{\partial z} \right) w_i \,\mathrm{d}r\,\mathrm{d}z \right]$$

$$+ \sum_i \left[r \left(\frac{\partial \phi_j}{\partial z} \psi_i \right) p_i \,\mathrm{d}r\,\mathrm{d}z \right] = \frac{1}{\mathrm{We}} \sum_i \left[\int_{s_B}^{s_A} \left(t_z \frac{\mathrm{d}}{\mathrm{d}s}(r\phi_i) + n_z \phi_i r \kappa_\theta \right) \mathrm{d}s \right]$$

$$= f. \tag{2.33}$$

We can form the mass matrix $M^{ij} = \int_V r\phi_i \phi_j \,\mathrm{d}r\,\mathrm{d}z$ and entries for the stiffness matrix are

$$K_{zz}^{ij} = - \int_V r \left(2\mu \frac{\partial \phi_i}{\partial z} \frac{\partial \phi_i}{\partial r} + \mu \frac{\partial \phi_i}{\partial r} \frac{\partial \phi_j}{\partial r} \right) \mathrm{d}r\,\mathrm{d}z, \tag{2.34}$$

$$K_{rz}^{ij} = - \int_V r\mu \left(\frac{\partial \phi_i}{\partial z} \frac{\partial \phi_j}{\partial r} \right) \mathrm{d}r\,\mathrm{d}z, \tag{2.35}$$

$$K_{pz}^{ij} = \int_V r \left(\psi_i \frac{\partial \phi_j}{\partial z} \right) \mathrm{d}r\,\mathrm{d}z. \tag{2.36}$$

For the equation in the r direction,

$$- \sum_i M^{ij} \frac{\mathrm{d}u_i}{\mathrm{d}t} - \sum_i \left[\int_V r \left(2\mu \frac{\partial \phi_j}{\partial r} \frac{\partial \phi_i}{\partial r} \right) u_i \,\mathrm{d}r\,\mathrm{d}z \right]$$

$$+ \sum_i \left[\int_V r \left(\frac{\partial \phi_j}{\partial r} \psi_i \right) p_i \,\mathrm{d}r\,\mathrm{d}z \right] - \sum_i \left[\int_V r \left(\mu \frac{\partial \phi_j}{\partial z} \frac{\partial \phi_i}{\partial z} \right) u_i \,\mathrm{d}r\,\mathrm{d}z \right]$$

$$- \sum_i \left[\int_V r \left(\mu \frac{\partial \phi_j}{\partial z} \frac{\partial \phi_i}{\partial r} \right) w_i \,\mathrm{d}r\,\mathrm{d}z \right] + \sum_i \left[\int_V (\phi_j \psi_i) \, p_i \,\mathrm{d}r\,\mathrm{d}z \right]$$

$$- \sum_i \left[\int_V \left(2\mu \frac{\phi_j \phi_i}{r} \right) u_i \,\mathrm{d}r\,\mathrm{d}z \right] = \frac{1}{\mathrm{We}} \sum_i \left[\int_{s_B}^{s_A} \left(t_r \frac{\mathrm{d}}{\mathrm{d}s}(r\phi_i) + n_r \phi_i r \kappa_\theta \right) \mathrm{d}s \right]$$

$$= g. \tag{2.37}$$

Again, the entries for the coefficient matrix are

$$K_{rr}^{ij} = - \int_V r \left(2\mu \frac{\partial \phi_i}{\partial r} \frac{\partial \phi_j}{\partial r} + \mu \frac{\partial \phi_i}{\partial z} \frac{\partial \phi_j}{\partial z} \right) \mathrm{d}r\,\mathrm{d}z - \int_V \left(2\mu \frac{\phi_i \phi_j}{r} \right) \mathrm{d}r\,\mathrm{d}z, \tag{2.38}$$

$$K_{pr}^{ij} = \int_V r \left(\frac{\partial \phi_j}{\partial r} \psi_i \right) \mathrm{d}r\,\mathrm{d}z + \int_V (\phi_j \psi_i) \, p_i \,\mathrm{d}r\,\mathrm{d}z, \tag{2.39}$$

$$K_{zr}^{ij} = - \int_V r \left(\mu \frac{\partial \phi_j}{\partial z} \frac{\partial \phi_i}{\partial r} \right) \mathrm{d}r\,\mathrm{d}z. \tag{2.40}$$

From the weak formulation of conservation of mass equation (2.12), in axisymmetric form, we have

$$\int_{\Omega} \psi_j \left(\frac{1}{r} \frac{\partial}{\partial r}(ru) + \frac{\partial w}{\partial z} \right) \mathrm{d}\Omega = 0 \,, \tag{2.41}$$

and by substituting the finite element approximation for u and w from equations (2.24) and (2.25)

$$\int_V \psi_j \left[\sum_i \left(\frac{\partial \phi_i}{\partial r} + \frac{\phi}{r} \right) u_i + \frac{\partial \phi}{\partial z} w_i \right] r \, \mathrm{d}r \, \mathrm{d}z = 0 \,. \tag{2.42}$$

These integrals can be solved analytically.

The entries for the coefficient matrix are

$$K_{rp}^{ij} = \int_V \left(\psi_j \frac{\partial \phi_i}{\partial r} + \psi_j \frac{\phi_i}{r} \right) r \, \mathrm{d}r \, \mathrm{d}z \,, \tag{2.43}$$

$$K_{zp}^{ij} = \int_V \psi_j \frac{\partial \phi_i}{\partial z} r \, \mathrm{d}r \, \mathrm{d}z \,. \tag{2.44}$$

Here, we note that $K_{rz}^{ij} = K_{zr}^{ji}$ and $K_{pz}^{ij} = K_{zp}^{ji}$. The entry K_{pp}^{ij} is the pressure stabiliser and is equal to zero.

With the formulation of equations (2.34) to (2.36), (2.38) to (2.40), (2.43) and (2.44) we have the following discretised system for the axisymmetric flow in cylindrical coordinates

$$\begin{pmatrix} \mathbf{M} & 0 & 0 \\ 0 & \mathbf{M} & 0 \\ 0 & 0 & 0 \end{pmatrix} \begin{pmatrix} \frac{\mathrm{d}w}{\mathrm{d}t} \\ \frac{\mathrm{d}u}{\mathrm{d}t} \\ 0 \end{pmatrix} + \begin{pmatrix} \mathbf{K}_{zz} & \mathbf{K}_{rz} & \mathbf{K}_{pz} \\ \mathbf{K}_{rz} & \mathbf{K}_{rr} & \mathbf{K}_{pr} \\ \mathbf{K}_{pz} & \mathbf{K}_{pr} & \mathbf{0} \end{pmatrix} \begin{pmatrix} w \\ u \\ p \end{pmatrix} = \begin{pmatrix} \mathbf{f} \\ \mathbf{g} \\ \mathbf{0} \end{pmatrix} \,. \tag{2.45}$$

2.3.2 Time discretisation

In the Lagrangian frame the Lagrangian material derivative $\mathrm{D}\mathbf{u}/\mathrm{D}t$ becomes the ordinary time derivative $\mathrm{d}\mathbf{u}/\mathrm{d}t$. Time derivatives are discretised using a θ scheme where the value of a variable ψ at the $(n+1)^{\mathrm{th}}$ time step is given by

$$\psi_{n+1} = \psi_n + \delta t \left[\theta \dot{\psi}_{n+1} + (1 - \theta) \dot{\psi}_n \right] \,, \tag{2.46}$$

where δt is the time step, $\theta \in [0, 1]$ is the weighting parameter of the scheme and $\dot{\psi} = \mathrm{d}\psi/\mathrm{d}t$. The size of the time-step δt is restricted by a CFL condition of the form $U\delta t < \delta x$, due to the moving mesh, where U is a typical flow velocity and δx

is a typical element size.

In addition to the time derivative in the momentum equation, the solution at the $(n+1)^{\text{th}}$ step depends upon the position of the nodes, which move with the fluid velocity. For each variable ψ, equation (2.46) results in a non-linear algebraic equation for ψ_{n+1} in terms of ψ_n. We linearise this equation via a Picard iteration scheme, since the node positions depend on the solution for the velocity.

The position $\mathbf{x}$ of any mesh node (except those on the nozzle inlet boundary) is updated after each time step as

$$\mathbf{x}_{n+1} = \mathbf{x}_n + \delta t \left[\theta \mathbf{u}_{n+1} + (1-\theta)\mathbf{u}_n \right] , \tag{2.47}$$

where θ is the same parameter as in equation (2.46). For the nodes on the nozzle inlet, special consideration is taken. Their positions are held constant to preserve the nozzle shape and the applicability of the driving boundary condition. This method is presented in Harlen et al. (1995) in more details.

So for each single time-step we have:

1. Solve the linearised system (minimum residual method) for $\mathbf{u}_{n+1}, p_{n+1}$ on the current geometry

2. Update the position of the nodes and the free surface as in equation (2.47)

3. Compare with older solution $\mathbf{u}_n$, $\mathbf{u}_n - \mathbf{u}_{n+1}$

4. If the difference is small enough, continue to next time-step. If not, repeat steps (1)-(3).

2.4   Summary

In this chapter, we presented the governing equations for the simple Newtonian fluid DOD simulation. The details of the derivation of the weak formulation of the system as well as the discretised linearised system is shown. We will show later in chapter 4 the amendments and additional equations required to model the surfactant transport and the effects of dynamic surface tension.

Chapter 3

Drop-On-Demand Jetting of Newtonian Fluids

In this chapter, the results of the mathematical model from chapter 2 are presented. We explore the parameter space in which the desired jetting behaviour for inkjet printing is found. In particular, we focus on the range of values for surface tension and viscosity required to produce drops at a desired drop speed from a given nozzle. Our simulations are compared with high-speed video observations of drop formation in an industrial inkjet print-head. We then examine the dependence of different jetting properties, such as ligament length and break-off time on fluid parameters and jetting speed. Finally, we present a phase diagram which predicts a region for good jetting behaviour parametrised by viscosity and surface tension.

3.1   Introduction

In the majority of industrial inkjet printers, drops are generated by a piezolectric ceramic element, which changes shape in response to an electric current, creating a pressure pulse within the print-head that leads to the ejection of a small volume of fluid (Hutchings et al., 2007; Martin et al., 2008). The shape that is commonly observed for the ejected fluid upon exiting the nozzle is an approximately spherical head with a trailing ligament (Martin et al., 2008). However the detailed shape, drop volume and velocity are all controlled by the magnitude and form of the pressure pulse.

Inks used in the inkjet printing industry are from a wide range of fluids depending on the application (Basaran et al., 2013; Derby, 2010). Complex dynam-

ics and different mechanisms are observed when complex fluids are used, even in standard inkjet print-heads. There have studies in inkjet printing with the addition of polymers, where viscoelastic effects rise (Morrison and Harlen, 2010; Hoath et al., 2012) and with the addition of small particles, where an asymmetry on the meniscus leads to the entrapment of air bubbles inside the nozzle (de Jong et al., 2006). However, there are many applications like water-based inks which have a simple Newtonian behaviour. In this chapter, we focus on fluids which are expected to follow a Newtonian behaviour and so we shall consider a constant viscosity and surface tension.

Detailed studies of the contraction of cylindrical fluid filaments (Schulkes, 1996; Notz and Basaran, 2004; Castrejon-Pita et al., 2012; Anthony et al., 2019) find that the Ohnesorge number indicates the critical aspect ratio that determines whether a filament contracts to a single drop or breaks up due to droplets breaking away from the end of the filament. For Ohnesorge numbers greater than around 0.3, a fluid filament of aspect ratio 25 contracts to a single drop, whereas for smaller Ohnesorge numbers the filament will break into multiple droplet (Notz and Basaran, 2004; Castrejon-Pita et al., 2012; Anthony et al., 2019).

There have been a number of experimental studies of DOD jetting (Dong et al., 2006; Martin et al., 2006; Hutchings et al., 2007; Li et al., 2008; Tjahjadi et al., 1992; Muzzio et al., 1991) in which the pressure and velocity response of the fluid, along with the meniscus position and minimum jet radius inside the print-head have been measured in response to the electrical driving pulse along with the meniscus position and minimum jet radius.

Castrejón-Pita et al. (2011) compare simulations with a large scale experimental model of a DOD printer and found excellent agreement in the detailed predictions of the evolution of the fluid domain during drop formation. In their experiments the nozzle diameter was 2 mm, however, the fluid properties at jetting speeds were chosen such that the Reynolds and Weber numbers were representative of industrial inkjet printing. Experimental images of droplet formation were compared with numerical simulations using the Lagrangian finite element code of Morrison and Harlen (2010) and showed excellent agreement between the simulations and experiments.

In this chapter, we extend this earlier study (Castrejón-Pita et al., 2011) in two ways. We explore in further detail the parameter space in which the desired jetting behaviour for inkjet printing is found. In particular, we focus on the range of values for surface tension and viscosity required to produce drops at a desired drop

speed from a given nozzle. This is a key difference to previous studies (McKinley and Renardy, 2011; Dong et al., 2006), where the study in the dimensionless group was based on changes on the drop speed. However, that results to unrealistic values that we do not find in inkjet printing, therefore a study on realistic parameters can provide more reasonable results. We also compare our simulations with high-speed video observations of drop formation in an industrial inkjet print-head rather than a large scale model to determine whether the different driving mechanics and more complex structure of a commercial print-head affects the comparison. We then examine the dependence of different jetting properties, such as ligament length and break-off time on fluid parameters and jetting speed. Finally, we present a phase diagram which predicts a region for good jetting behaviour parametrised by viscosity and surface tension.

3.2   A Drop-On-Demand Inkjet Simulation

The nozzle geometry used for the axisymmetric simulation of a DOD inkjet is shown in figure 3.1. The detailed flow within the entire print-head is not modelled, but instead only the flow in the region close to the nozzle. Since the nozzle is axisymmetric, this allows to make the assumption of axisymmetry where the axis of symmetry lies at the centre of the outlet nozzle, even though the print-head itself may be non-axisymmetric. The shape and dimensions of the nozzle are chosen to replicate the dimensions of the Ricoh GEN-5 print-head. The initial finite-element grid is shown in figure 3.1. The curved inlet (left side of figure 3.1) is an artificial inflow boundary across which there is a mass flow driven by the pressure variations within the print-head.

A time-dependent velocity boundary condition is imposed on this inlet boundary to provide a mass flow with a magnitude given by a driving signal. This is based on the qualitative behaviour of the print-head drive, which produces a "pull-push-pull" waveform. A graph of the typical time-dependence of signal used in the simulations and the corresponding position of the meniscus is shown in figure 3.2. In this case the drive is formed of three parabolic segments, each of 4 µs duration. In the initial phase (the first parabolic section) the meniscus is drawn back into the print-head. In the second phase the pressure drives liquid from the reservoir through the nozzle orifice. In the final stage liquid is again drawn back into the nozzle from the tail of the emergent jet.
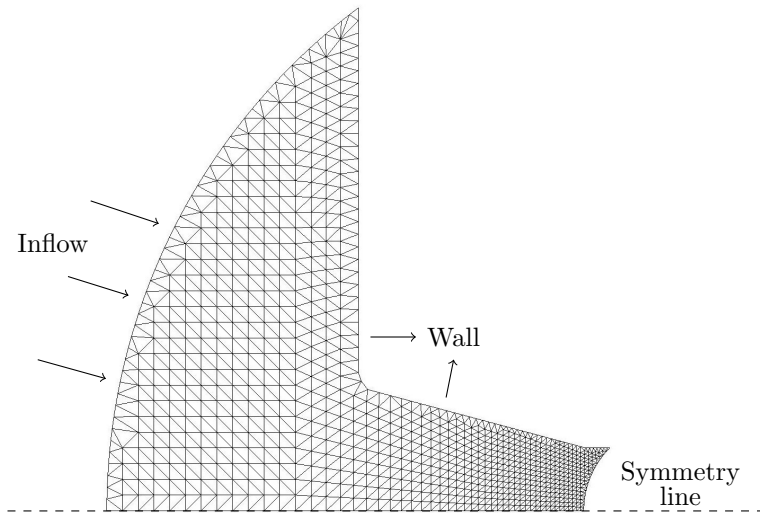
Figure 3.1: The nozzle shape and the initial mesh used in the simulations. The jet is assumed to be axisymmetric so for the production of subsequent images, the results are a mirrored around the axis of symmetry.
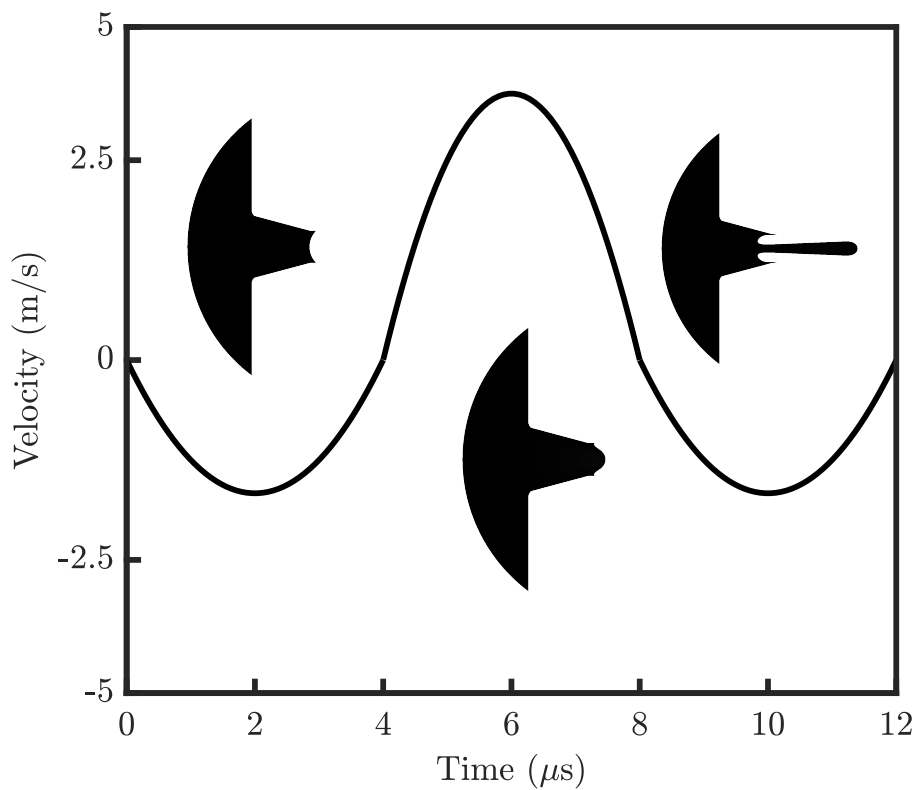
Figure 3.2: Plot of the driving signal as a function of time, which is imposed as a flux boundary condition over the nozzle inlet. Inside: Images showing the meniscus position at 0, 6 and 11 µs.

The initial 'pull' phase of the driving signal is shown in figure 3.3a. At the beginning of the final 'pull' stage of the simulated driving signal, the ligament length and the drop diameter are both equal to the nozzle diameter, as seen in figure 3.3b.

The ligament then pinches off from the nozzle at the end of this 'pull' phase shown in figure 3.3c. The final velocity is the speed at the front of the main drop, which is usually less than the velocity when the ligament is attached.

When the ligament has pinched off from the nozzle, it may merge with the main drop or break up into satellite drops due to the capillary instability. The generation of satellite drops due to ligament break-up is dependent on a number of factors, notably the Ohnesorge number. Here, no coalescence after the break-up is considered, whereas in reality drops may merge into another. The ligament is seen to break up into numerous satellite drops in figure 3.3e.

(a) $t = 4\,\mu s$ (b) $t = 8\,\mu s$ (c) $t = 37\,\mu s$ (d) $t = 74\,\mu s$ (e) $t = 91\,\mu s$
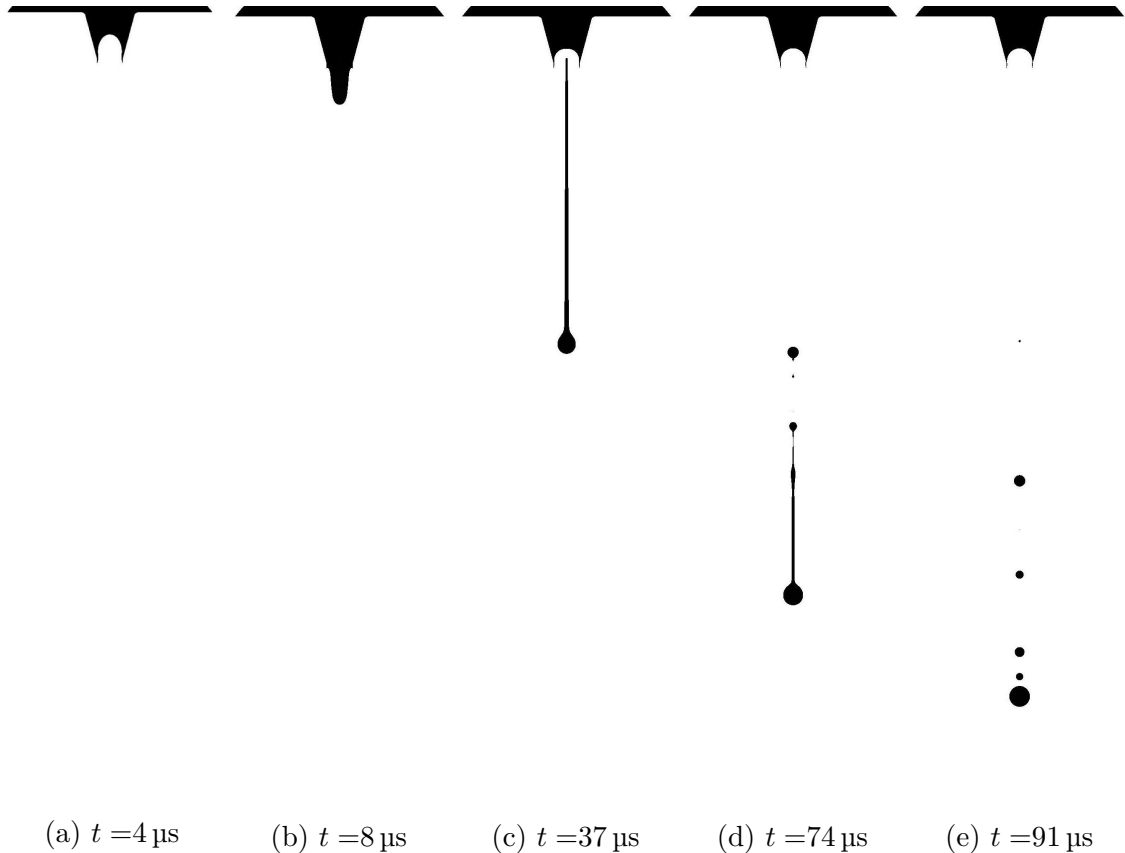
Figure 3.3: Simulation of the different phases of DOD jet process for a Newtonian fluid. (a) End of first 'pull' stage; (b) Start of final 'pull' stage; (c) Ligament pinches off the nozzle; (d) Final velocity reached; (e) Final break-up into satellite drops.

3.3 Experimental Methods

The experimental set-up is shown in figure 3.4. The experiments were performed using a Ricoh GEN-5 print-head which uses a piezoelectric drive to generate a pressure pulse in the ink chamber causing liquid to be ejected from the nozzle orifice. In this

work, the waveform of the voltage (and therefore pressure) signal was kept constant, with amplitude adjusted to control the speed of ejected fluid. Other studies have investigated the effect of the waveform optimisation in the droplet formation showing key characteristics of the timing and the amplitude in different jetting properties (Dong et al., 2006). The simulation code used in this work requires an equivalent velocity waveform. This was inferred from the flow rate at the nozzle orifice.
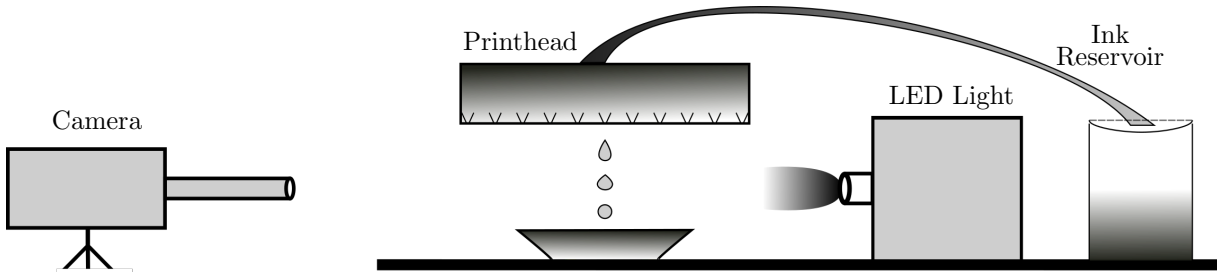
Figure 3.4: Schematic diagram of the experimental set-up.

High-speed videos were recorded using an ultra-high-speed Photron Fastcam SA-Z camera. The lens of the camera is Navitar 1-50486 (530980) (12×) and the fiber LED light source is a Keyman LA-HDF7010. This provided images at a resolution of 512×56 recorded at 480,000 frames per second. This allows the evolution of a single drop to be followed, enabling variations between different jetting events to be captured, such as the position of satellites drops, whilst producing of sufficient quality for the details of the ligament break-up to be observed.

Experiments were conducted using two different sets of fluids. A test fluid was provided by Ricoh with surface tension $0.03 \, \text{N m}^{-1}$, viscosity $0.012 \, \text{N s m}^{-2}$ and density $1021 \, \text{kg m}^{-3}$ and different PPH-TPM (Glycol Ether from DOW) mixtures of 20, 40, 50 and 60 %(w/v) with surface tension and viscosity presented in table 3.1. Viscosity was measured on the Malvern Kinexus rotational rheometer and surface tension on the Theta Attension pending drop meter. These fluids showed Newtonian behaviour at the shear rates encountered with this study. All the experiments were performed at 26 °C.

% PPH	Viscosity (N s m^{-2})	Surface tension (N m^{-1})
20	0.0074	0.035
40	0.0094	0.036
50	0.0116	0.037
60	0.0129	0.038
test fluid	0.012	0.030

Table 3.1: PPH-TPM mixtures properties

3.4 Comparison between Simulations and Experiments

We begin by comparing the images of drop formation taken from the simulations and experiments for droplets jetted at $7\,\mathrm{m\,s^{-1}}$. This jetting velocity is considered the optimal printing speed for this print-head by Ricoh. These are shown in figures 3.5 and 3.6 where snapshots at different times after the drop emerges from the nozzle are compared. Each image compares two different experimental droplets produced from the same nozzle under the same jetting conditions with the simulation where the ink properties at drop speed match those of the experiments presented in §3.3. The principal uncertainty in the comparison is the precise form of the driving waveform. The jetting velocity is defined to be the head drop speed after it has detached from the ligament. Although the drop speed will subsequently decrease due to aerodynamic drag, this effect is negligible within the observed length. In the experiments, the jetting velocity is measured using the proprietary drop measurement system provided by Ricoh, where an appropriate calibration is initially needed in order to provide the correct length scale. In the simulations, after a study on the amplitude for the waveform where we increase and decrease the amplitude in order to achieve a head drop speed with a 5% difference from the desired drop speed.

Nevertheless it can be seen that there is good agreement between the experiments and the simulations. In particular, the first snapshot taken shortly after the ligament detaches from the print-head, shows that this first break-off event is captured accurately by the simulations. Following break-off, the ligament shortens with a bulb forming at the end. In the final frame, we see the growth of variations in the filament thickness that lead to break-up of the filament into satellites. Comparing the final frames in figure 3.5 shows that the precise position of these bulges on the filament differs between the left and right-hand image, indicating that these arise from the growth of instabilities seeded by noise that varies between droplets. Similar variations in thickness are seen in the simulations, although we observe an earlier break-up of the tail of the filament in the simulations than is seen experimentally.

The 40% PPH solution, shown in figure 3.6, shows a qualitatively similar evolution. However, in the final frame it can be seen that the ligament is both shorter and that the instability has developed further to the point where the ligament of the left-hand image has broken into two satellite drops. This fluid has both a lower viscosity and a higher surface tension than the Ricoh test fluid and so has a lower Ohnesorge number. Again, the ligament in the simulation breaks up slightly earlier than in the experiments. This may be a consequence of the approximation

of the drive waveform. Nevertheless the overall level of agreement confirms that the numerical model can capture the dynamics of jet break-up in a commercial inkjet print-head.
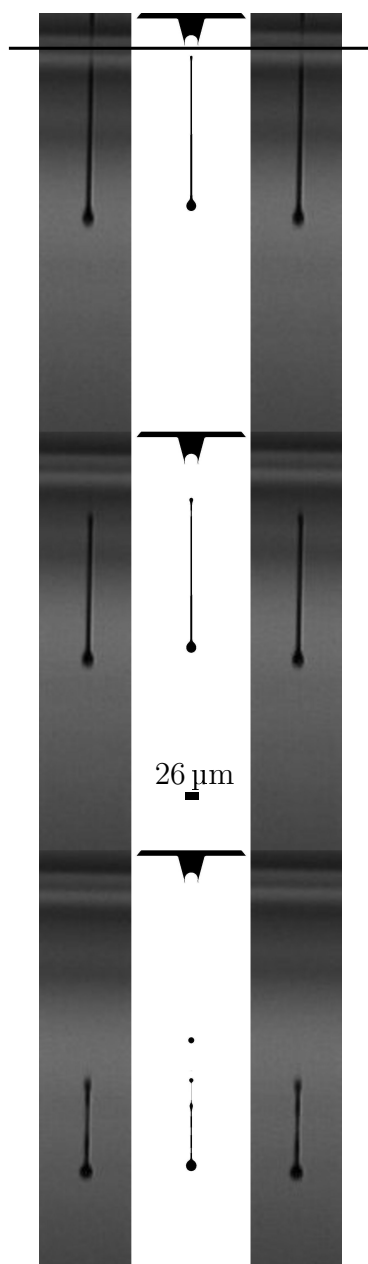
Figure 3.5: Comparison between simulations (white background) and experiments (grey background) with test fluid (Ricoh) at different times for a prescribed drop speed of $7\,\mathrm{m\,s^{-1}}$ at $41\,\mathrm{\mu s}$, $48\,\mathrm{\mu s}$ and $77\,\mathrm{\mu s}$, from top to bottom. The solid black line on the top indicates the exit of the nozzle.
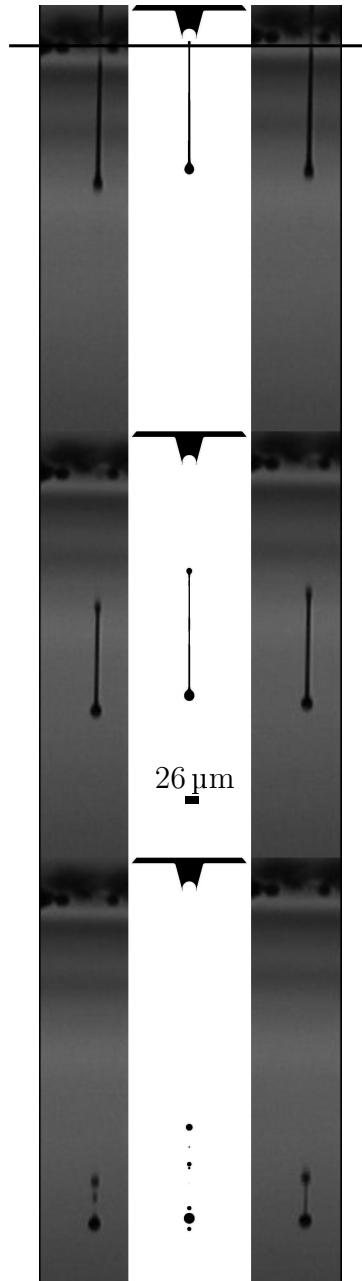
Figure 3.6: Comparison between simulations (white background) and experiments (grey background) with PPH 40% mixture at different times for a prescribed drop speed of $7\,\mathrm{m\,s^{-1}}$ at $33\,\mathrm{\mu s}$, $60\,\mathrm{\mu s}$ and $89\,\mathrm{\mu s}$, from top to bottom. The solid black line on the top indicates the exit of the nozzle. The spurious satellite in the computational results at the longest elapsed time is a result of the no implementation of coalescence in the code.

The experiments and the simulations are compared based on the drop speed, the ligament length and the drop radius. The length scale in the experiments was measured from the known drop speed and the time between frames. Small differences in the visible volume ejected are attributed to the difficulty on focusing with the current set-up. Further experiments with a different inkjet system at the University of Twente provided higher resolution images for a more detailed experimental comparison (see §5.2).

3.5   Effect of Jetting Speed

We next examine the effects of varying the jetting speed. This is achieved through varying the amplitude of the drive waveform within the model, or in the case of the experiments the voltage applied to the piezoelectric drive. The ink properties for the simulations were chosen to match the ones of the test fluid, described in §3.3. The velocity of the drop increases nearly linearly with the amplitude, in agreement with previous experimental studies (Hoath, 2016). In inkjet printing the desired range of the drop velocity is usually $5-10\,\mathrm{m\,s^{-1}}$, to prevent drops splashing on impact.
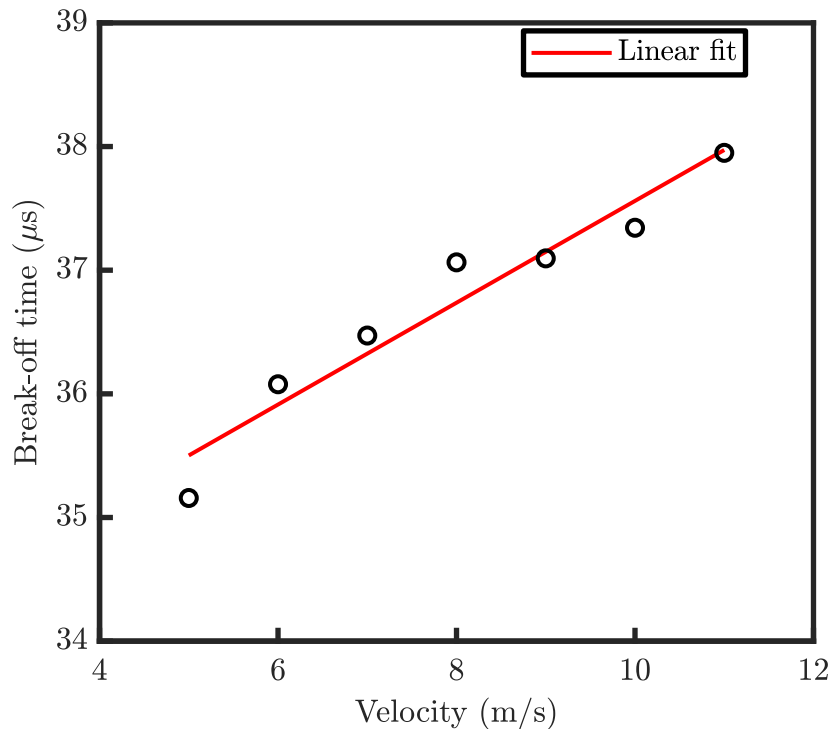
Figure 3.7: Graph showing the time of break-off of the droplet from the nozzle as a function of drop velocity from simulations. Time is measured from the start of the drive signal. The solid line shows a linear fit to the data and shows that the break-off time has a weak linear increase with the drop velocity.

We denote the break-off time as the time interval between the start of the drive waveform and the break-off of the droplet from the nozzle and present it as a function of drop velocity in the simulations. In figure 3.7 we see that this increases only slightly with increasing droplet speed (by a factor of 10% between 5 and 11 $\mathrm{m\,s^{-1}}$), suggesting that break-off is primarily determined by surface tension driven thinning rather than the pressure wave. It can also be observed that the time to break-off is comparable with the Rayleigh timescale (1.2) $t_R = \sqrt{\rho R^3/\gamma} = 8.2\,\mathrm{\mu s}$ for the growth rate of the capillary instability. However, the increasing drop speed does lead to a slight increase in break-off, which may be considered counter-intuitive, but arises from the stabilising effect of the extensional flow.
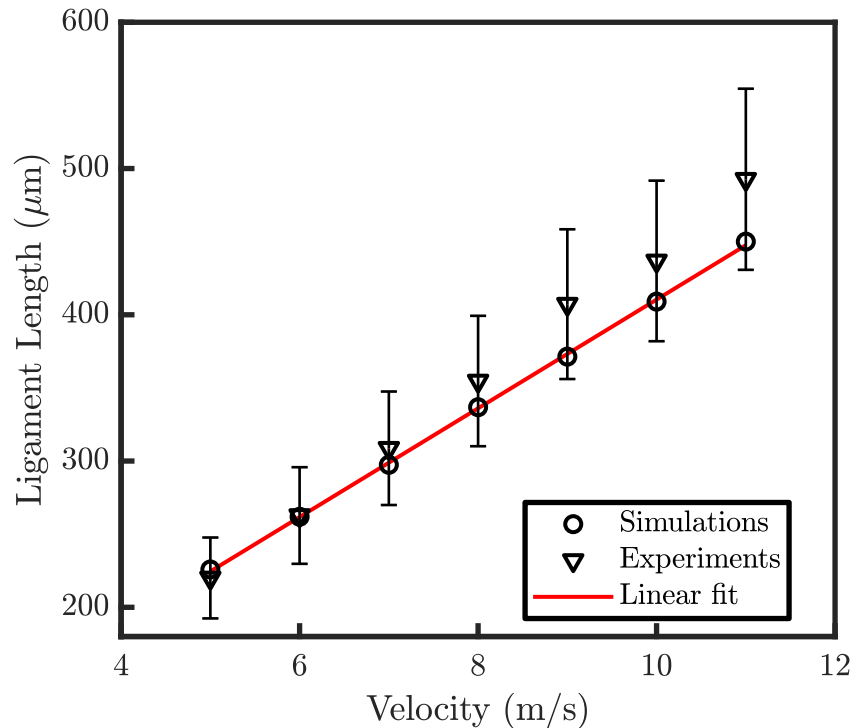
Figure 3.8: Comparison of the ligament length at the point of break-off as a function of drop velocity between simulations and experiments. The red solid line is the linear fit to the simulation data. The ligament length increases linearly with the drop velocity.

A consequence of the break-off time being only weakly dependent on the drop velocity is that the ligament length at break-off grows approximately linearly in proportion to the drop velocity and can be many jet diameters in length. This is shown in figure 3.8 where we compare the ligament lengths at different drop velocities between the simulations and experiments. Due to the resolution of video images there is an uncertainty in the ligament lengths measured from the experiments due to the size of the pixels. To establish a lengthscale, we count the number of pixels across the diameter of the droplet, which is known, and assume an error of plus and minus one pixel in this measurement. This provides a relative error for the ligament

length measurements. It can be seen that the simulations and experiments agree within this error range. These results also agree with the observations in previous experimental work of Dong et al. (2006).

The results in figures 3.7 and 3.8 indicate that the time of break-off is largely independent of drop velocity and that this time is comparable with the Rayleigh timescale. In contrast, the ligament length is directly proportional to droplet velocity over the typical operating range.

3.6   Different Fluid Properties

We now examine the effect of changing fluid properties when printing at a prescribed drop speed of $7\,\mathrm{m\,s^{-1}}$. In these simulations the surface tension and viscosity were varied in the range of 0.02-$0.09\mathrm{N\,m^{-1}}$ and 0.008-$0.012\mathrm{N\,s\,m^{-2}}$ respectively by varying the concentration of PPH and TPM (see in table 3.1). For each fluid the amplitude of the velocity waveform was adjusted until the desired drop velocity was achieved, however, the shape of the waveform was kept constant.
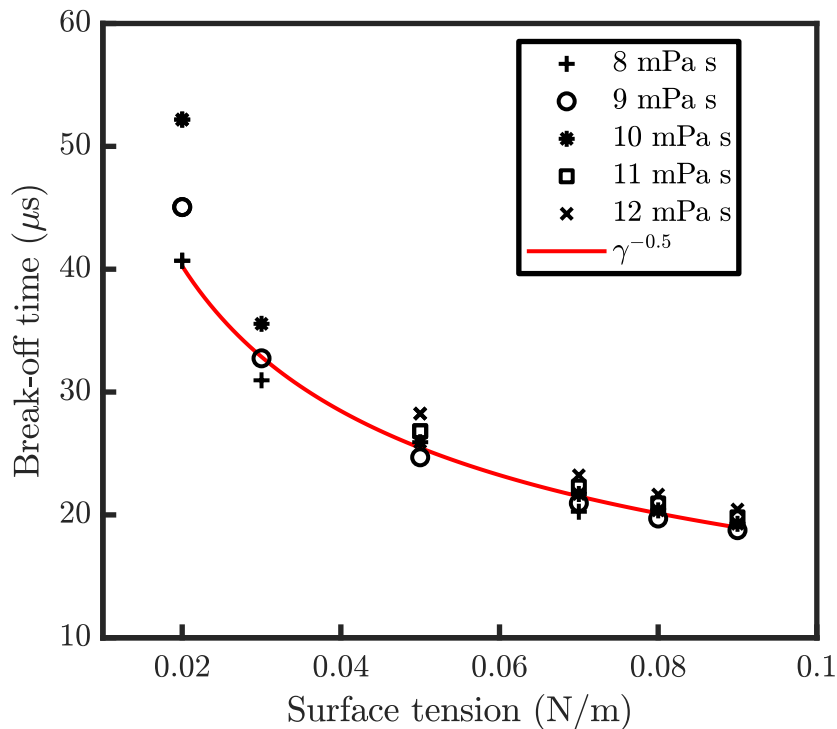
Figure 3.9: Break-off time for different fluids jetted at $7\,\mathrm{m\,s^{-1}}$. The red solid line shows that the break-off time follows a decay law inversely proportional to the square root of surface tension, as Rayleigh timescale (1.2).

The results from §3.5 suggest that while the drop speed is determined by

the driving waveform, the break-off is primarily driven by surface tension thinning. Figure 3.9 shows the first break-off time for different ink properties. It can be seen that the first break-off time is proportional to $\gamma^{-1/2}$, in agreement with the scaling suggested by the Rayleigh timescale (1.2). For this range of fluid viscosities there is also an increase in break-off time with viscosity, particularly for low values of surface tension, which correspond to the highest values of Ohnesorge number. However, at low Ohnesorge number, the fluid viscosity is of secondary importance. Figure 3.10 shows the variation in ligament length, which mirrors the variations in break-off time. Experimental measurements for the different PPH-TPM blends are also shown in figure 3.11, where there is a very good agreement with the results of the simulations.
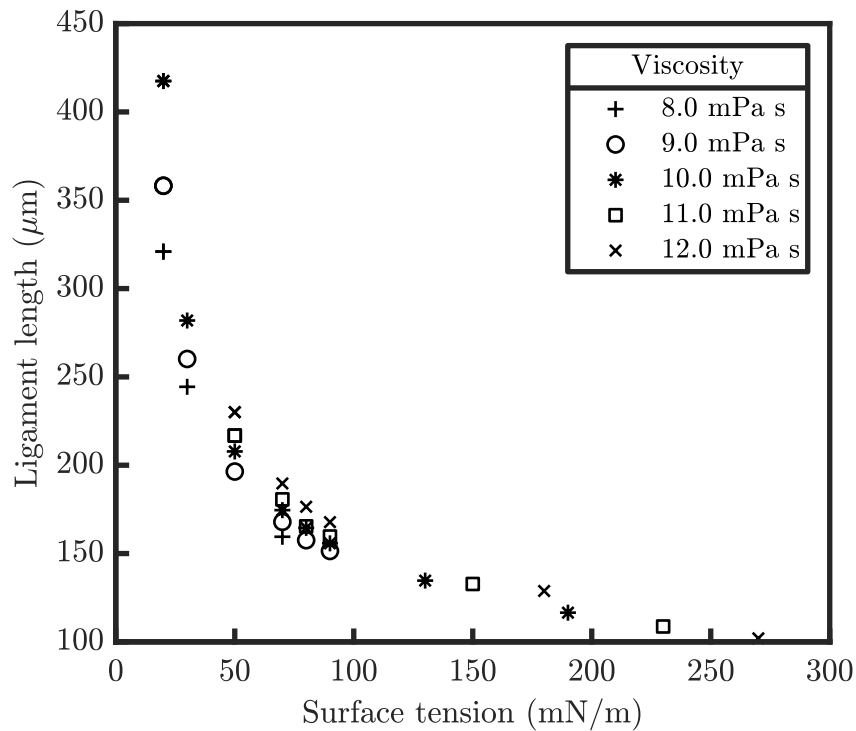
Figure 3.10: Ligament length at break-off time for different fluids jetted at $7\,\mathrm{m\,s^{-1}}$. The decay trend is the same as for the break-off time, shown in figure 3.9.
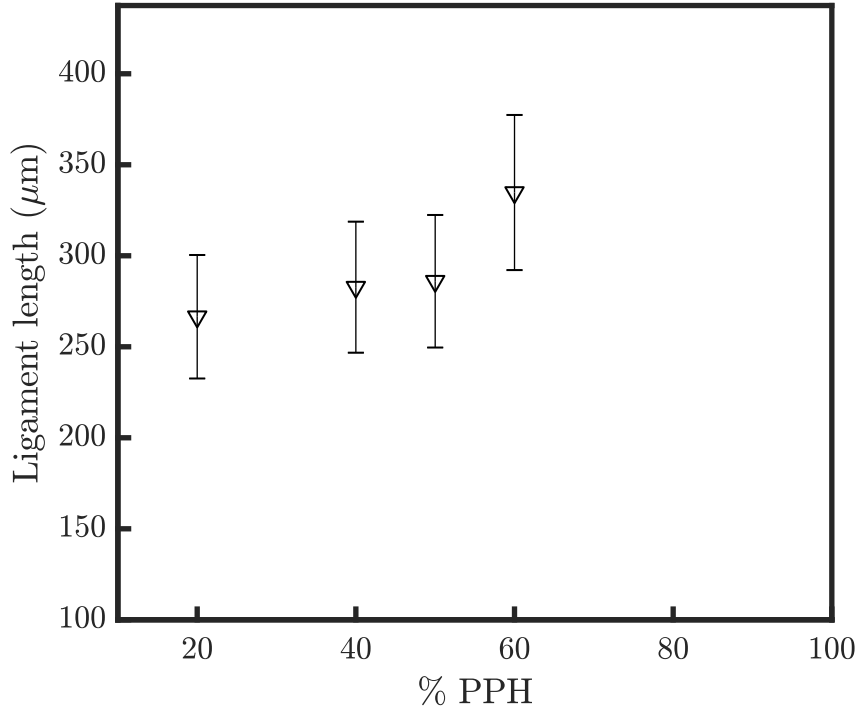
Figure 3.11: Measurements for the ligament length for different PPH-TPM blend are presented. The results agree well with the predicted simulations trend shown in figure 3.10.

Figures 3.12 and 3.13 compare the jetting behaviour between experiments and simulations for different solutions of PPH and TPM with properties presented in table 3.1 at constant drop speed $(7\,\mathrm{m\,s^{-1}})$, at the pinch-off from the nozzle and at a later time after the capillary break-off. The surface tensions of these mixtures are approximately the same $(0.036 \pm 0.02\mathrm{N\,m^{-1}})$ while the viscosity ranges from 0.0074 to $0.0129\,\mathrm{N\,s\,m^{-2}}$. The effect of this increase can be seen in the break-off time and the increase in the ligament length as shown in figure 3.12.
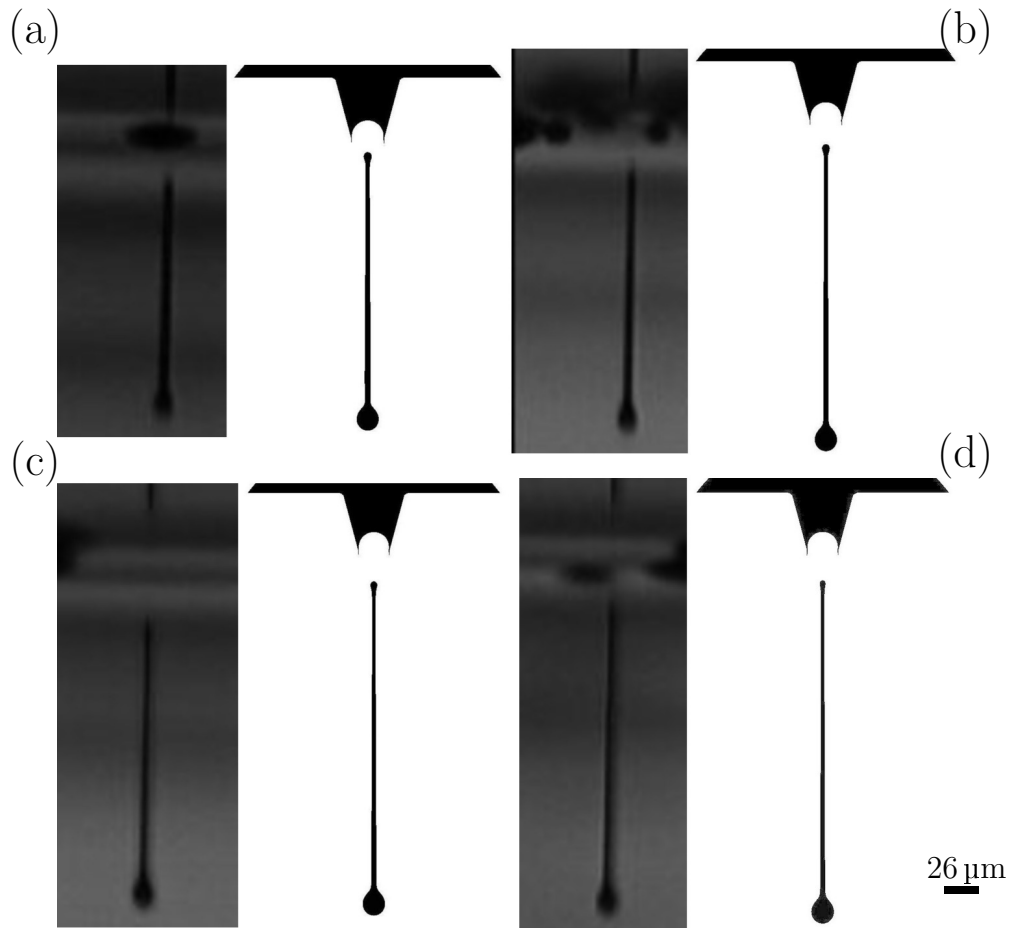
Figure 3.12: Comparison between different PPH-TPM blends at $7\,\mathrm{m\,s^{-1}}$. Left: experiments, right: simulations, (a) 20% at $31\,\mu s$, (b) 40% at $35\,\mu s$, (c) 50% at $39\,\mu s$ and (d) 60% at $41\,\mu s$ with ligament length of $22\,\mathrm{mm}$, $25\,\mathrm{mm}$, $30\,\mathrm{mm}$ and $28\,\mathrm{mm}$ respectively.
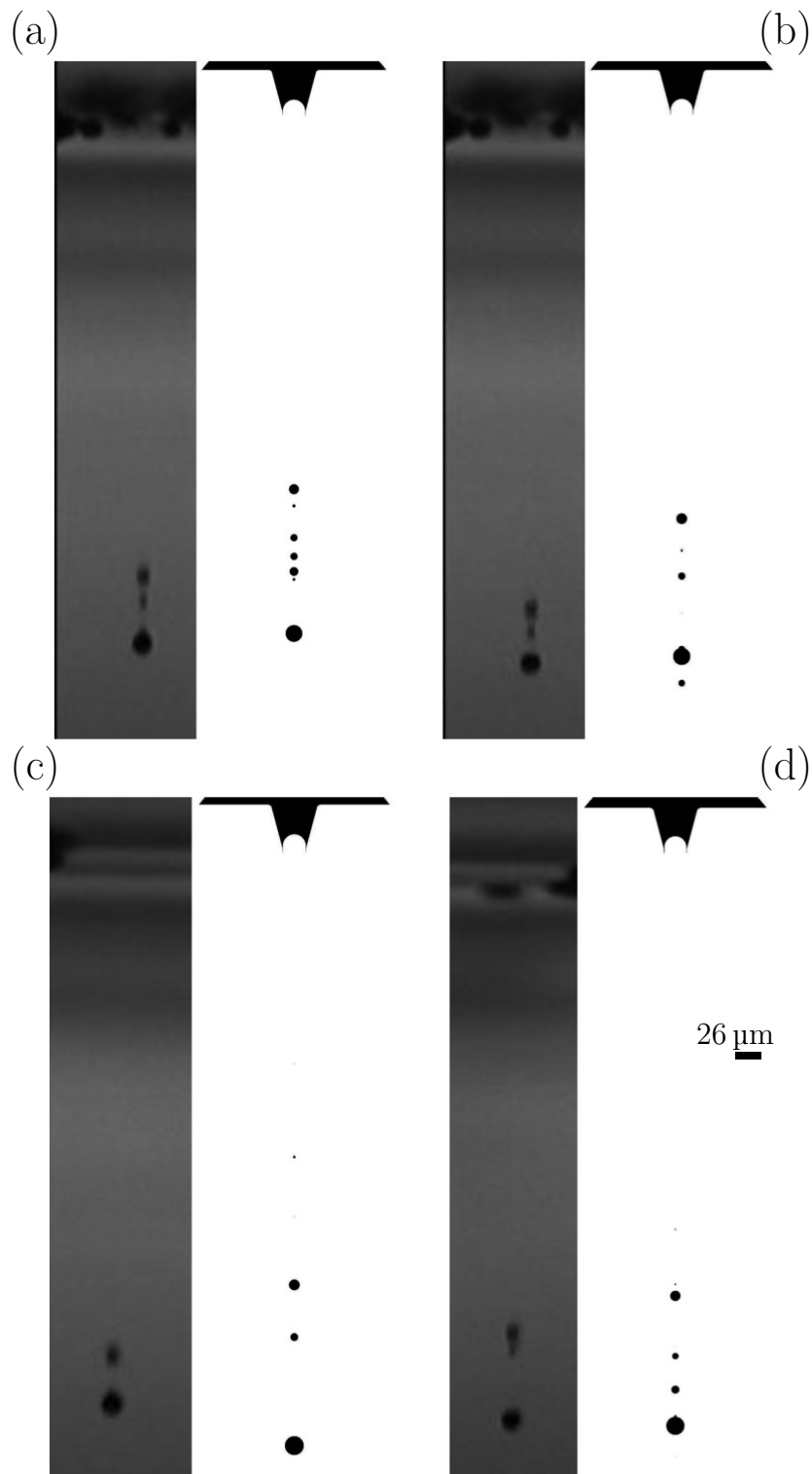
Figure 3.13: Comparison between different PPH-TPM blends at $7\,\mathrm{m\,s^{-1}}$. Top: experiments, bottom: simulations, from left to right: 20%, 40%, 50% and 60% at $89\,\mu\mathrm{s}$, $94\,\mu\mathrm{s}$, $96\,\mu\mathrm{s}$ and $100\,\mu\mathrm{s}$ respectively.

3.7 Jetting Behaviour

We now turn our attention to the subsequent drop formation after the drop and attached ligament have broken off from the nozzle in order to determine the range of fluid properties for which the jetted fluid forms into a single drop of the desired velocity before reaching the substrate. To do this, we ran a series of simulations with fluids of different viscosities and surface tensions through the same nozzle design at the same drop speed. For each of the simulations, the jetting behaviour is characterised as being one of three types:

- '*good*' if a single drop is formed or a small number of fast satellites are formed that will coalesce with the main drop,

- '*ligament*' where the ligament becomes very long, typical of more viscous fluids with low surface tension. Although these ligaments will eventually either retract into a single drop or break-up into satellite drops, this can take longer than the time of flight of the drop before striking the substrate.

- '*satellites*' where the ligament breaks up into multiple smaller drops that do not coalesce with the main drop, typical of less viscous fluids.

(a) Good jetting behaviour

(b) Ligament jetting behaviour

(c) Satellites jetting behaviour
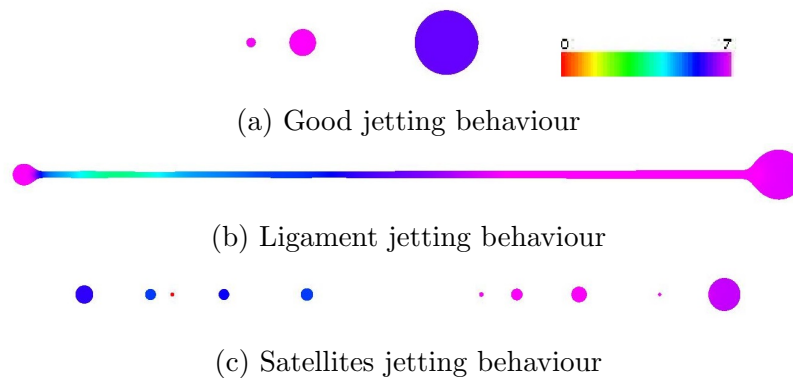
Figure 3.14: Jetting behaviour classification. (a) An example of good jetting behaviour. The two satellite droplets are moving faster than the main drop and so will merge with it. (b) An example of jet formation with a long stable ligament. (c) An example of drop formation where multiple satellite drops are formed that will not merge with the main drop. The colour bar shows the velocity value for the jet points.

In some cases it can be difficult to distinguish between the latter two as long ligaments will eventually break into satellites, so that some cases are classed as '*ligament/satellite*' to indicate that a long ligament is formed which then breaks into satellites.

In figure 3.15 we show the range of fluid properties where these different behaviours are found in the form of a phase diagram in Ohnesorge-Reynolds number space. Since the Reynolds number is independent of the surface tension, changes in surface tension correspond to movements parallel to the vertical axis, whereas decreasing viscosity both reduces the Ohnesorge number and increases the Reynolds number. The region of good behaviour, sketched in the green cross region is found
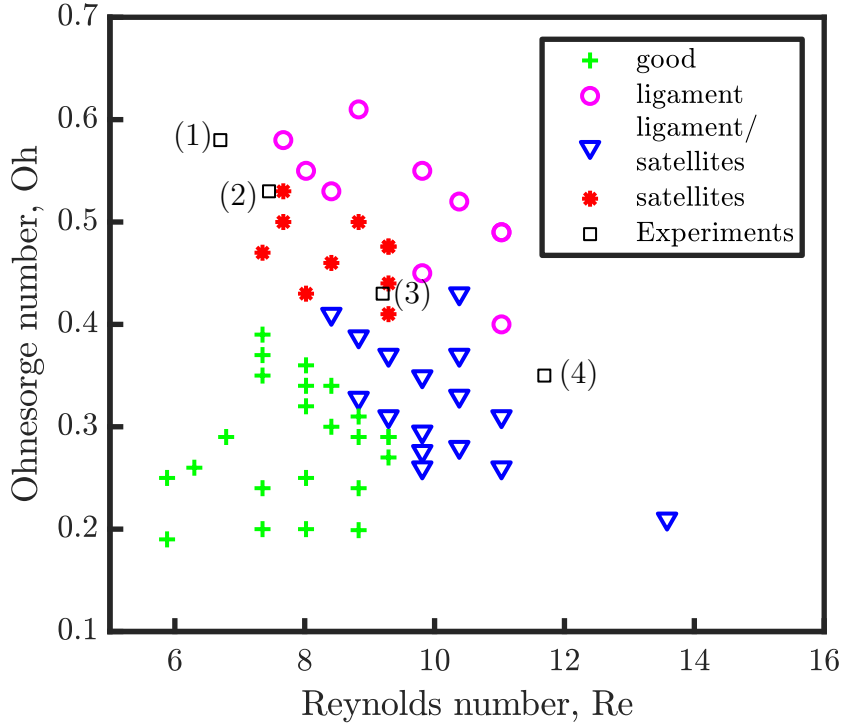
Figure 3.15: Jetting behaviour diagram showing the location of different classes of drop formation in terms of Oh and Re. The fluid properties for the experiment shown in here are presented in table 3.1 so (1): viscosity $0.013\,\mathrm{N\,s\,m^{-2}}$ and surface tension $0.038\,\mathrm{N\,m^{-1}}$, (2): viscosity $0.012\,\mathrm{N\,s\,m^{-2}}$ and surface tension $0.037\,\mathrm{N\,m^{-1}}$, (3): viscosity $0.009\,\mathrm{N\,s\,m^{-2}}$ and surface tension $0.036\,\mathrm{N\,m^{-1}}$, and (4): viscosity $0.007\,\mathrm{N\,s\,m^{-2}}$ and surface tension $0.035\,\mathrm{N\,m^{-1}}$.

to occur for Ohnesorge numbers in the range $0.2 < \mathrm{Oh} < 0.4$. We did not explore Ohnesorge numbers less than 0.2 as this was outside the range of realistic values of surface tension and viscosity for our chosen nozzle radius. This is consistent with the suggested jettability range of $0.1 < \mathrm{Oh} < 1$ (Hutchings and Martin, 2012; McKinley and Renardy, 2011). However, we find an additional restriction of $\mathrm{Re} < 10$ for satellite-free droplet formation. At higher Reynolds numbers, satellite formation is always observed, even at $\mathrm{Oh} = 0.3$. This restriction is distinct from the Reynolds number limit discussed in the literature (McKinley and Renardy, 2011; Hoath, 2016), which arises from splashing on impact with the substrate. In this case the restriction arises from the length (and hence aspect ratio) of the ligament formed behind the drop. At a fixed value of Ohnesorge number, an increase in Reynolds

number corresponds to an increase in drop velocity and hence ligament length, as shown in figure 3.8. Even at moderate values of Ohnesorge number, ligaments of very high aspect ratio will break up to form satellite drops (Hoath et al., 2013; Castrejon-Pita et al., 2012). At values of Oh > 0.4, fluid viscosity significantly retards the break-off of the drop from the nozzle as seen in figure 3.9 for low surface tension and high viscosity resulting in the formation of a long ligament.

3.8 Conclusions

Within this chapter, results from numerical simulations and experiments of droplet formation in an industrial DOD print-head have been presented. We find good agreement in the evolution of droplet shapes between the experiments and simulations, despite the uncertainty in determining the precise shape of the drive waveform.

This level of agreement gives confidence in using the simulations to analyse the mechanisms underlying the driving droplet formation. Whilst the drive is responsible for the momentum of the drop, it is surface tension that it responsible for the break-off from the nozzle and is found to be proportional to the Rayleigh timescale for the growth of capillary instabilities. Indeed, the effect of increasing drop velocity is to increase slightly the break-off time. As a consequence, the length of the ligament behind the drop grows in proportion to the drop speed. The length of this ligament limits the range of drop velocities for which the ligament will retract into the main drop before it breaks up to form satellite drops. For the particular print-head and drive in this study we find that this limits the range of fluids that produce satellite free drops to Reynolds numbers below 10, irrespective of the Ohnesorge number of the fluid. This provides an additional limit of the window of "printable" fluids in addition to the restriction on the values of the Ohnesorge number.

The results also confirm that an Ohnesorge number of around 0.3 is optimal for controlling satellites in DOD printing. Although a larger Ohnesorge number would further stabilise the retracting ligament, the increased viscosity also acts to delay the break-off from the nozzle and so increases the length of the ligament.

Chapter 4

Surfactant Transport and Dynamic Surface Tension

In this chapter, we present the governing equations for the surfactant transport and the concentration-dependent surface tension used in the model, along with their non-dimensionalised form. The finite element formulation and the coupling with the existing model is shown. Finally, details about the coding adaption are shown.

4.1 Governing Equations

4.1.1 Surface equation of state

Changes in surface concentration of surfactant cause surface tension gradients and can significantly affect the break-up dynamics compared to surfactant-free systems. However, an accurate estimation of the surface tension depending on the surfactant concentration can be very complicated.

The surface tension γ depends on the surface concentration Γ of surfactant which lowers the surface tension and is given by an equation of state of the form

$$\gamma = \gamma(\Gamma) \,.$$

Equations of state relating γ and Γ which account for different effects are reviewed in §1.3.3. In this thesis, the Langmuir-Frumkin surface equation of state (1.8) is used because of its simplicity and use in other studies (Chang and Franses, 1995;

Liao et al., 2006, 2004),

$$\gamma = \gamma_p + \mathcal{R}T\Gamma_\infty \ln\left(1 - \frac{\Gamma}{\Gamma_\infty}\right).$$ (4.1)

For the rest of the chapter, γ_p is the pure solvent surface tension (clean interface), $\mathcal{R}$ is the gas constant $8.134\,\mathrm{J\,mol^{-1}\,K^{-1}}$, Γ_∞ is the maximum packing concentration value $(\mathrm{mol\,m^{-2}})$ and T is the absolute temperature (K).

4.1.2 Surfactant transport equations

Surfactants move along the evolved interface of the jet. The interface deformation and the flow-induced changes in the jet break-up lead to a non-uniform surfactant distribution along the interface.

The surface density of surfactants at a point on the interface will evolve due to the surface flow, the deformation of the surface, the diffusion of surfactant molecules on the surface and the bulk-interface exchange (in the case of a soluble surfactant).

The governing equation for the surfactant transport on the liquid-gas interface is the time-dependent advection-diffusion equation (Stone, 1990; Stone and Leal, 1990),

$$\frac{\partial \Gamma}{\partial t} + \nabla_s \cdot (\Gamma \mathbf{u}) + \nabla_s \cdot \jmath = b,$$ (4.2)

where $\Gamma(z, t)$ is the surface concentration of surfactant, $\jmath$ is the flux along the interface, considered here as the Fickian flux given by

$$\jmath = -D_s \nabla_s \Gamma,$$ (4.3)

where D_s is the surfactant surface diffusivity $(\mathrm{m^2\,s^{-1}})$, ∇_s is the gradient operator and b is the net flux of surfactants to and from the interface from and to the bulk phase. In the case of insoluble surfactant the bulk exchange will be zero, so $b = 0$.

4.2 Non-dimensional Equations

Dividing equation (4.1) by γ_p, we obtain the surface tension relative to the pure solvent in the form

$$\gamma = 1 + \beta \ln\left(1 - \frac{\Gamma}{\Gamma_\infty}\right),$$ (4.4)

where

$$\beta = \frac{\Gamma_\infty RT}{\gamma_p} \tag{4.5}$$

provides a measure for the strength of the surfactant.

The surfactant concentration is non-dimensionalised by the equilibrium surface surfactant concentration of the solution Γ_{eq},

$$C = \frac{\Gamma}{\Gamma_{\mathrm{eq}}} \, . \tag{4.6}$$

This introduces a non-dimensional parameter

$$K = \frac{\Gamma_{\mathrm{eq}}}{\Gamma_\infty} \, , \tag{4.7}$$

the ratio of the equilibrium surfactant concentration on the surface, which is a measure of the surfactant concentration of the solution. Hence, equation (4.4) becomes

$$\gamma = 1 + \beta \ln(1 - KC) \, . \tag{4.8}$$

For the surfactant transport equation (4.2), using equations (4.3) and (4.6) and dividing by the length scale R_N, the nozzle radius, and velocity scale U, the drop speed, we have

$$\frac{\partial \Gamma}{\partial t} + \nabla_s \cdot (\Gamma \mathbf{u}) - D_s \nabla_s^2 \Gamma = b \Rightarrow$$
$$\frac{\mathrm{D}_s C}{\mathrm{D}_s t} - \frac{1}{\mathrm{Pe}} \nabla_s^2 C = B, \tag{4.9}$$

where $\mathbf{x}$ and t are now in dimensionless units, B is the dimensionless bulk exchange rate and Pe is the surface Péclet number given by

$$\mathrm{Pe} = \frac{R_N U}{D_s} \, , \tag{4.10}$$

which determines the importance of convection of surfactant relative to its diffusion along the free surface. Here $\dfrac{\mathrm{D}_s}{\mathrm{D}_s t}$ is defined as the derivative in the Lagrangian frame of the surface

$$\frac{\mathrm{D}_s f}{\mathrm{D}_s t} = \frac{\partial f}{\partial t} + \nabla_s \cdot (\mathbf{u} f)$$

and includes the dilation as well as the advection of the surface.

$$\begin{bmatrix} \text{first node on first domain} & \\ \quad \text{on symmetry line,} & \text{first node on free surface} \\ \text{first node on free surface,} & \text{second node on free surface} \\ \text{second node on free surface,} & \text{third node on free surface} \\ \vdots & \vdots \\ \text{last node on first domain} & \\ \quad \text{on free surface,} & \text{node on symmetry line} \\ \text{first node on second domain} & \text{first node on second domain} \\ \quad \text{on symmetry line,} & \quad \text{on free surface} \\ \vdots & \vdots \end{bmatrix}$$
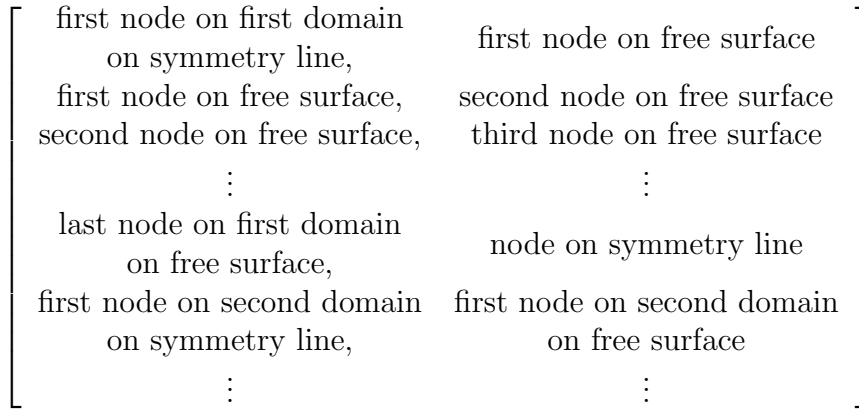
Figure 4.2: Schematic of the edge structure used in the code. Each row contains the left and right hand side node of each edge.

4.3 Structure for Surfactants on the Interface

As described in chapter 2, the code used in this thesis derived from Morrison and Harlen (2010); Harlen et al. (1995) uses axisymmetric finite elements in which the nodes advect with the flow. In order to include the transport of surfactant molecules on the free surface, a new data structure needs to be introduced. While variables such as velocity and pressure are stored at the nodes, it is more natural for the number surfactant molecules to be stored on the edges. An edge is defined as the connection between two nodes on the free surface.
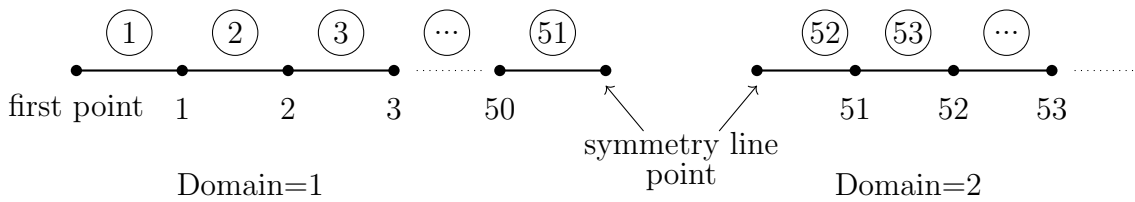
Figure 4.1: Edge and node numbering system on the free surface.

As the ejected fluid breaks up into satellite drops, the free surface is broken into a number of different domains. With the exception of the first domain of fluid connected to the nozzle, each domain begins and ends with a point on the symmetry line, see figure 4.1, with the free surface points numbered consecutively in between. The edge structure is stored in a $1 \times N_u$ array, where N_u is the number of nodes, that records the left and right-hand side nodes of the edge. The edge array has the following structure: The surfactant distribution is stored in a 1D array, a vector

where each index corresponds to an edge along the free surface.

4.4 Surfactant Distribution and Conservation on the Interface

A key property of the Lagrangian finite element scheme is that the nodes move with the fluid velocity (Harlen et al., 1995). Therefore, the dilation and advection of the surface is handled by the motion of the nodes.
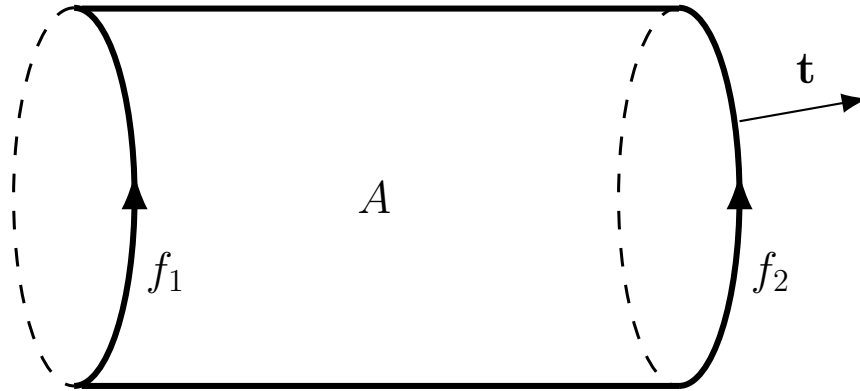
Figure 4.3: Sketch showing the domain of integration over a surface element. Using the divergence theorem on an element on the surface, we have the integral in equation (4.11). $\mathbf{t}$ is the unit tangent vector, f_1, f_2 are the circular contours corresponding to the boundary of the surface element A.

Integrating equation (4.2) over the surface corresponding to the edge between points (r_1, z_1) and (r_2, z_2), for the cylindrical coordinate system, gives

$$\frac{\mathrm{d}}{\mathrm{d}t} \int_A C \, \mathrm{d}A + \int_{f_2} \boldsymbol{\jmath} \cdot \mathbf{t} \, \mathrm{d}S - \int_{f_1} \boldsymbol{\jmath} \cdot \mathbf{t} \, \mathrm{d}S = \int_A b \, \mathrm{d}A, \tag{4.11}$$

where $\mathbf{t}$ is the unit tangent along the free surface curve, as seen in figure 4.3. Hence defining

$$2\pi N = \int_A C \, \mathrm{d}A$$

as the number of surfactant molecules on the edge, the evolution of the surfactant distribution is given by

$$\frac{\mathrm{d}N}{\mathrm{d}t} + J_2 - J_1 = B, \tag{4.12}$$

where

$$J_i = r_i D_s \mathbf{t} \cdot \nabla_s C \tag{4.13}$$

and

$$2\pi B = \int_A b \, \mathrm{d}A \,.$$

In order to determine the surfactant concentration along the interface, the "area" of each edge is computed. The coordinate system is axisymmetric and so the area $2\pi A$ is computed as

$$A = (r_1 + r_2)\sqrt{(r_2 - r_1)^2 + (z_2 - z_1)^2}, \tag{4.14}$$

where r_i, z_i is the left-hand side node ($i = 1$) and the right-hand side node ($i = 2$) coordinates of the edge.

Due to the Langrangian nature of the mesh, in the absence of diffusion (and for $\beta = 0$) the number of surfactant molecules N on each edge remains constant. Hence surface concentration of surfactants is given by

$$C = \frac{N}{A} \,, \tag{4.15}$$

for each edge. We denote with N the number of surfactant molecules on each edge and with A the area of each edge.

When the distance between two nodes is larger than a desirable value (presented and explained in §2.2.1), a new node is added between these two nodes. This splits the edge into two new edges. In order to conserve the number of surfactant molecules and therefore the surfactant concentration, a surfactant share procedure is applied. Let us denote by N_0, A_0, C_0 the number of surfactant molecules, the area and the concentration of the original edge and by N_i, A_i, C_i, $i = 1, 2$ the new edges after adding the point in the middle of the original edge, as shown in figure 4.4
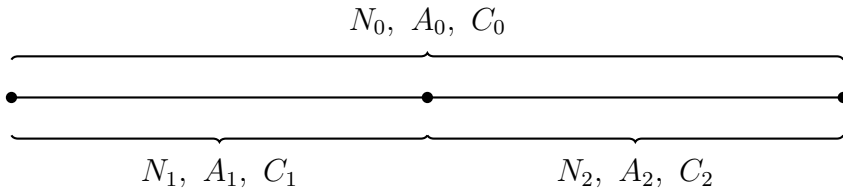
Figure 4.4: Edge splitting when a node needs to be added.

In order to preserve the number of surfactant molecules we need the concentration of the original edge to be the same as the concentration of edge 1 and the same as the concentration of edge 2,

$$C_0 = C_1 = C_2.$$
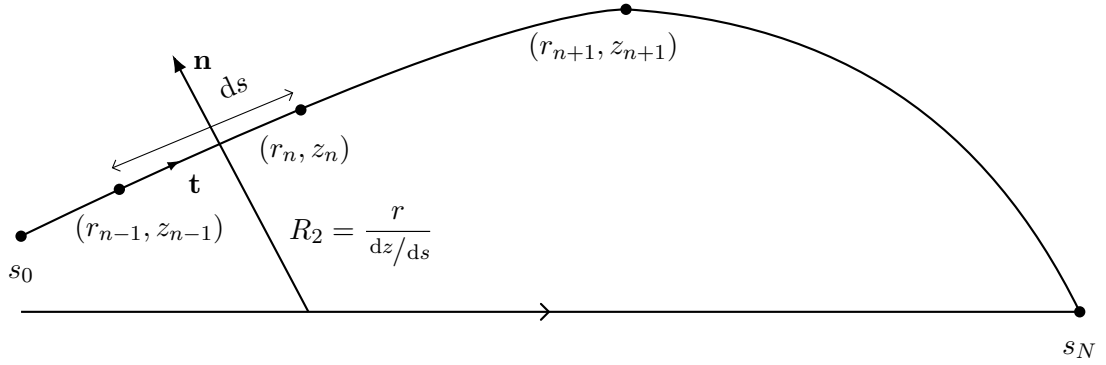
Figure 4.5: Free surface and unit vectors, where tangential vector $\mathbf{t}$, normal vector $\mathbf{n}$ to the surface, radial coordinate r, axial coordinate z, radius of curvature R_2 and s is the contour length of the surface.

This is achieved by assigning the number of surfactants on the new edges as

$$N_1 = \frac{A_1}{A_0} N_0, \quad N_2 = \frac{A_2}{A_0} N_0. \tag{4.16}$$

In the opposite case, when the distance between two nodes is smaller than a desirable value, one of these nodes is removed. This leads to the merger of two edges with the sum of the surfactant number from the two original edges assigned to the merged edge.

Both cases require careful book keeping to ensure that the lists of edges are correctly maintained. This is verified by calculating the total number of surfactants before and after any addition or removal of edges to ensure conservation of surfactants.

4.5 Finite Element Formulation for Dynamic Surface Tension

In the presence of variable surface tension, the surface force on the air-ink interface is given by

$$[\mathbf{n} \cdot \boldsymbol{\sigma}]_{\text{surface}} = -\frac{\gamma}{\text{We}} \mathbf{n} \nabla_s \cdot \mathbf{n} + \frac{1}{\text{We}} \nabla_s \gamma. \tag{4.17}$$

The tangential and normal vector to the surface, $\mathbf{t}$ and $\mathbf{n}$ respectively are

given by

$$\mathbf{t} = \left(\frac{\mathrm{d}z}{\mathrm{d}s}, \frac{\mathrm{d}r}{\mathrm{d}s} \right) \tag{4.18}$$

$$\mathbf{n} = \left(\frac{\mathrm{d}r}{\mathrm{d}s}, -\frac{\mathrm{d}z}{\mathrm{d}s} \right), \tag{4.19}$$

see §2.3.1 where the constant surface tension case is discussed. The curvature is given by

$$\left(\nabla_s \cdot \mathbf{n} \right) \mathbf{n} = -\frac{\mathrm{d}\mathbf{t}}{\mathrm{d}s} + \frac{\mathbf{n}}{R_2}.$$

Hence equation (4.17) can be rewritten as

$$\begin{aligned}
\left[\mathbf{n} \cdot \boldsymbol{\sigma} \right]_{\text{surface}} &= \frac{1}{\mathrm{We}} \left(\gamma \frac{\mathrm{d}\mathbf{t}}{\mathrm{d}s} - \frac{\mathbf{n}}{R_2} + \mathbf{t} \frac{\mathrm{d}\gamma}{\mathrm{d}s} \right) \\
&= \frac{1}{\mathrm{We}} \left[\frac{\mathrm{d}}{\mathrm{d}s} \left(\gamma \mathbf{t} \right) - \gamma \frac{\mathbf{n}}{R_2} \right].
\end{aligned} \tag{4.20}$$

Note that equation (4.20) also contains the constant surface tension case.

As in the case of constant surface tension, the momentum equation is given by equation (2.6). However, we need to modify the surface boundary condition by substituting equation (2.4) in equation (2.13). For the weak formulation of the normal stress balance, we multiply equation (4.20) with the basis function ϕ_n and integrate over the surface in cylindrical coordinates. Thus, the modified version of equation (2.15) becomes

$$\begin{aligned}
\int_S \left(\mathbf{n} \cdot \boldsymbol{\sigma} \right) \phi_i r \, \mathrm{d}s \, \mathrm{d}\theta &= -\frac{2\pi}{\mathrm{We}} \left(\int_{s_0}^{s_N} \gamma \frac{\mathbf{n}}{R_2} r \phi_n \, \mathrm{d}s - \int_{s_0}^{s_N} \frac{\mathrm{d}}{\mathrm{d}s} \left(\gamma \mathbf{t} \right) \phi_i r \, \mathrm{d}s \right) \\
&= -\frac{2\pi}{\mathrm{We}} \left(\int_{s_0}^{s_N} \gamma \frac{\mathrm{d}z}{\mathrm{d}s} \mathbf{n} \phi_i \, \mathrm{d}s + \int_{s_0}^{s_N} \gamma \mathbf{t} \frac{\mathrm{d}}{\mathrm{d}s} \left(r \phi_i \right) \mathrm{d}s - \left[\gamma \mathbf{t} r \phi_i \right]_{s_0}^{s_N} \right),
\end{aligned} \tag{4.21}$$

where s_0, s_N are the beginning and end points of the free surface. Note that the contribution from the end points is zero in our case as the point s_0 is part of the nozzle boundary so that ϕ_i is zero there for all velocity unknowns, and the other end s_N is located on the axis so that $r = 0$.
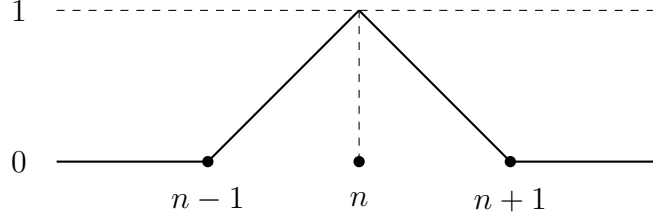
Figure 4.6: Sketch of the basis function ϕ_n at a surface node.

The final term is zero in our case as the point s_0 is part of the nozzle boundary and the basis function ϕ_n is zero for all velocity unknowns. In addition, s_N is at the last point on the surface located at the symmetry line and so $r = 0$.

The integrals in equation (4.21) are the same as in the constant surface tension case, described in §2.2.3. For points on the surface, ϕ_n is non-zero only on the two edges connected to point n, as shown in figure 4.6. The basis function ϕ varies linearly with s as follows

$$\phi = \begin{cases} \dfrac{s - s_{n-1}}{s_n - s_{n-1}}, & \text{in } [s_{n-1},\ s_n] \\ \dfrac{s_{n+1} - s}{s_{n+1} - s_n}, & \text{in } [s_n,\ s_{n+1}]. \end{cases} \tag{4.22}$$

Moreover on each edge $\dfrac{r}{R_2} = \dfrac{\mathrm{d}z}{\mathrm{d}s}$ is constant, as is $\gamma\mathbf{n}$ therefore the first integral $\int_{s_0}^{s_{N_u}} \gamma \frac{\mathbf{n}}{R_2} \phi_n r \,\mathrm{d}s$ can be evaluated as

$$\begin{aligned}
\int_{s_0}^{s_{N_u}} \gamma \frac{\mathbf{n}}{R_2} \phi_n r \,\mathrm{d}s \quad &= \int_{s_{n-1}}^{s_n} \gamma_- \frac{\mathbf{n}_-}{R_2} \phi_n r_- \,\mathrm{d}s + \int_{s_n}^{s_{n+1}} \gamma_+ \frac{\mathbf{n}_+}{R_2} \phi_n r_+ \\
&= \gamma_- \mathbf{n}_- \frac{\mathrm{d}z_-}{\mathrm{d}s_-} \int_{s_{n-1}}^{s_n} \phi_n \,\mathrm{d}s + \gamma_+ \mathbf{n}_+ \frac{\mathrm{d}z_+}{\mathrm{d}s_+} \int_{s_n}^{s_{n+1}} \phi_n \,\mathrm{d}s \\
&= \gamma_- \mathbf{n}_- \frac{\mathrm{d}z_-}{\mathrm{d}s_-} \frac{1}{2} \Delta s_- + \gamma_+ \mathbf{n}_+ \frac{\mathrm{d}z_+}{\mathrm{d}s_+} \frac{1}{2} \Delta s_+ \\
&= \tfrac{1}{2} \gamma_- \mathbf{n}_- \Delta z_- + \tfrac{1}{2} \gamma_+ \mathbf{n}_+ \Delta z_+ , \tag{4.23}
\end{aligned}$$

where $\Delta s_- = s_n - s_{n-1}$, $\Delta s_+ = s_{n+1} - \Delta s_n$ and $\gamma_{-,+}$ is the surface tension on each edge, which is determined from the surfactant concentration on the edge.

We will now focus on the second integral, $\int_{s_0}^{s_{N_u}} \gamma \mathbf{t} \frac{\mathrm{d}}{\mathrm{d}s} (r\phi_n) \,\mathrm{d}s$. Here, $\gamma \mathbf{t}$ is

constant on each edge so that

$$
\begin{aligned}
\int_{s_0}^{s_{Nu}} \gamma \mathbf{t} \frac{\mathrm{d}}{\mathrm{d}s} \left(r\phi_n \right) \mathrm{d}s &= \int_{s_{n-1}}^{s_n} \gamma \mathbf{t} \frac{\mathrm{d}}{\mathrm{d}s} \left(r\phi_n \right) \mathrm{d}s \\
&\quad + \int_{s_n}^{s_{n+1}} \gamma \mathbf{t} \frac{\mathrm{d}}{\mathrm{d}s} \left(r\phi_n \right) \mathrm{d}s \\
&= \gamma_- \mathbf{t}_- \left[r\phi_n \right]_{s_{n-1}}^{s_n} + \gamma_+ \mathbf{t}_+ \left[r\phi_n \right]_{s_n}^{s_{n+1}} \\
&= r_n \left(\gamma_- \mathbf{t}_- - \gamma_+ \mathbf{t}_+ \right) .
\end{aligned}
\tag{4.24}
$$

Hence, the normal stress balance force for the dynamic surface tension equation (4.17) in weak formulation is given by

$$
\frac{\mathrm{We}}{2\pi} \int_S \left(\mathbf{n} \cdot \boldsymbol{\sigma} \right) \phi_n r \, \mathrm{d}s \, \mathrm{d}\theta = -\frac{1}{2} \left(\gamma_- \mathbf{n}_- \Delta z_- + \gamma_+ \mathbf{n}_+ \Delta z_+ \right) + r_n \left(\gamma_+ \mathbf{t}_+ - \gamma_- \mathbf{t}_- \right) , \tag{4.25}
$$

where $\Delta z_- = z_n - z_{n-1}$, $\Delta z_+ = z_{n+1} - \Delta z_n$ and $\gamma_{-,+}$ is the surface tension on edges connected to point n. As we can see from equation (4.25), the only thing we need is the surface tension on each edge which is calculated using equation (4.8), so consequently we just need the number of surfactant molecules on each edge.

4.6 Surfactant Diffusion Along the Interface

For the case of an insoluble surfactant for which $B = 0$ from equation (4.12), the number of surfactants on an edge N changes only as a result of diffusion along the interface. From equation (4.13) the flux J at a node between adjacent edges is given by

$$
J = -\frac{r}{\mathrm{Pe}} \frac{\partial C}{\partial S} ,
$$

where S is the path length along the surface.

4.6.1 Diffusion explicit scheme

Using a simple finite difference scheme we have that

$$
\frac{\partial C}{\partial S} = \frac{(C_+ - C_-)}{S_+ - S_-} = \frac{2(C_+ - C_-)}{\Delta S_+ + \Delta S_-} . \tag{4.26}
$$

Here, S is calculated as

$$S_+ = S + \frac{\Delta S_+}{2} \,, \tag{4.27a}$$

$$S_- = S - \frac{\Delta S_-}{2} \,, \tag{4.27b}$$

$$\Delta S_+ = \sqrt{(r_+ - r)^2 + (z_+ - z)^2} \,, \tag{4.27c}$$

$$\Delta S_- = \sqrt{(r_- - r)^2 + (z_- - z)^2} \,, \tag{4.27d}$$

$$\tag{4.27e}$$

where ΔS is the length of the edge so that

$$S_+ - S_- = \frac{1}{2}\sqrt{(r_- - r)^2 + (z_- - z)^2} + \sqrt{(r_+ - r)^2 + (z_+ - z)^2} \,. \tag{4.28}$$
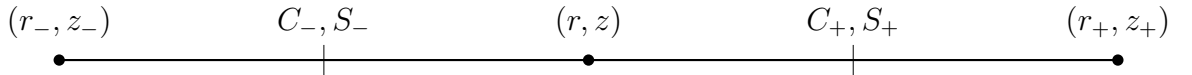
Figure 4.7: Concentration on the edges on the free surface, where r, z is the radial and axial co-ordinate respectively, C is the surface surfactant concentration and S is the contour length.

Hence by equation (4.3) we get

$$J = -\frac{2r}{\text{Pe}} \frac{(C_+ - C_-)}{S_+ - S_-} \,, \tag{4.29}$$

where here C is the concentration from the previous time-step. Since we calculate number of surfactant molecules in the simulations we compute flux as

$$J = -\frac{2r}{\text{Pe}} \left[\frac{N_+/A_+ - N_-/A_-}{S_+ - S_-} \right] \,. \tag{4.30}$$

This is computed every time-step after the positions of the nodes have been updated in the Lagrangian time-step.
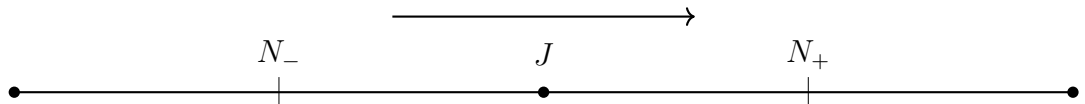
Figure 4.8: Surfactant flux between two edges. Whether the surfactants are moved from or to edge + depends on the sign of the flux which depends on the surface concentration gradient.

In contrast to the number of surfactant molecules and the area, the flux

is computed at each node. This flux is then added to the edge on the right-hand side and subtracted from the edge on the left-hand side so that the numbers of surfactants are modified as

$$N_-^{\text{new}} = N_-^{\text{old}} - J\Delta t \tag{4.31a}$$

$$N_+^{\text{new}} = N_+^{\text{old}} + J\Delta t, \tag{4.31b}$$

as seen in figures 4.7 and 4.8.

The initial condition is chosen so that initial number of surfactants molecules on the edges gives an initial concentration equal to the equilibrium concentration, so that $C = 1$.

4.6.2 Maximum packing concentration and surfactant transport

For a typical surfactant, the surface diffusivity $D_s = 5 \times 10^{-10}$ m^2 s^{-1} yields to a surface Péclet number Pe $= 2 \times 10^5$ for inkjet printing. Hence the transport of surfactant is dominated by surface advection. Although overall the jetting process leads to an overall dilation of the free surface and hence a reduction in surfactant concentration, locally there are areas where the surface area is contracting. This can lead to situations where the local concentration exceeds the maximum packing concentration Γ_∞ of surfactants. This unphysical situation gives rise to the resultant surface tension becoming zero or even negative in equation (4.1) and is outside the range for which the equation of state is applicable. In reality, strong repulsive forces between the surfactant molecules would prevent this from happening.

When the interface is fully covered with surfactants, any attempt for a concentration higher than the maximum packing will cause surfactants to move to the bulk. In order to prevent this issue, a check needs to be made at every advection time-step to ensure that the concentration in each edge remains below the maximum packing concentration, as otherwise surfactants need to be moved away from that edge.

These issues occur in very small edges on the mesh where even a small amount of surfactant can result in a very high concentration due to the small area. This problem has been observed only at the two edges at the tip of the droplet head, whereas we will present later, there is a high concentration of surfactants compared to the rest of the droplet and the surface area of the edges is small.

As this only happens in very small regions, rather than adjusting the surfactant transport, we modify the equation of state such that

$$\gamma = 1 + \beta \ln(1 - KC) \text{ for } C < C_m\,,$$
$$\text{and } \gamma = \gamma_{\text{eq}} \text{ otherwise,}$$

where C_m is defined such that

$$\gamma_{\text{eq}} = 1 + \beta \ln(1 - KC_m)\,.$$

4.7   Resolution and Accuracy

In order to test the implementation of the algorithm, in figure 4.9 the results from the Newtonian case model presented in chapter 2 for water are compared with the new model presented here for a surfactant with strength $\beta = 0$. In this limit, there is no effect on the surface tension from the surfactants and therefore we have a constant surface tension. As we can see, the results are identical, as expected.
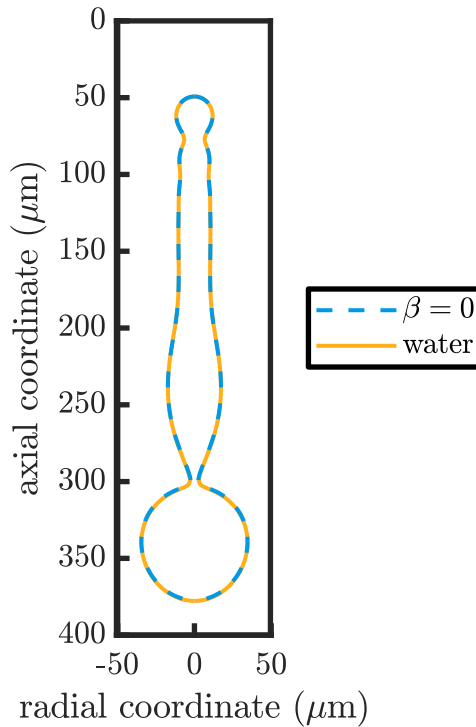
Figure 4.9: Simulation results comparing Newtonian code with $\beta = 0$. The implementation of the surfactant effect shows the same results as the Newtonian code giving confidence that the implementation of the surface tension in the weak formulation has not altered the result in a non-meaningful way.
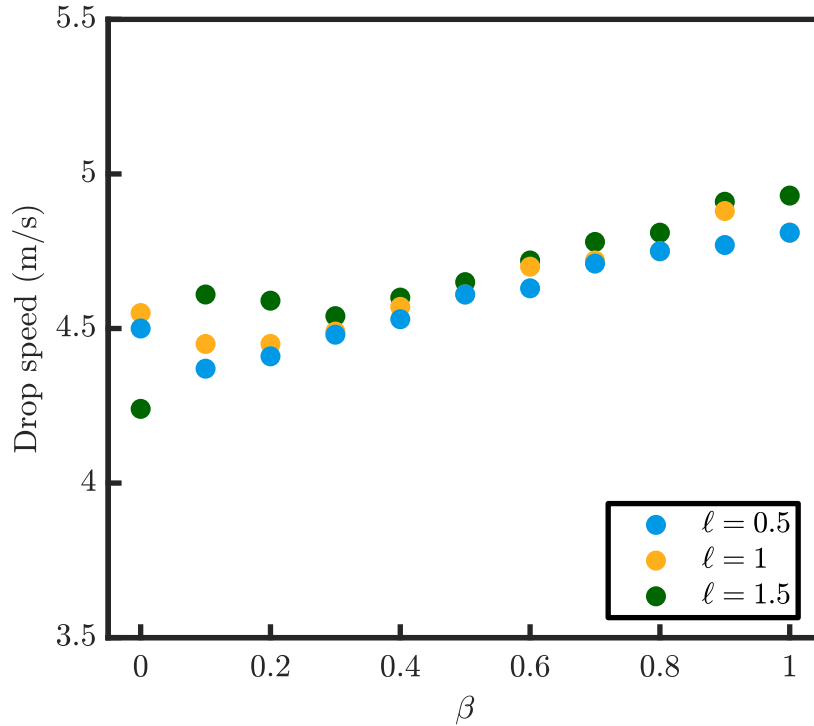
Figure 4.10: Drop speed measurements from numerical simulations using different mesh resolutions for different surfactant strengths β. The relative error between the reference mesh and the fine mesh is always smaller than 2%. There is also a small increase in the drop speed with increasing surfactant strength; with the difference between the weakest ($\beta = 0.1$) and the strongest surfactant ($\beta = 1$) of 10%.

To test the effect of the spatial resolution on the accuracy of the calculations, we performed simulations with three different mesh resolutions. The resolution of the mesh is characterised by the parameter ℓ, which scales the maximum length allowed in the mesh. Thus, the value 1 will correspond to the reference mesh, 0.5 will give a finer mesh with twice the spatial resolution and 1.5 gives a coarser mesh.

In figure 4.10 we examine the drop speed as the representative diagnostic because this variable depends on the initial condition and the break-off time of the system. Comparison between the results for the reference mesh used for this study and the highest resolution mesh gives an error of less than 2%. This implies that the mesh we use is suitable to capture the dynamics of this problem accurately. For the lowest surfactant strength, there is a larger difference between the very coarse mesh and the higher resolution meshes, however we focussed our studies on meshes with enough resolution to make sure we avoid any numerical errors in the lowest resolution.

Another comparison is to compare the surface shape at a given time for different mesh resolutions. For surfactant strength $\beta = 0.4$ and the different mesh
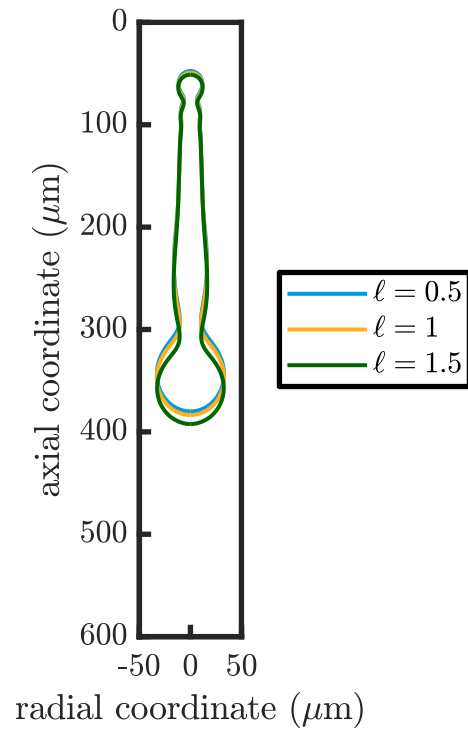
Figure 4.11: Surface outline for $\beta = 0.4$ surfactant strength for different mesh resolutions.

resolutions used before, we see that the shape outline is almost identical for the normal and fine mesh, whereas for the coarse mesh there is a small difference mainly due to the faster drop speed. We use the normal mesh for our studies, as we have shown that further refinement gives very similar results.

Chapter 5

Drop-on-Demand Jetting of Surfactant Solutions

In this chapter, the surfactant distribution along the forming jet is investigated using numerical simulations of the mathematical framework presented in chapter 4. A typical serial simulation of the full jetting process with the addition of surfactants required approximately clock time of 2 to 3 hours, using one core on a Linux desktop PC containing Intel(R) Xeon(R) CPU E3-1240 v5 at 3.5 GHz processor. We present results for different strength surfactants, showing its importance in the non-uniform surfactant concentration on the jet which gives rise to Marangoni forces. In turn, Marangoni effects affect the surface evolution and therefore the dynamics of the jet break-up. We examine the thinning rate of the neck radius as a function of surfactant strength. Finally, a jetting behaviour analysis based on the surfactant strength is made, where we present an example case in which the addition of a strong surfactant prevents the formation of satellites, resulting in a good jetting behaviour.

5.1   Diffusion During Drop-on-Demand Printing

In this section, we will look in more detail at the diffusion of the surfactants on the interface. Surfactants are treated as being effectively insoluble in this work, therefore there is no bulk exchange in our numerical model, i.e. $B = 0$ in equation (4.9). Nevertheless, we will show that this assumption can be applied to soluble surfactant systems over the timescales involved in inkjet printing.

5.1.1 Derivation of diffusion time for surfactant adsorption

In order to estimate the timescale for diffusion limited equilibration of the surface concentration, we consider the case shown in figure 5.1 where a surfactant-free surface is created at time $t = 0$ so that $\Gamma(0) = 0$. Here, Γ is the surfactant concentration on the interface and c is the concentration near the sub-phase.

Monomeric surfactants are adsorbed in the interface, while there is still space for them, from the bulk. This gives rise to a flux, j. From conservation of mass we have at the interface

$$j|_{z=0} = \frac{d\Gamma}{dt} \, .$$

The bulk diffusion of surfactant is modelled using the unsteady form of Fick's law of diffusion

$$j = D\frac{\partial c}{\partial z} \, . \tag{5.1}$$

Therefore, we have

$$D\frac{\partial c}{\partial z}\bigg|_{z=0} = \frac{d\Gamma}{dt} \, ,$$

which can be seen as a flux condition at the interface.
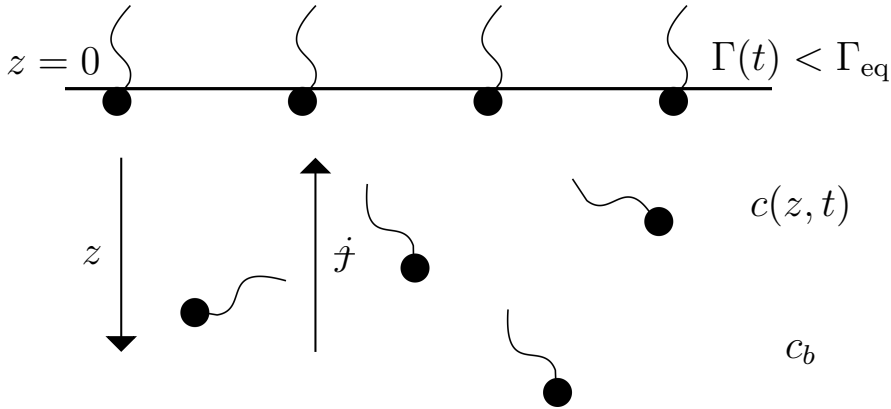
Figure 5.1: Schematic representation of the diffusion occuring near the subphase. The subphase has a width given by the depletion depth. j is the flux of the surfactant molecules from the bulk to the interface. c_0 and Γ_{eq} are the equilibrium concentrations of the bulk and the surface respectively.

Far from the interface, a Dirichlet boundary condition applies, where $c_{z\to\infty} = c_b$ and we have an initial condition $\Gamma(t = 0, z = 0) = 0$, which corresponds to a clean interface. For the bulk, we have that the concentration is determined by solving the bulk diffusion equation

$$\frac{\partial c}{\partial t} = D\frac{\partial^2 c}{\partial z^2}.$$

This equation with the initial conditions

$$c = c_0, \ z > 0,$$
$$c = 0, \ \text{on } z = 0$$

is a well-known established initial-value problem with solution

$$c = c_0 \operatorname{erf}\left(\frac{z}{2\sqrt{Dt}}\right).$$

By differentiating with respect to z we have that

$$\frac{\partial c}{\partial z} = \frac{c_0}{\sqrt{\pi Dt}} \exp\left(-\frac{z^2}{4Dt}\right)$$

and by substituting into equation (5.1) we get

$$\dot{\jmath} = D\frac{\partial c}{\partial z}\bigg|_{z=0} = c_0\sqrt{\frac{D}{\pi}}\frac{1}{\sqrt{t}} = \frac{d\Gamma}{dt}\bigg|_{t=0}$$
$$\frac{d\Gamma}{dt} = c_0\sqrt{\frac{D}{\pi}}\frac{1}{\sqrt{t}} \Rightarrow$$
$$\Gamma(t) = 2c_0\sqrt{\frac{D}{\pi}}\sqrt{t} \Rightarrow$$
$$\Gamma^2(\tau_D) = 4c_0^2\frac{D}{\pi}\tau_D \Rightarrow$$

$$\tau_D = \left(\frac{\Gamma}{c}\right)^2\frac{\pi}{4D}, \tag{5.2}$$

where τ_D is the diffusion time, using the initial condition $\Gamma(t = 0) = 0$. This relationship can be thought of as the mean time taken by a surfactant molecule to diffuse a distance given by the depletion length $h = \Gamma_{\text{eq}}/c$.

Here, we note that this calculation is for a planar interface and is strictly valid only near $t = 0$. Thus it assumes that the depletion depth $h_p = \Gamma/c$ (cf. equation (1.9)) is small compared to the radius of the jet, as seen and explained in §1.3.4. In the following section, we show why this assumption holds in inkjet applications.

5.1.2 Diffusion timescale compared to break-off time

In equation (5.2), we derived the formula for the diffusion time in the planar case. In our experiments, we used Triton X-100 as the surfactant. The conditions of the

experiments correspond to the parameters:

$$D \approx 2.6 \times 10^{-10} \text{ m}^2\text{s}^{-1},$$
$$\Gamma_{\text{eq}} = 2.9 \times 10^{-6} \text{ mol m}^{-2},$$
$$c_b = 0.22 \text{ mol m}^{-3}.$$

These give an estimated depletion depth is h_p =13.18 μm which is half the jet diameter (25 μm). Using equation (5.2), the diffusion time is around 0.52 s. This time is 3×10^3 larger compared to the break-off time observed in our experiments. Moreover this timescale is based on the assumption of a planar interface and the diffusion time will be slower for a curved surface as discussed in §1.3.4.

One of the most commonly used surfactants in inkjet printing applications is Surfynol 465 and it has been studied in the literature for its chemical properties and the effect on dynamic surface tension and the instability of a liquid jet (Yang and Bain, 2009; Yang et al., 2014). The values estimated in these studies for the diffusion coefficient, the equilibrium concentration and the bulk surfactant concentration used in these experiments are

$$D \approx 3 \times 10^{-10} \text{ m}^2\text{s}^{-1},$$
$$\Gamma_{\text{eq}} = 1.4 \times 10^{-6} \text{ mol m}^{-2},$$
$$c_b = 11.3 \text{ mol m}^{-3}.$$

Surfynol 465 has a much higher solubility than Triton X-100 and using these values in equation (1.9), we can estimate that the depletion length is approximately 100 nm. Comparing this with the jet radius, which is of the order of micrometers (13 μm for Ricoh nozzle) in inkjet printing scales, we see that the assumption of a planar interface is valid for the lengthscales relevant to inkjet drop formation.

Now from equation (5.2), the lowest estimation for the diffusion time is around 40 μs. For a simple Newtonian fluid, using the parameters of the Ricoh experiments §3.3, our numerical model gives a break-off time of approximately 40 μs, as seen in figure 3.9, so for Surfynol 465 there will be some adsorption of the surfactant from the bulk to the interface.

The difference in the depletion depths for these two surfactants can be explained from the differences in solubility. Triton X-100 has a very low CMC of 0.22 mol m^{-3} showing that it is highly insoluble compared to Surfynol 465 whose CMC is equal to 11.3 mol m^{-3}.

5.2 Experimental Details

As in the case of the simple Newtonian fluids, experiments are conducted to validate our model. Since experiments for directly measuring the surfactant concentration in a dynamic framework are not possible, we based our validation on the jetting behaviour as well as properties of the jetting process such as break-off time and ligament length.

This work is part of the collaboration with Maaike Rump, Dr Tim Segers and Prof Detlef Lohse from the Physics of Fluids (POF) group, at University of Twente (Twente, the Netherlands), where the experiments were performed during a placement visit.
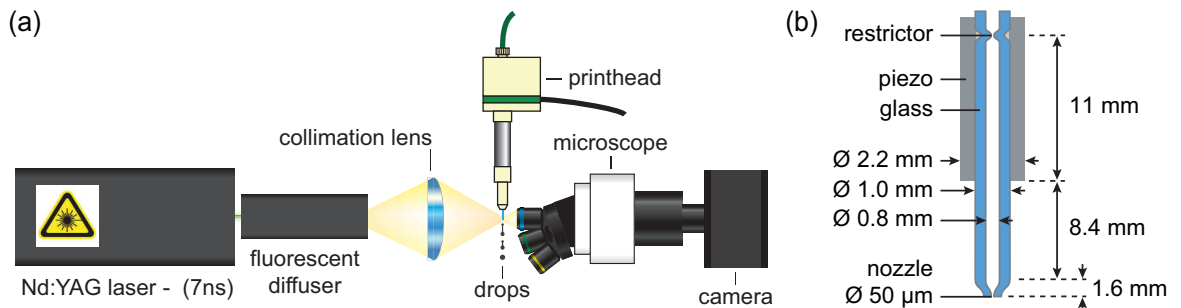
Figure 5.2: Schematic of the experimental setup, provided by Physics of Fluids group, University of Twente

A 50 µm diameter Autodrop Pipette from Microdrop Technologies GmbH (AD K-501 and AD-H-501) is used. More details about this type printhead can be found in (Dijksman, 1984, 1998).

All experiments were performed at room temperature. The surfactant solutions were supplied from a plastic syringe to the top of the Autodrop Pipette holder via flexible plastic PEEK tubing (Upchurch Scientific) and the meniscus was positioned at the nozzle exit by manually adjusting the piston of the syringe.

The model was compared to experiments performed at room temperature on a 50 µm diameter single nozzle printhead (AD K-501 and AD-H-501, Microdrop Technologies GmbH). Aqueous surfactant solutions were supplied from a rubber-free plastic syringe to the printhead via flexible PEEK tubing (Upchurch Scientific). Before the jetting experiments, the meniscus was positioned at the nozzle exit by manually adjusting the piston of the syringe. The printhead was driven by a rectangular waveform with a width of 30 µs and a rise and fall time of 0.2 µs. The waveform was generated by an arbitrary waveform generator (Agilent 33440A) and amplified to an amplitude of 66.4 V by a broadband amplifier (Falco System WMA-300).

The imaging setup is shown in figure 5.2. The setup consisted of a modular microscope (BXFM-F, BXFM-ILHS, Olympus) equipped with a 5 times magnifying objective (MPLFLN, Olympus) and an additional 2 times magnifying lens resulting in an effective magnification of 10 times. The microscope was connected to a CCD camera (Lumenera, Lw135 m, 4.65×4.65 µm² pixels) via a tube lens (U-TLU) resulting in an imaging resolution of 465 nm\pixel. Sufficient illumination was provided via laser-induced fluorescence (iLIF) (van der Bos et al., 2011) using a 7 ns laser light flash (Quantel EverGreen, Nd: YAG, $\lambda = 532$ nm, 7 ns) of which the coherence was removed by a fluorescent diffusor (Lavision, part nr. 118417 and 1003144). The resulting 8 ns incoherent light flash was condensed onto the imaging plane using a lens (2 cm focal distance) and an optical fiber. The waveform generator, the laser, and the camera were triggered with nanosecond precision using a pulse-delay generator (Berkeley Nucleonics Corp., BNC 575). The pulse delay generator was controlled via custom-made software programmed in Labview (National Instruments). To avoid surfactant aggregation due to evaporation at the meniscus and to ensure a uniform surfactant concentration in the bulk liquid behind the meniscus, first, 999 droplets were jetted at a rate of 1000 droplets/s. Subsequently, the jetting process was stopped for 10 ms to allow surfactants to adsorb to the meniscus. After these 10 ms, a next series of 999 droplets was jetted at a frequency of 1000 droplets/s. For each series of 999 droplets, the first droplet was imaged. The imaging software was programmed such that the pulse delay generator increased the delay of the light flash with respect to the piezo actuation pulse by 2 µs for every image. In this manner, the droplet formation process was recorded stroboscopically at the extremely short exposure time of 8 ns.

In order to determine the form of the drive waveform used in the experiments, we use the meniscus position inside the nozzle. It can be seen (in figures 5.3 and 5.4) that there is very good agreement between the experiments and the simulations. In particular, both the pinch-off and the break-off event are captured accurately by the simulations.

In figures 5.3 and 5.4, we compare snapshots at the pinch-off from the nozzle and at a later time after the break-off of the head droplet from the ligament for the pure water and the water-Triton X-100 solution. For the Triton-X simulations, we use a value for $\beta = 0.1$ which was estimated using the value of the equilibrium surface tension (Robinson et al., 2014) and $K = 1$ since the bulk concentration is at the CMC which gives a full covered meniscus at the initial resting stage. We note that here the major uncertainty in the comparison is the precise form of the driving waveform and any effect of the acoustics on the meniscus. Although we can observe some small differences, overall there is good agreement between the experiments and

(a) $t = 140$ µs   (b) $t = 168$ µs
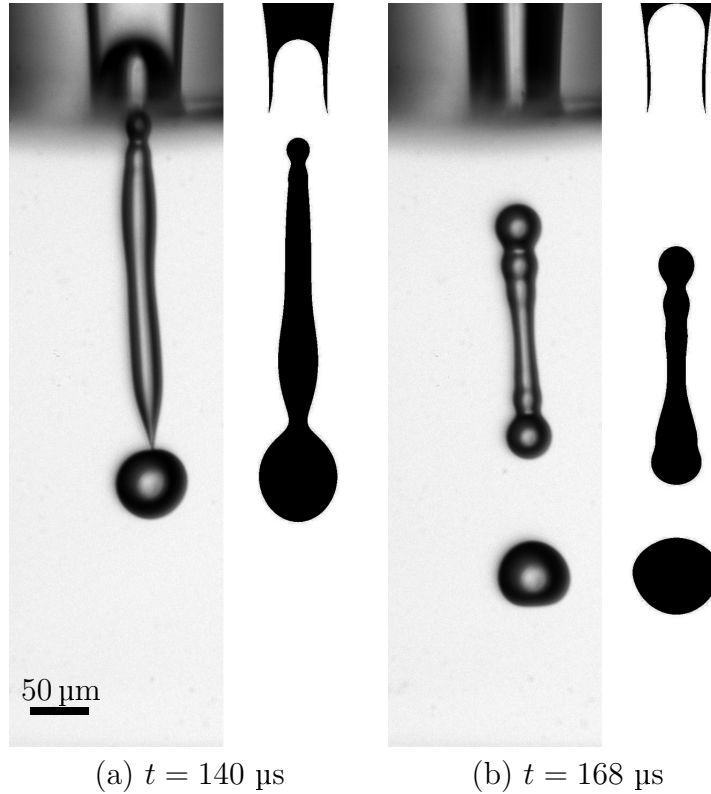
Figure 5.3: Comparison between experiments (grey background) and simulations (white background) with water at different times for a prescribed drop speed of $4\,\mathrm{m\,s^{-1}}$ (a) at pinch-off from the nozzle $t = 140$ µs and (b) at break-off of the main droplet from the ligament at $t = 168$ µs.

simulations. However, comparing figures 5.3 and 5.4 we observe, that there is very little difference between the pure water and the water-Triton X-100 solution.

The main difference seen in figure 5.3a and figure 5.4a is that the neck connecting the main drop to the ligament is thicker for the case of the surfactant solution as the presence of surfactants slightly retards the thinning break-up of this neck. This difference is also captured in the simulations. The small value of β means that the changes to the break-off are small, both in the simulations and in the experiments. However, the simulations do capture the way in which they are modified.

5.3 Surfactant Distribution and Surfactant Strength

The addition of surfactants in high surface tension solutions, often aqueous based, aims to improve the quality of the jetting behaviour by reducing the number of satellites and the power input needed for the actuation signal.

(a) $t = 140$ µs (b) $t = 168$ µs
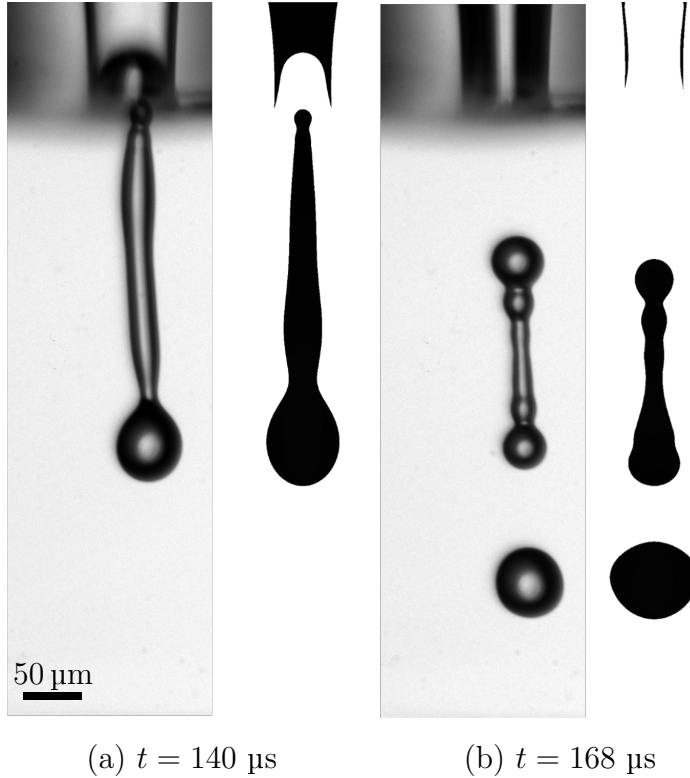
Figure 5.4: Comparison between simulations (white background) and experiments (grey background) with water-Triton X-100 mixture at 1 CMC at different times for a prescribed drop speed of $4\,\mathrm{m\,s^{-1}}$ (a) at pinch-off from the nozzle $t = 140$ µs and (b) at break-off of the main droplet from the ligament at $t = 168$ µs.

Our pure solution here is water. Water has a high surface tension of $0.072\,\mathrm{N\,m^{-1}}$ and a low viscosity of $0.001\,\mathrm{N\,s\,m^{-2}}$. The addition of most common surfactants, like Surfynol 465, Triton X-100 and Dynol reduces the surface tension down to $0.035\,\mathrm{N\,m^{-1}}$ in equilibrium (Robinson et al., 2014; Yang and Bain, 2009) and for concentrations lower than the CMC, the viscosity remains unaffected.

The drive amplitude is kept the same for both pure solvent and surfactant solutions, in both experiments and numerical simulations. We firstly look at the transport of surfactants along the interface for different surfactant strengths β at a given initial concentration. The effects of surfactant strength β at a given initial concentration $K = 1$, a fully covered meniscus interface, are investigated by measuring different jetting properties such as the drop speed, the pinch-off time, as well as of course the jetting behaviour.

The surfactant strength parameter β is related to the surface tension γ reduction with surfactant concentration C as given by the Langmuir-Frumkin surface

equation of state (4.4) which we state here in the dimensionless form

$$\gamma = 1 + \beta \ln(1 - KC), \tag{5.3}$$

where K is the ratio of the equilibrium surfactant concentration on the solvent studied and the maximum packing concentration,

$$K = \frac{\Gamma_{\text{eq}}}{\Gamma_{\infty}}$$

and

$$\beta = \frac{\Gamma_{\infty} \mathcal{R} T}{\gamma_p}.$$

Equation (5.3) holds for low values of C. However there is a lower bound to the surface tension as maximum packing is approached. Therefore in the simulation we set

$$\gamma = \max \left(1 + \beta \ln(1 - KC), \gamma_{\text{eq}} \right),$$

where γ_{eq} is the ratio of the surface tension at CMC to the surface tension of pure water, as explained in §4.6.2. This is shown in figure 5.5, where we see that the minimum surface tension of $0.035 \, \text{N m}^{-1}$ is reached at lower concentrations for higher β. Here $\gamma_{\text{eq}} = 0.5$, leading to a dimensional surface tension of $0.035 \, \text{N m}^{-1}$.
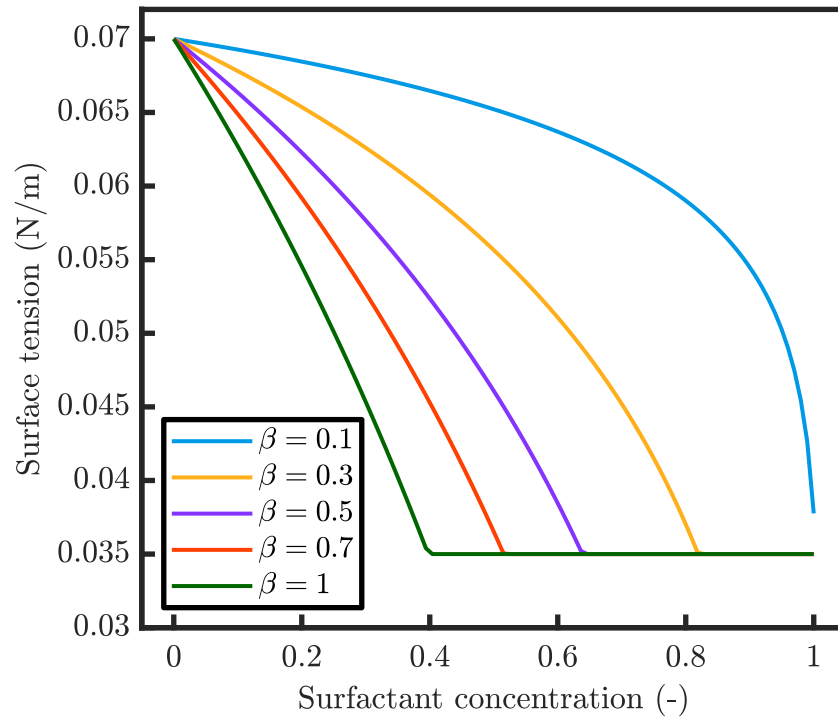
Figure 5.5: Surface tension as a function of surfactant concentration using equation (5.3) for different surfactant strengths β. A minimum surface tension equal to the equilibrium surface tension is imposed at the value of $0.035 \, \text{N m}^{-1}$.

Without surfactant exchange, surface advection and diffusion are the only mechanism to relax gradients in $\gamma(\Gamma)$. Surface diffusion acts against gradients in surface concentration Γ established by surfactant advection. In our simulations, the diffusion is weak, as seen in §5.1.2 so that the main mechanism is advection and its modification from Marangoni stresses. The surface tension $\gamma(\Gamma)$ will also determine the strength of the Marangoni reverse flows, which also act to oppose the gradients in concentration.

As the newly formed droplet is pushed out of the nozzle, surfactants are concentrated at the tip of the drop, (figure 5.6a). This is a consequence of the pull-push drive. During the first pull stage, new surface is generated by the retraction of the meniscus into the nozzle lowering the concentration. However, during the subsequent push-out stage, the meniscus initially contracts before expanding again as the fluid is squeezed at the nozzle, which has the effect of transporting the surfactants towards the front of the droplet. As the new surface is created at a rate several orders of magnitude faster than the surfactants can diffuse (based only on surface diffusion, with the timescale (5.2)), diffusion has a negligible effect on the surfactant transport. Therefore, the dominant mechanism controlling the surfactant distribution is the advection by the surface velocity, which is modified by the Marangoni forces.

The ensuing surface tension gradients act in a manner such as to restore the interface to its homogeneous equilibrium state by producing flow in proximity to the interface, a phenomenon known as the Marangoni effect (Marangoni, 1871). In other words, the surfactants will locally decrease the surface tension and as a result, drive fluid flow away from that region.

At a later time, when the droplet and its ligament pinch off from the nozzle, the surfactants have moved closer to the neck (figure 5.6b). This arises from a flow around the droplet surface from the front towards the tail. This also occurs for surfactant-free fluids but is enchanced by Marangoni forces. The high concentration of surfactants earlier at the front created a high surface tension gradient and therefore a strong Marangoni force and a large Marangoni stress,

$$T_M = \mathbf{t} \cdot \nabla_s \gamma \,, \tag{5.4}$$

where $\mathbf{t}$ is the unit tangent to the free surface (directed toward the main droplet) and ∇_s is the surface gradient operator. A negative spike in T_M represents a Marangoni stress pointing away from the bulge toward the main ligament. In addition, the surface regions with high surfactant concentration and therefore lower surface tension,
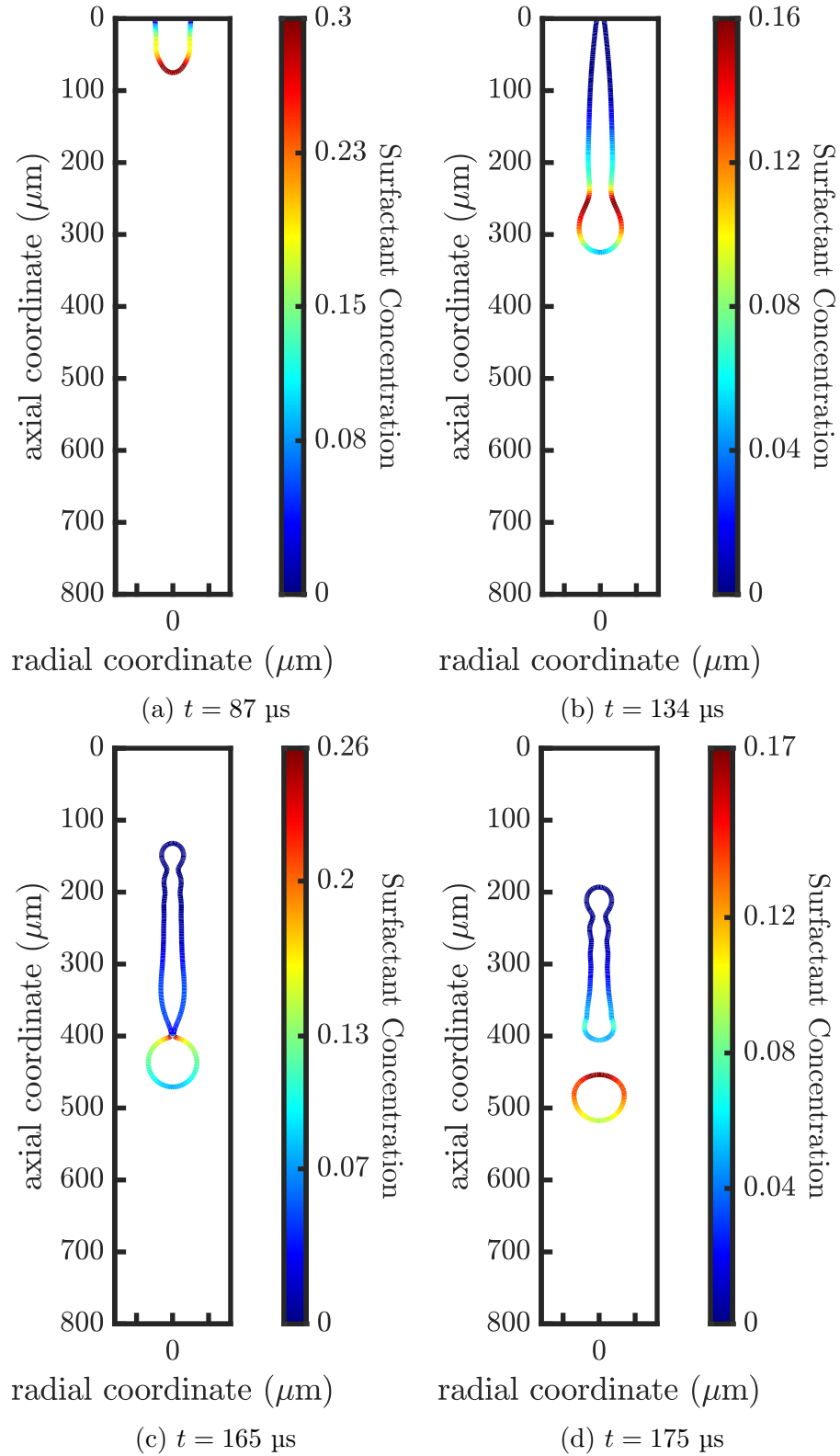
Figure 5.6: Surfactant distribution along the interface at different stages of the jetting process for $\beta = 1$. From top left to bottom right: (a) end of push-stage, (b) pinch-off from the nozzle, (c) capillary break-off and (d) ligament retraction. Note here that the colour bar limits are different for each case. The concentration shown here is non-dimensionalised by equilibrium concentration.

stretch which then lowers the concentration. This shows again that advection and Marangoni forces are the driving mechanisms for surfactant transport on the inkjet timescales of microseconds. As seen in other studies in surfactant covered filaments (Kamat et al., 2018; Xu et al., 2007; Ambravaneswaran and Basaran, 1999; Timmermans and Lister, 2002; Craster et al., 2002) as the thread thins, the break-off vicinity is almost surfactant-free with the pure liquid surface tension, which shows that surfactants play no role in the local pinch-off dynamics. However, we note here that these works assume a uniform surfactant covered filament and the timescales are significantly larger.

After the capillary break-off figure 5.6d, when the droplet has separated from the ligament, the surfactant concentration on the surface of the droplet approaches a uniform concentration, subject to change with the small amplitude oscillations of the droplet. The ligament has a much lower surfactant concentration than the drop and that as well will eventually relax to a uniform concentration.

To show the importance of the surface tension gradient and therefore the Marangoni stress, we compare a weaker surfactant of strength $\beta = 0.1$ with the strong surfactant presented and discussed on figure 5.6 of strength $\beta = 1$. The strength of the surfactant dictates the reduction of the surface tension based on the surfactant concentration locally from the isotherm 5.3 and therefore the strength of the Marangoni force.

In both cases, during the push-out stage, the head front has a high concentration of surfactants with a more uniform distribution in the $\beta = 1$ case, where the head has a concentration of 0.3 and the vicinity around it has a concentration closer to 0.2 (figure 5.7a, right). At the time when the ejected fluid pinches off from the nozzle, figure 5.7b, there is a clear difference between the cases of strong and weak surfactant: $\beta = 0.1$ has a localised area of high concentration towards the rear of the drop, while $\beta = 1$ has a lower and more uniform concentration along the head. This difference is caused by the stronger Marangoni force for $\beta = 1$ that acts to oppose gradients in surfactant concentration. However in both cases the trailing ligament is almost entirely surfactant-free.

A similar variation in the distribution can be seen at the time of the capillary break-off in figure 5.8, where for the weak surfactant ($\beta = 0.1$) case there is a localised area of high surfactant concentration, towards the back of the main drop. This results from the advection of surfactant from the front of the main drop by circulatory flow around the surface of the drop. In comparison, in the case of the stronger surfactant the concentration is less localised and the maximum located

(a) $t = 87$ μs

(b) $t = 134$ μs

Figure 5.7: Surfactant distribution along the interface at different stages of the jetting process for $\beta = 0.1$ on the left and $\beta = 1$ on the right of each subfigure. From left to right: (a) end of push-stage and (b) pinch-off from the nozzle. Here the colour bar limits are the same for both cases. The concentration shown here is non-dimensionalised by the equilibrium concentration.

closer to the rear of the droplet. This can also be seen in the top sub-figures within figures 5.10 and 5.11 that show the surfactant concentration along the interface at a time just before the capillary break-off.

After the capillary break-off, when the head droplet has separated from the ligament, the surfactant concentration of the droplet approaches a uniform surfactant concentration, driven by the Marangoni stress and subject to change with the small amplitude oscillations of the droplet, (figure 5.8b). Both cases have an almost surfactant-free ligament, since the induced Marangoni forces are not strong enough to redistribute surfactants far from the initial high concentration at the head. In addition, both surfactant solutions will reach an equilibrium uniform concentration at a later time after the capillary break-off.

Figure 5.8: Surfactant distribution along the interface at different stages of the jetting process for $\beta = 0.1$ on the left and $\beta = 1$ on the right of each subfigure. From left to right: (a) capillary break-off and (b) ligament retraction. Here the colour bar limits are the same for both cases. The concentration shown here is non-dimensionalised by the equilibrium concentration.

5.4 Marangoni Stress on the Interface

In figures 5.6 to 5.8, the non-uniform distribution of surfactants along the jet is shown. As the neck thins, the advection of surfactant from the thread to the main droplet results in depletion of surfactant in the thread and accumulation of surfactant in the main droplet and closer to the neck from the main droplet side. Therefore, the surface tension is lower in the main droplet compared to the relatively surfactant-free thread.

At the pinch-off of the jet from the nozzle, the surfactant concentration is very low and uniform near the pinch-off point so that the surface tension is close to that of the pure solution shown in figure 5.9. Therefore, there is no effect of the Marangoni phenomenon and this can be also seen in the results for pinch-off time (figure 5.14) and pinch-off radius thinning rate (figure 5.19), which remain

unchanged irrespective of the presence of surfactants.
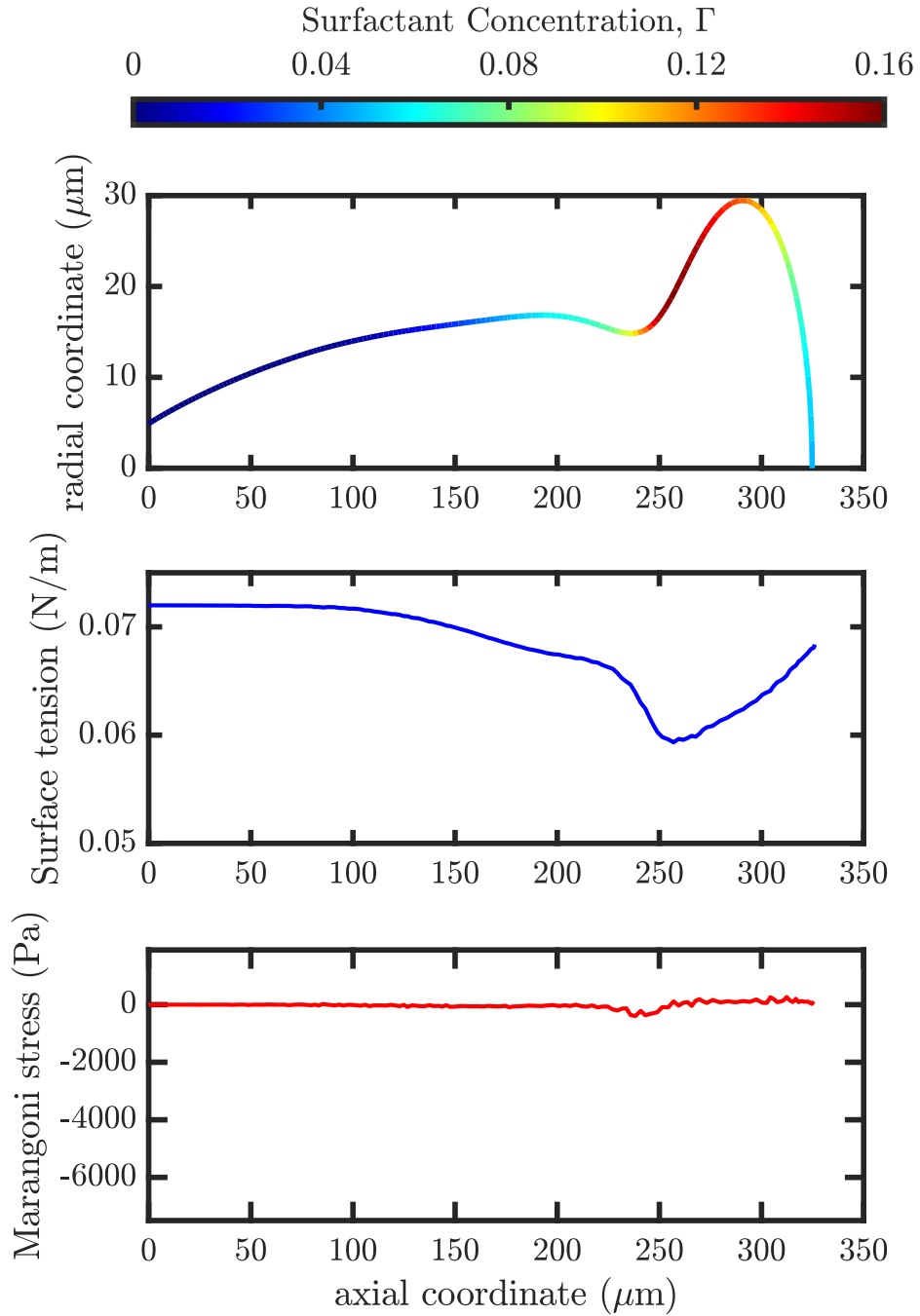
Figure 5.9: Surfactant concentration with interface shape, surface tension and Marangoni stress along the free surface for $\beta = 1$ at $t = 134$ µs, before break-off. The horizontal axis is common for every figure.

Figures 5.10 and 5.11 show the interface shape, the surfactant concentration, the surface tension and the Marangoni stress profiles just before the main droplet breaks off from the ligament for a weak ($\beta = 0.1$) and a strong surfactant ($\beta = 1$) case. The resulting surface tension gradient near the neck gives rise to a large Marangoni stress (5.4), just downstream of the neck. Close to the neck,

near the break-off point, there is a negative spike in T_M, which shows that there is a Marangoni stress pointing away from the main droplet toward the ligament. However, because of the difference in the surfactant strength, the surface tension reduction in the high concentration regions is smaller in the weak surfactant case (figure 5.10) compared to the stronger surfactant (figure 5.11).
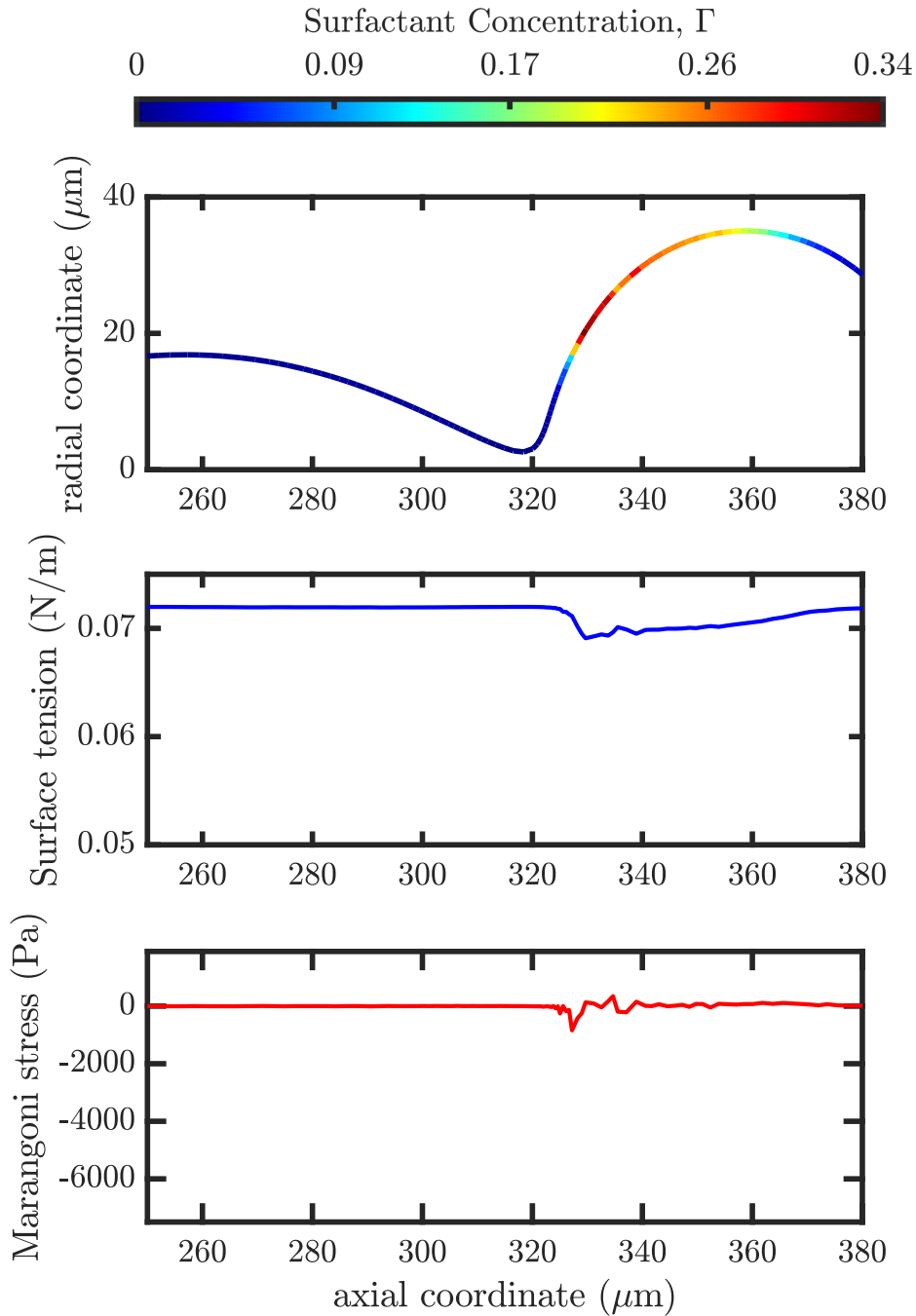
Figure 5.10: Surfactant concentration with interface shape, surface tension and Marangoni stress along the free surface for $\beta = 0.1$ at $t = 155$ µs, before break-off. The horizontal axis is common for every figure.
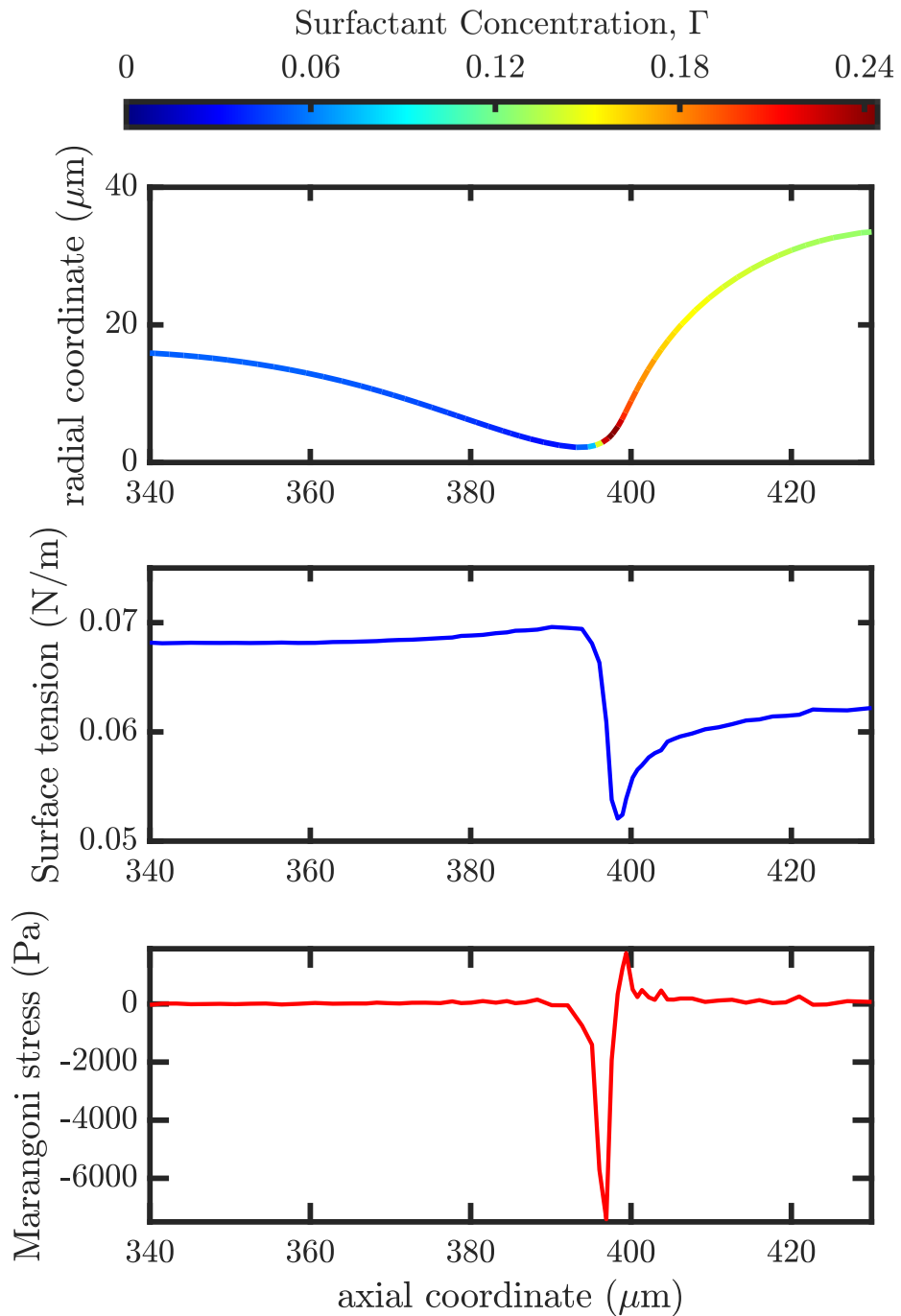
Figure 5.11: Surfactant concentration with interface shape, surface tension and Marangoni stress along the free surface for $\beta = 1$ at $t = 165$ µs, before break-off. The horizontal axis is common for every figure.

The strong Marangoni forces due the large surfactant concentration gradients and therefore high surface tension gradients, give rise to particular flow patterns inside the droplet. In figure 5.12, the flow relative to the mean velocity inside droplets of different surfactant strengths is shown at the time before the capillary break-off. In the pure water case, the flow shows a recirculation within the droplet with a return flow along the surface toward the neck. When surfactants are present,
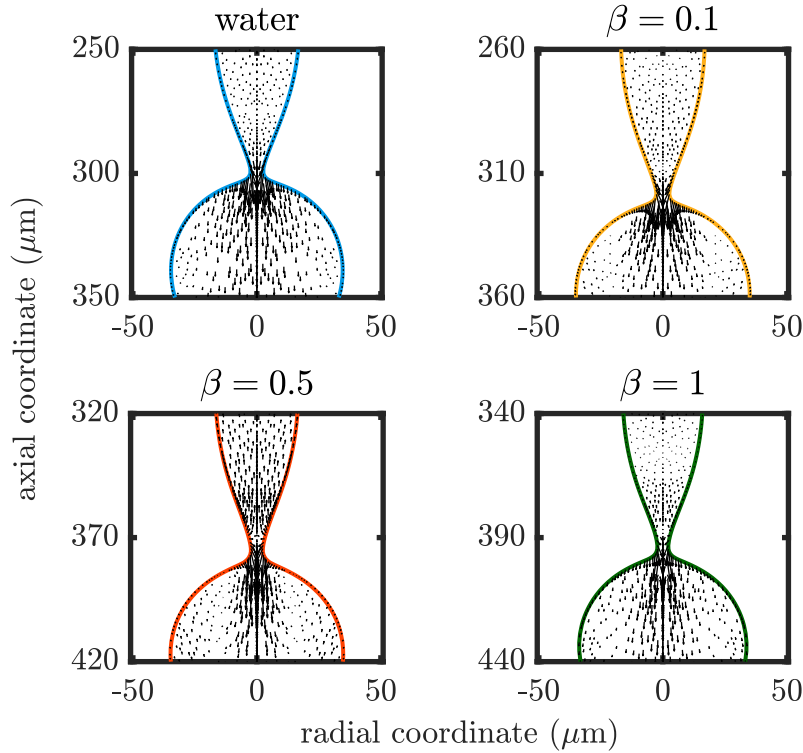
Figure 5.12: Flow relative to the mean velocity inside the droplet normalised by the head drop speed for pure water and for water with different surfactant strengths. The times for each of these graphs is different and is chosen as the point just before the capillary break-off.

even the weakest of them, the flow around the neck starts to differ: there is less re-circulation on the sides and a stronger jet appears downstream in the main droplet.

5.5   Jetting Behaviour

We now turn our focus to the jetting behaviour of the surfactant solutions. The effects of surfactant strength β for a given initial concentration $K = 1$, corresponding to a fully covered meniscus interface with $\gamma_{\mathrm{eq}} = 0.035\,\mathrm{N\,m^{-1}}$, are investigated by measuring different jetting properties such as the drop speed and the times of the pinch-off from the nozzle and the break-off of the main droplet from the ligament in the case of satellite formation. A study of the thinning rate of the neck of the surfactant solution jet is presented, where we investigate further the scaling laws for Newtonian fluids from Day et al. (1998).

5.5.1   Drop speed, pinch-off time and ligament length

The drop speed for different β is measured at two different times:

- at the pinch-off from the nozzle, i.e. when the tail pinches off from the nozzle;

- at the capillary break-off, i.e. when the main droplet separates from the ligament.

A small increase in speed of 10%, evident in figure 5.13, is noticed in the stronger surfactants, which is however relatively small. The pinch-off time is not affected by the presence of the surfactants, with no change in the pinch-off time at all as seen in figure 5.14. Since the drop speed and the pinch-off time are barely affected by the surfactants, there is no change to the ligament length.
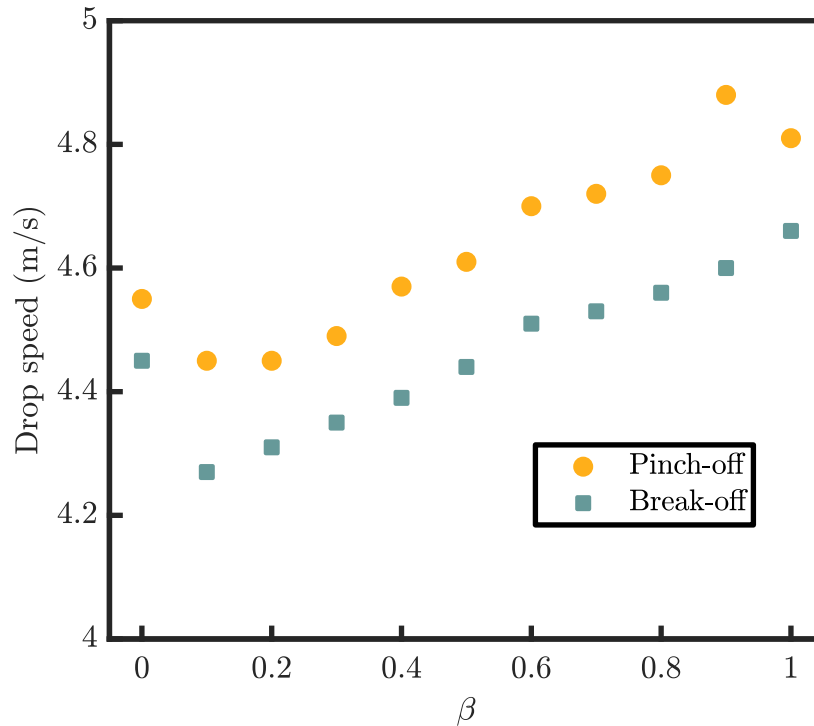
Figure 5.13: Drop speed at pinch-off from the nozzle and at break-off of the main droplet from the ligament for different surfactant strengths β, for same initial driving waveform. There is a small increase (maximum 10%) in the drop speed between the pure solution and the strongest surfactant.

Experiments in Ricoh and POF have confirmed this. In Ricoh, we used a glycerol-water mixture with viscosity of $0.01\,\mathrm{N\,s\,m^{-2}}$ and surface tension $0.065\,\mathrm{N\,m^{-1}}$ with Surfynol 465 and in POF, we used water with Triton X-100. Although the jetting properties are unchanged, it is worth mentioning that the surfactant solutions did show a more "user friendly" behaviour compared to the pure solutions. For
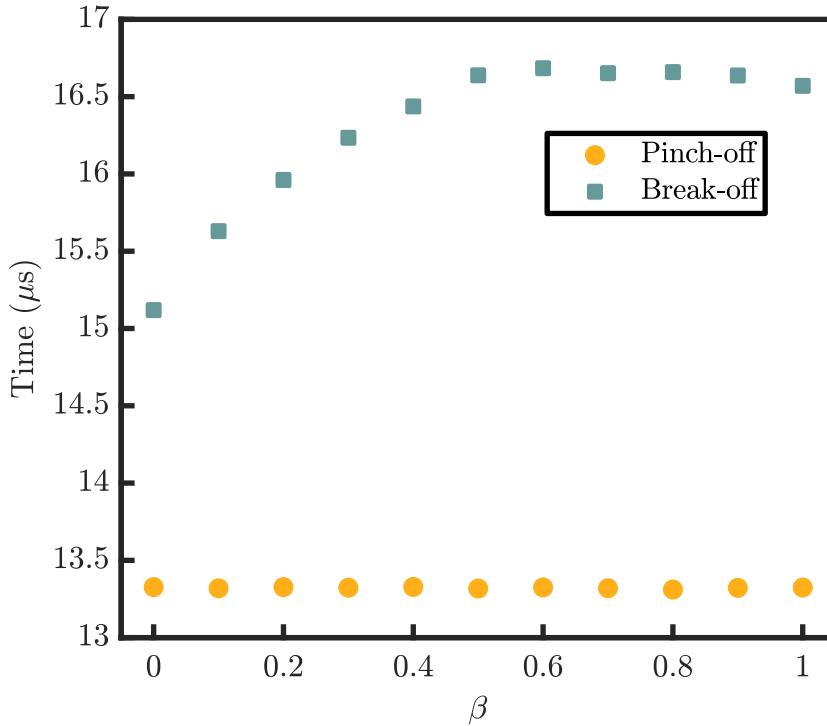
Figure 5.14: Pinch-off from the nozzle and capillary break-off times for different surfactant strengths β, for same initial driving waveform. The pinch-off time is clearly not affected by the presence of surfactants. On the other hand, the break-off time increases with surfactant strength until a critical value of $\beta = 0.6$.

example, with the glycerol-water mixture, we experienced clogging issues, where a layer of fluid formed on the nozzle plate so that fluid was unable to be jetted and a flushing procedure was required to restore the nozzles. However, when we used the surfactant solutions, the jetting was stable and reproducible during the whole duration of the experiments. This can be explained by the results shown in figure 5.7. At the beginning of the jetting process, the meniscus is fully covered with surfactants which reduces the surface tension to its equilibrium value. At the early stages of the drop formation, the surfactants remain at the head of the droplet, keeping the surface tension close to the equilibrium value. Therefore, the ejection process is applied essentially to a fluid with less surface tension which makes it easier to jet. This suggests that surfactants, even these very weak ones we tried experimentally, can be helpful in improving jetting reliability.

5.5.2 Capillary break-off

Even though the surfactants show no effect on most stages of the jetting process, there is an effect on the capillary break-off time.

Unlike pinch-off time, the capillary break-off time as shown in figure 5.14 increases with surfactant strength, delaying the capillary break-off event. However this increase saturates above a critical value of $\beta = 0.6$, beyond this the strength of the surfactant does not affect the break-off time. This saturation effect can be explained by the reduction of the surface tension from equation (5.3): the equilibrium surface tension is reached at high surfactant concentration regions and when the surfactant strength is high, this value is reached faster. Therefore at high values of β, the same surfactant concentration would give a surface tension value very close to the equilibrium as seen in figure 5.5.
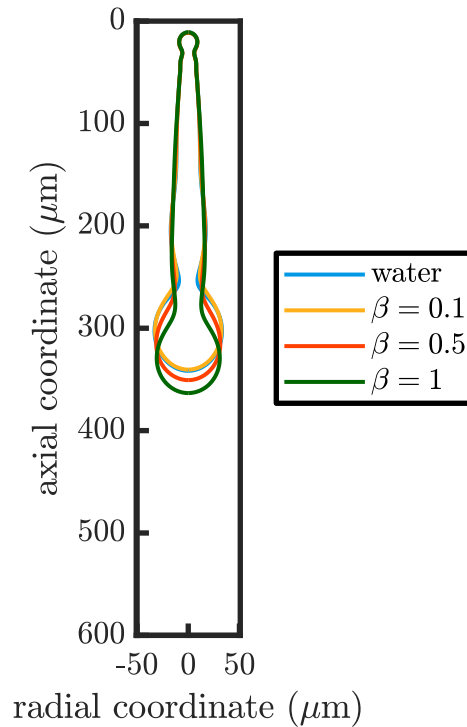
Figure 5.15: Surface shape at $t = 142\,\mu s$ for different surfactant strengths after pinch-off from the nozzle. At this early stage, the influence of surfactants is negligible, with no significant change on the free surface, neither velocity as mentioned earlier.

In figure 5.15, the free-surface shape of water and different surfactant solutions are shown. As mentioned in §5.5.1, at the early stages of the jet, there is no difference between the pure and the surfactant solutions. Comparing with figure 5.7, we can see that the surfactants stay at the head of the droplet and therefore we expect no influence at this stage.

During the later stages of the jetting and particularly closer to the capillary break-off time, shown in figure 5.8, the surfactants are advected towards the rear of the main drop, therefore we expect a difference in the behaviour closer to the neck. Indeed, while the main drop in solutions with the weaker surfactant has already broken off, in the stronger cases the ligament remains attached and it breaks off later,
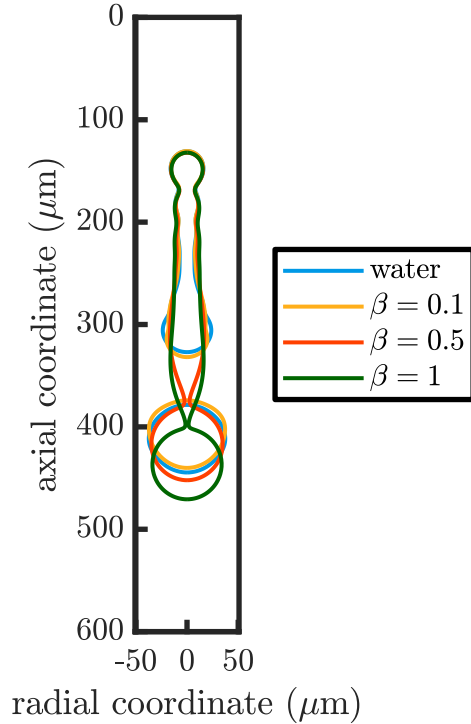
Figure 5.16: Surface shape at $t = 165\,\mu$s for different surfactant strengths. In the pure solution and weak surfactant solution ($\beta = 0.1$) the main droplet has already broken off from the ligament, while at $\beta = 0.5$ it remains attached. A slight increase in the drop velocity is noticed in the very strong surfactant $\beta = 1$.

as seen in figure 5.16. This can also be explained by the difference in the resulting Marangoni stress which is smaller in the weak surfactant as seen in figures 5.10 and 5.11.

This suggests that, with appropriate waveform optimisation for the initial driving signal, it may be possible to prevent satellite formation by adding a strong surfactant. Taking that one step further, figure 5.17 shows a case where the addition of a strong surfactant ($\beta = 1$) prevents completely any satellite formation. The pure solvent here has a viscosity of $0.07\,\mathrm{N\,s\,m^{-2}}$, surface tension $0.072\,\mathrm{N\,m^{-1}}$ and the drop speed is $3\,\mathrm{m\,s^{-1}}$.

5.5.3 Jet break-up thinning rate

Surfactant strength is the key property that affects the break-off of the jet, as seen in figure 5.14. Break-off is important both during the ejection and during the possible subsequent break-up of satellite drops from the ligament. The inviscid assumption is appropriate while the pinch-off region is larger than $1\,\mu$m. Therefore we will use the scaling laws presented by Day et al. (1998). We note that as τ is the time until
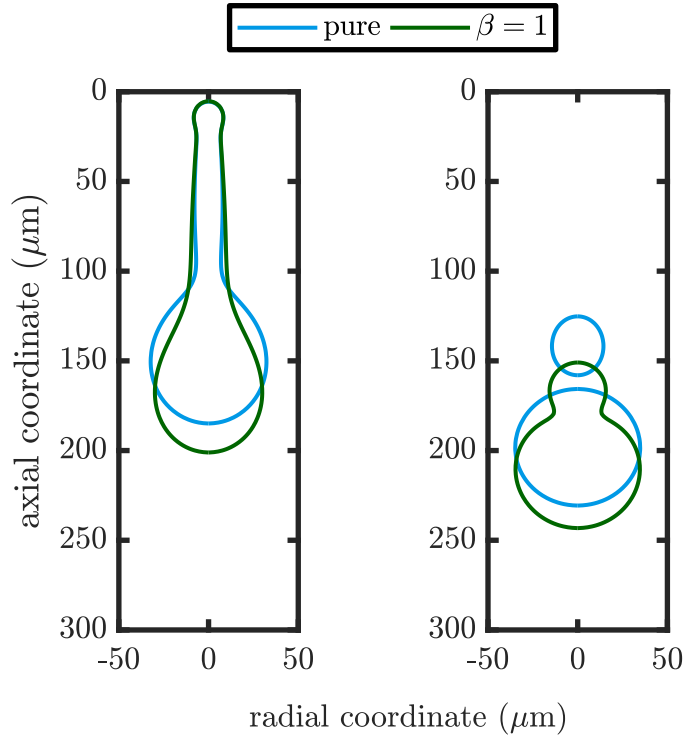
Figure 5.17: Surface shape at $t = 150\,\mu s$ and $t = 180\,\mu s$ for fluid with viscosity of $0.007\,\mathrm{N\,s\,m^{-2}}$, surface tension $0.072\,\mathrm{N\,m^{-1}}$ and final drop speed of $3\,\mathrm{m\,s^{-1}}$. While in the pure solution there is a satellite, the presence of a strong surfactant $\beta = 1$ prevents that formation with a single droplet as a result.

the break-off of the jet, $\tau = t_b - t$ or $\tau = t_p - t$ for capillary break-off time or pinch-off time respectively.

In §1.2.3, we described the framework of Newtonian jet break-up. For the system we are looking at, with Microdrop nozzle and water properties for the fluid, the Ohnesorge number is very low, Oh $= \mathcal{O}(10^{-3})$ and therefore we expect to be in the Euler regime (Day et al., 1998) for capillary thinning.

Once the neck radius becomes small compared to the drop radius, the behaviour at the vicinity of the neck is locally determined and independent of initial conditions. Therefore we expect that in the capillary break-off region, both axial and radial dimensions, the neck radius scales as

$$\left(\frac{\gamma \tau^2}{\rho}\right)^{1/3}. \tag{5.5}$$

This behaviour can be investigated by plotting the numerical predictions for the minimum neck radius $R^{3/2}$ against the time until the pinch-off or break-off event τ, where we have

$$R^{3/2} = 0.586 \left(\frac{\gamma}{\rho}\right)^{1/2} \tau. \tag{5.6}$$

This scaling indicates that the thinning rate should increase with the surface tension as $\gamma^{1/2}$.

Firstly, we investigate the predicted radius thinning for the simple Newtonian fluids for our system. The thinning rate for different surface tension is computed by linear fit of the last stage of thinning, when the radius decreases linearly. Then, a power law of the form $y = \gamma^{\alpha}$ is fitted to the data for each surface tension case and our predicted α is 0.56, as shown in figure 5.18. For the Euler regime, $\alpha = 0.5$ so this gives confidence that the mathematical framework established and explained in chapter 3 captures the jet break-up dynamics successfully and accurately.
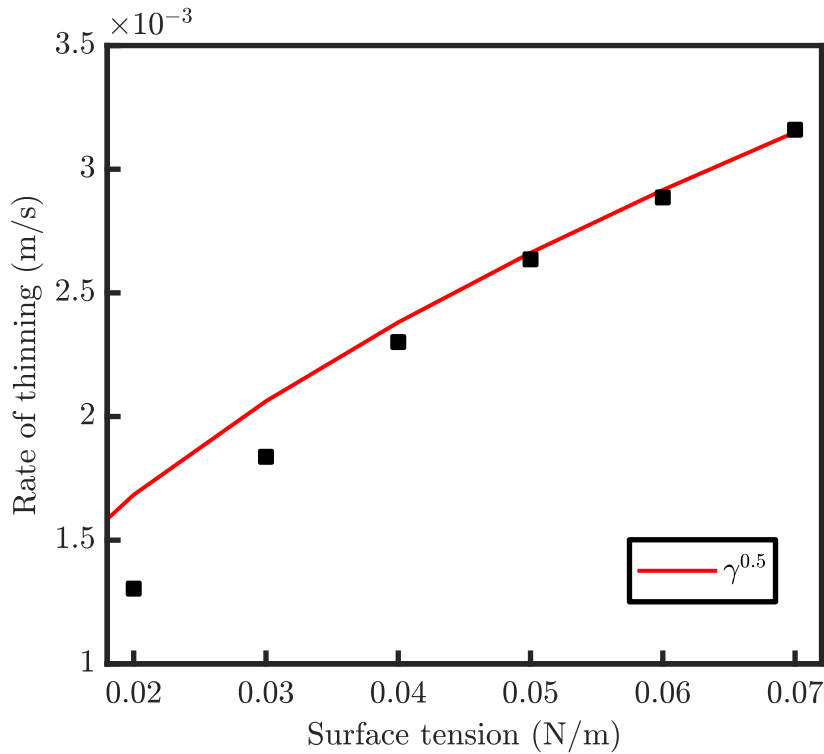
Figure 5.18: Rate of thinning of the neck for Newtonian fluids with different surface tensions. The solid line shows the $\gamma^{0.5}$ (Day et al., 1998) scaling law (5.6).

As shown in figure 5.14, the pinch-off time is not affected by the surfactants. Hence, the pinch-off neck thinning rate is not expected to change with the increasing surfactant strength, which we can see in figure 5.19. However, it is important to note here that the predicted thinning rate follows the scaling rate 5.5, as $R^{3/2}$ is a linear function of time τ_p.
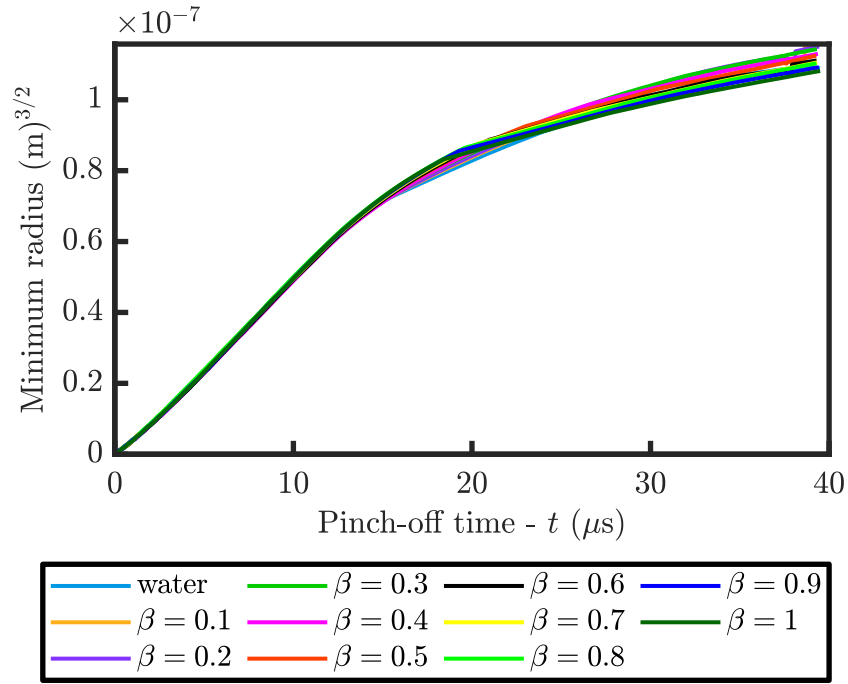
Figure 5.19: Jet radius near pinch-off for different surfactant strengths. The jet radius R scales with $\tau^{2/3}$ where $\tau = t_p - t$ and t_p is the pinch-off time, as demonstrated by plotting $R^{3/2}$ against τ. The surfactant strength β does not affect the approach to pinch-off.
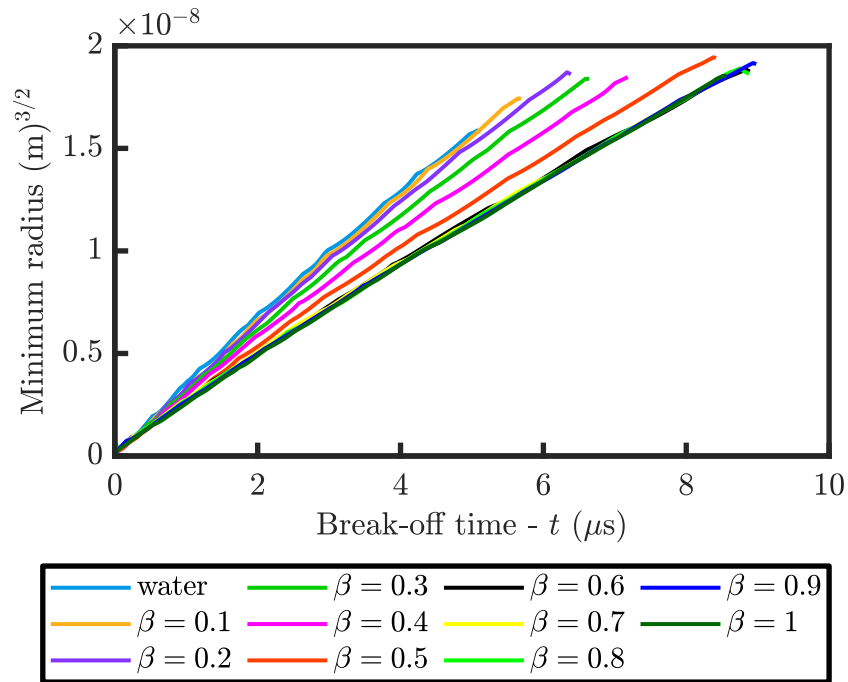
Figure 5.20: Neck radius for different surfactant strengths. The neck radius R scales with $\tau^{2/3}$ where $\tau = t_b - t$ and t_b is the capillary break-off time, as demonstrated by plotting $R^{3/2}$ against τ. The surfactant strength β affects the slope of R indicating that a stronger surfactant can delay the capillary break-off. After $\beta = 0.6$, the minimum radius for each case overlaps indicating an independence of surfactant strength after that value.

Beside the confirmation of the scaling law, figure 5.20 shows that the rate of thinning decreases with increasing surfactant strength. This is shown both by the decreasing slope of the minimum radius and the later break-off time. However, for the given system at $\beta = 0.6$ the thinning of the neck becomes independent of the surfactant strength, which is explained in §5.5.2.
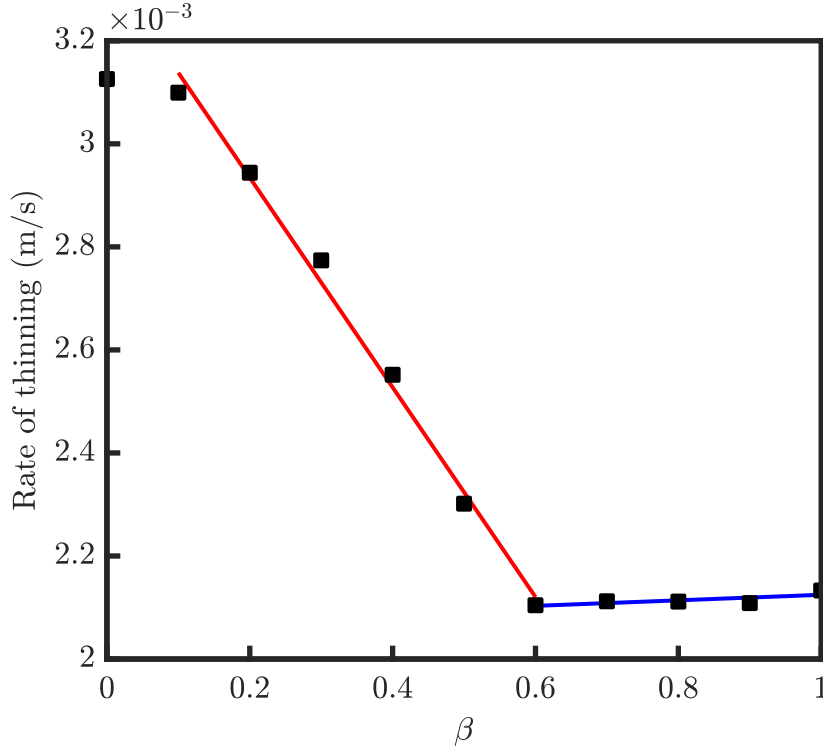
Figure 5.21: Thinning of the neck radius for different surfactant strengths. These are computed by the linear fit in the results shown in figure 5.20. Two distinct regimes are shown: before $\beta = 0.6$ where the thinning rate decays linearly with β and after $\beta = 0.6$ where the thinning rate is almost independent of β.

As shown in figure 5.21, the neck radius decays more slowly for stronger surfactants. This is another confirmation for the effect the surfactants can have on the jetting behaviour: by using a strong surfactant and an appropriate driving signal, we can delay the break-off as required so as to provide time for the tail to be absorbed into the main droplet.

5.6   The Effect of Surfactants Using an Industrial Printer

We now revisit the Oh -Re phase diagram for the jetting behaviour we presented in chapter 3 in figure 3.15. We explore the effect of surfactants on the regime of

behaviour previously observed. For the simulations, the Ricoh nozzle geometry is used and a prescribed drop speed of $7\,\mathrm{m\,s^{-1}}$, with the same initial driving waveform as described in §3.3. We will investigate the jetting behaviour of the fluid with viscosity $0.01\,\mathrm{N\,s\,m^{-2}}$ and surface tension $0.07\,\mathrm{N\,m^{-1}}$, which corresponds to Re = 9 and Oh = 0.35 to which we add a strong surfactant ($\beta = 1$) to lower the equilibrium surface tension to $0.035\,\mathrm{N\,m^{-1}}$.
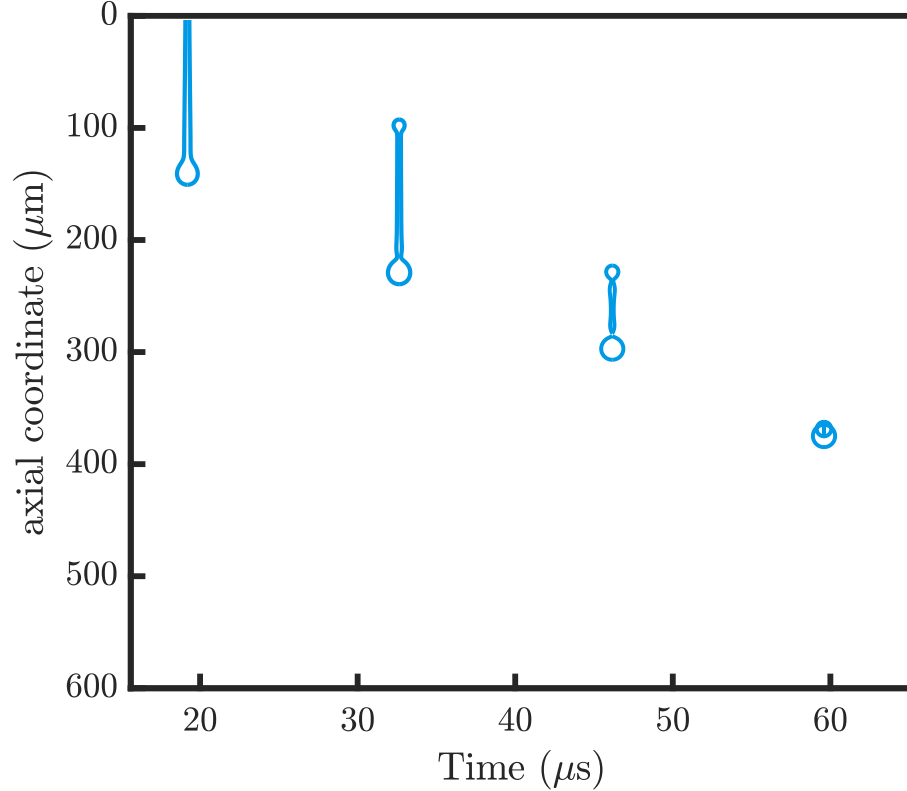
Figure 5.22: Snapshots showing the shape of the fluid interface simulated using Ricoh nozzle and driving waveform. Here, the pure solution without surfactant has a viscosity $0.01\,\mathrm{N\,s\,m^{-2}}$ and surface tension $0.07\,\mathrm{N\,m^{-1}}$.

Figure 5.22 shows the jetting of the pure fluid. The jet breaks up to form a main drop with a single satellite that catches up with the main drop.

We now compare a pure fluid solution with viscosity $0.01\,\mathrm{N\,s\,m^{-2}}$ and surface tension $0.035\,\mathrm{N\,m^{-1}}$, chosen to be the same as the equilibrium surface tension in the surfactant solution using the same initial waveform as in the previous case. The lower surface tension results in an increase in the drop speed by 40% so that the flow parameters are now Re = 11 and Oh = 0.5 for this case, see figure 5.23. From our phase diagram 3.15, the predicted jetting behaviour for that fluid is to form a very long ligament that will eventually break up into a large number of satellites.

Figure 5.24 shows the behaviour of the surfactant solution. Using the same waveform, the drop speed is 10% higher than for the pure solution. This is due to
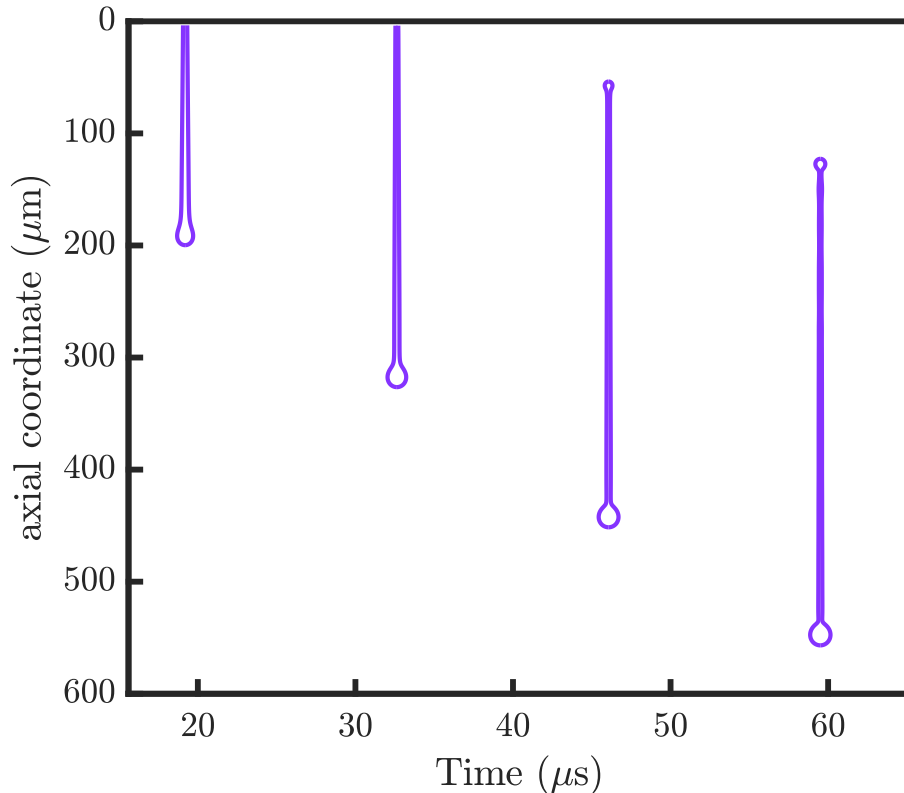
Figure 5.23: Snapshots showing the shape of the fluid interface simulated using Ricoh nozzle and driving waveform. Here, the fluid has constant surface tension equal to the equilibrium surface tension of the surfactant solution $0.035\,\text{N}\,\text{m}^{-1}$.

the initial reduction in the surface tension compared to the pure fluid and results in slightly longer ligament than in case (5.22), although much shorter than found with a fluid of the same equilibrium surface tension. This long ligament breaks up into three satellites rather than the single satellite for the pure case (5.22). Moreover the two slower satellite do not merge with the main drop.

What is clear from this comparison is that adding surfactants to an ink does not result in reproducing the same behaviour as a simple pure fluid with a lower surface tension. In this example, the addition of surfactants did not improve the jetting behaviour for this waveform although it did produce a slightly higher drop speed. However, the break-up behaviour is much closer to that of the higher surface tension fluid than of the lower one. Since in practice high surface tension fluids are difficult to jet, adding surfactants to make jetting more reliable and reproducible by reducing initial surface tension around the meniscus allowing easier ejection but giving a higher effective surface tension during subsequent break-up, may improve the overall jetabillity.
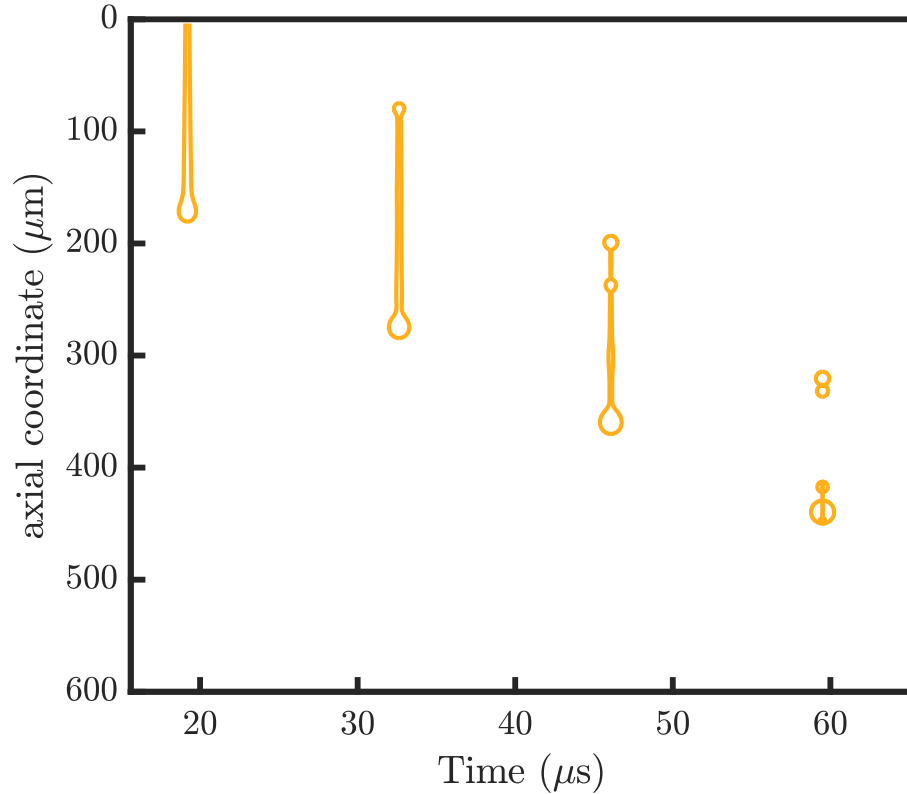
Figure 5.24: Snapshots showing the shape of the fluid interface simulated using Ricoh nozzle and driving waveform. Here, a surfactant solution with $\beta = 1$ where the surfactant lowers the equilibrium surface tension from $0.07\,\mathrm{N\,m^{-1}}$ to $0.035\,\mathrm{N\,m^{-1}}$.

5.7 Conclusions

In this chapter, an analysis of the jet break-up in the presence of surfactants has been presented. The diffusion timescale is much smaller than the break-off time and the new surface generation, therefore we conclude that diffusion is not important in inkjet drop formation. This can also be seen by the large surface Péclet number in our system of order 10^5.

Consequently, surfactants are unevenly distributed with a higher concentration on the surface of the drop compared to the ligament. This gives rise to two very important consequences and benefits from the surfactant presence:

1. The strong Marangoni stress around the vicinity of the neck, where the side close to the ligament is surfactant-free and the side of the droplet head is covered with surfactants, delays the break-off time significantly and in some circumstances it has been shown that this can prevent the formation of any satellites.

2. In a typical example of an industrial print-head with a high drop speed, the

addition of surfactants did not reduce the number of satellites observed in this case, however it delays the break-off time. This allows fluids that are difficult to jet as pure solutions, due to problems near the nozzle area (clogging, surface overlapping), to be jetted more reliably without losing any of the properties of the pure solution.

For the latter, we expect that an extended waveform optimisation can result in single droplet behaviour just through the addition of surfactants, at a concentration lower than CMC.

From a fluid dynamics perspective, the most interesting dynamical effects are in the area near the neck between the drop and the ligament. The distribution along the jet is not uniform (figures 5.7 and 5.8) and these surface concentration gradients give rise to Marangoni stresses. The Marangoni stress is strong near the neck and it counteracts the surface stretching caused by capillary thinning. As a result, the thinning rate of the neck radius slows down significantly with the surfactant strength (figures 5.20 and 5.21). The thinning rate for this system follows the prediction of Day et al. (1998), as the radius decreases with time as $t^{3/2}$. This shows that the surfactants do not affect the Newtonian properties of the fluid such as viscosity, however by altering the surface tension (locally), they change the dynamics of the jet break-up.

Chapter 6

Oscillating Drop Method and Dynamic Surface Tension

In this chapter we look at the oscillating drop method, a technique used to measure surface tension and viscosity of fluids. We first give the background of the method and the mathematical framework which we will use for our analysis. The dependence of the frequency and the decay rate of the oscillation on the surfactant strength is investigated. Finally, we look at the flow inside a droplet at various stages of the oscillating cycle and compare them to the results we obtained from the mathematical analysis of the oscillating droplet, explaining our observations.

6.1   Background

For fluids where the surface tension varies in time, a key challenge is to be able to measure surface tension on a sufficiently short timescale to capture the dynamic surface tension. Techniques such as pendant drop and tensiometer methods are only able to capture dynamic surface tension for surface ages greater than around 10^{-2} s (Franses et al., 1996). However, with the advent of high-speed video, the oscillating drop method has been explored as a tool for the determination of the dynamic surface tension and viscosity of fluids. In principle, the oscillation of a free-falling printed drop immediately after formation at the orifice provides a way to measure dynamically the viscosity and the surface tension from the decay rates and frequencies of the resulting oscillation on timescales smaller than 10^{-4} s, much faster than other techniques (Ronay, 1978; Trinh and Wang, 1982; Loshak and Byers, 1973; Miller et al., 1994; Matsumoto et al., 2002). As such, drop oscillation

based measurement has applications in sprays, inkjet printing, nuclear physics and meteorology (Velentine et al., 1965; Nelson and Gokhale, 1972; Wong, 1976; Martin et al., 2008).

Trinh et al. (1988) and Hiller and Kowalewski (1989) considered experiments on freely oscillating drops with small oscillation amplitudes and validated the oscillating drop theory within the linear approximation for the fundamental mode. The oscillating drop method was used to determine the temporal development of the dynamic surface tension of heptanol-water solutions in the work of Stückrad et al. (1993) where they interpreted the results by a diffusion-controlled adsorption mechanism. The experimental and theoretical work of Becker et al. (1991) studied the non-linear dynamics of viscous droplets with large initial amplitudes of oscillation, exceeding 10% of the drop radius for the fundamental mode. Their results showed that non-linear effects were most apparent for higher oscillation modes ($l > 2$, where l is the oscillatory mode) while the fundamental mode followed the linear theory even for initial amplitudes exceeding 50% of the drop radius. These previous studies have investigated drop diameters of the order of $\sim 100\,\mu\text{m}$–$1\,\text{mm}$.

All of these classical oscillating drop studies examined Newtonian fluids. However, with the increasing use of inkjet printing in recent years, the dynamic properties of complex fluids, such as polymer solutions, colloids, emulsions, gels and foams and the addition of surfactants, have attracted great interest both for fundamental research and for industrial applications involving jet, sprays and coating. These include development of the theory of oscillating viscoelastic drops (Khismatullin and Nadim, 2001), experiments to measure polymer relaxation times in viscoelastic levitated drops (Brenn and Teichtmeister, 2013), experimental measurement of the transient shear viscosity of shear-thinning fluids on the timescale of a few tens of microseconds (for picolitre droplets) to a few tens of milliseconds (for microlitre drops) (Staat et al., 2017). Yang et al. (2014) and Hoath et al. (2015) used the oscillation of drops generated using a MicroFab nozzle to measure the surface tension and viscosity of complex fluids under conditions relevant to the DOD method. In particular, they were able to study the fluid thixotropy in response to shear-changing environments, found when drops are formed in a jet or a spray, where the fluid moves from the high-shear environment of a nozzle to the low-shear environment of a free drop over a period of microseconds to milliseconds (Ishiwata and Sakai, 2014).

In modern DOD inkjet printing, the jetted droplets are often a complex mixture of solvents, pigments and one or more surfactants (Wijshoff, 2010). The solvents carry the pigment particles to the medium and evaporate, solidify or crys-

tallise, while the surfactants prevent wetting of the nozzle plate and promote spreading of the droplet after it impacts the underlying medium. The determination of the droplet's in-flight dynamics is crucial to understanding droplet formation in these newly developed complex fluids. The surface tension of a surfactant solution is determined by the concentration of the adsorbed surfactant molecules at the liquid-air interface. Where fresh surface is formed, the surface tension is equal to the pure surface tension of the solvent in the absence of surfactants (Ohl et al., 2003) and it decreases as surfactants from the bulk adsorb at the interface, until reaching an equilibrium surfactant concentration. The timescale of the adsorption process is governed by the diffusion time of the surfactant molecules. This is the time that a surfactant molecule requires to diffuse from the adsorption or depletion depth h to the interface (Ferri and Stebe, 2000; Alvarez et al., 2010), where h is the equilibrium surface concentration of surfactant divided by the bulk concentration. The typical diffusion time τ_D is inversely proportional to the surfactant diffusion coefficient D as $\tau_D \sim h^2/D$ and ranges from milliseconds to days, depending on the surfactant type and surfactant concentration (Chang and Franses, 1995; Eastoe and Dalton, 2000). In inkjet printing, the surfactants need to act before the ink dries or even while the drop is formed and it is therefore required that they are adsorbed as fast as possible. As described in sections 1.2.1, 3.6 and 5.1.2, droplet formation is a fast process with timescales of the order of $10\,\mu s$, which is shorter than the approximately $100\,\mu s$ for which a droplet is typically in flight. This in turn is much shorter than the time a droplet needs to evaporate which is typically on the order of seconds. A surfactant with a typical adsorption timescale of the order of milliseconds is considered a fast-adsorbing surfactant (Chang and Franses, 1995; Eastoe and Dalton, 2000) and as a result the surface tension of a newly formed drop is higher during its formation and flight than during the later spreading and evaporation stages. Although methods exist to measure the time-dependent dynamic surface tension (Franses et al., 1996; Tian et al., 1995, 1997), it was not until recently that new methods using ultra-fast imaging have been developed in order to operate at the microsecond timescales and the micrometer lengthscales of the inkjet process (Yang et al., 2014; Hoath et al., 2015; Staat et al., 2017).

6.2   Mathematical Framework

For more than a century, the oscillatory motion of a drop has been a classical problem in fluid mechanics (Rayleigh, 1879; Lamb, 1932; Chandrasekhar, 1959; Prosperetti, 1980; Becker et al., 1994; Khismatullin and Nadim, 2001). The first mathematical

investigation of the free oscillations of a drop was by Rayleigh (1879), who derived a solution for small amplitude, axisymmetric oscillations of an inviscid and incompressible drop free from the influence of an outer fluid. He described the distortion of the spherical drop as an infinite sum of orthogonal surface spherical harmonics, which corresponds to the natural oscillation modes. For an axisymmetric drop, the radius R is given by

$$R(\theta, t) = R_0 \left[1 + \sum_{l=2}^{\infty} a_l(t) P_l(\cos \theta) \right], \tag{6.1}$$

where $P_l(\cos \theta)$ are the Legendre polynomials of order l, $a_l(t)$ is the instantaneous amplitude of the lth mode of the oscillation (with fundamental mode $l = 2$), θ is the polar angle of a spherical coordinate system with its origin at the centre of the spherical drop and R_0 is the equilibrium radius of the droplet.

For small amplitude oscillations, the angular frequency Ω_l of the lth oscillation mode is given by

$$\Omega_l = \sqrt{\gamma \frac{l(l-1)(l+2)}{\rho R_0^3}}, \tag{6.2}$$

where γ and ρ are the surface tension and density of the fluid, respectively.

Later, more generalised linear analyses incorporated effects of the viscosity of the droplet and viscous effects of an outer fluid. For drops with low viscosity and an oscillation amplitude small compared to R_0, Lamb (1932) obtained an irrotational approximation for an oscillating drop. The amplitude of the lth mode behaves as

$$a_l(t) = A_l \exp \left(i \Omega_l^* t - \frac{t}{\tau_l} \right) \tag{6.3}$$

with a decay time τ_l and an angular frequency of oscillation Ω_l^*, given by

$$\tau_l = \frac{\rho R_0^2}{\mu(l-1)(2l+1)} \tag{6.4}$$

and

$$\Omega_l^* = \Omega_l \sqrt{1 - (\Omega_l \tau_l)^{-2}}, \tag{6.5}$$

where μ is the viscosity of the fluid. The decay time or damping rate depends on density and viscosity and so by measuring both τ_l and Ω_l, both the surface tension and viscosity can be determined. Equations (6.4) and (6.5) are strictly valid only in the limit of small Ohnesorge number. The work of Prosperetti (1980) and Becker et al. (1994) determined that for Ohnesorge number less than 0.1 and small oscillations of fundamental mode $l = 2$ with amplitude not exceeding $0.1 R_0$

the approximation given by equations (6.4) and (6.5) is valid. However, non-linear effects are small even for initial amplitudes as large as $0.2R_0$, where the change in the fundamental frequency Ω_2 is only 2.5% (Becker et al., 1991). Furthermore, Smith (2010) has shown that the time-dependent variations in the decay rate of the fundamental mode, for oscillation amplitudes as large as $0.3R_0$, can be approximated by an additional quadratic component and is less than 25% below the linear result.

At higher Ohnesorge numbers the irrotational solution gives way to an asymptotic solution for the oscillations of a viscous sphere (Prosperetti, 1980) derived by Lamb (1932) and Chandrasekhar (1959), where the restoring force is self-gravity rather than surface tension. Beyond an Ohnesorge number of approximately 0.77 (Prosperetti, 1980) this asymptotic solution no longer gives oscillatory solutions.
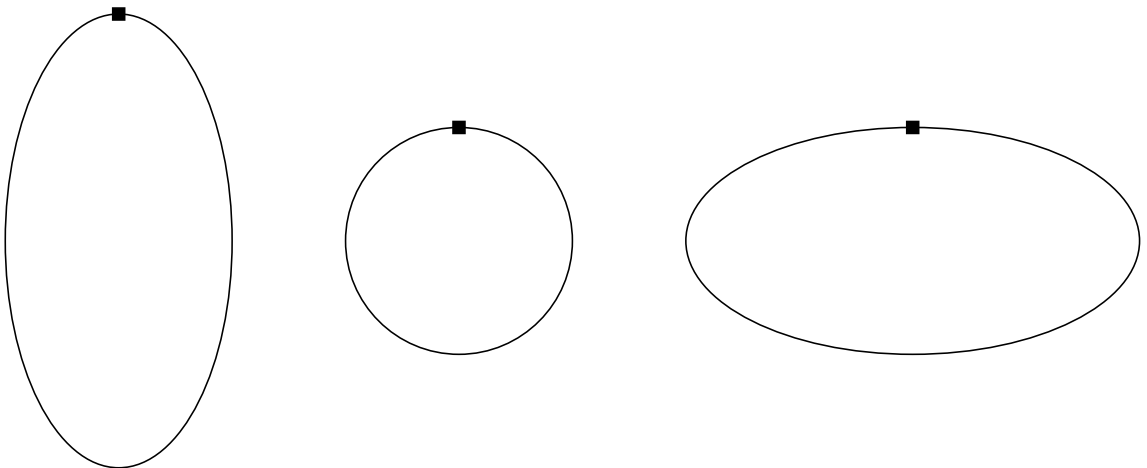
Figure 6.1: The maximum height at each time-step in the simulations is captured. Here, we show the maximum height at different stages of an oscillating cycle, at the maximum value, when the drop has the equilibrium radius and at the minimum value before repeating the cycle.

The fundamental mode ($l = 2$) corresponds to an oscillation between oblate and prolate shapes. Thus, we can define the amplitude of this mode from the maximum radial distance or "height" of the drop surface from the axis, as shown in figure 6.1. By subtracting this from its equilibrium value equal to the drop radius gives a measure of the amplitude of the $l = 2$ mode. Figure 6.2 shows the amplitude-time curve of the shape oscillation for an $R_0 = 34\,\mu\text{m}$ droplet as captured by our simulations, capturing the maximum height at each time-step. Under these operating conditions the fluid properties are given by a viscosity of $0.001\,\text{N}\,\text{s}\,\text{m}^{-2}$, surface tension $0.07\,\text{N}\,\text{m}^{-1}$. With the pure solution parameters we have an Ohnesorge number of 0.017 and hence we are in the regime where the irrotational solution (6.4) and (6.5) is valid.
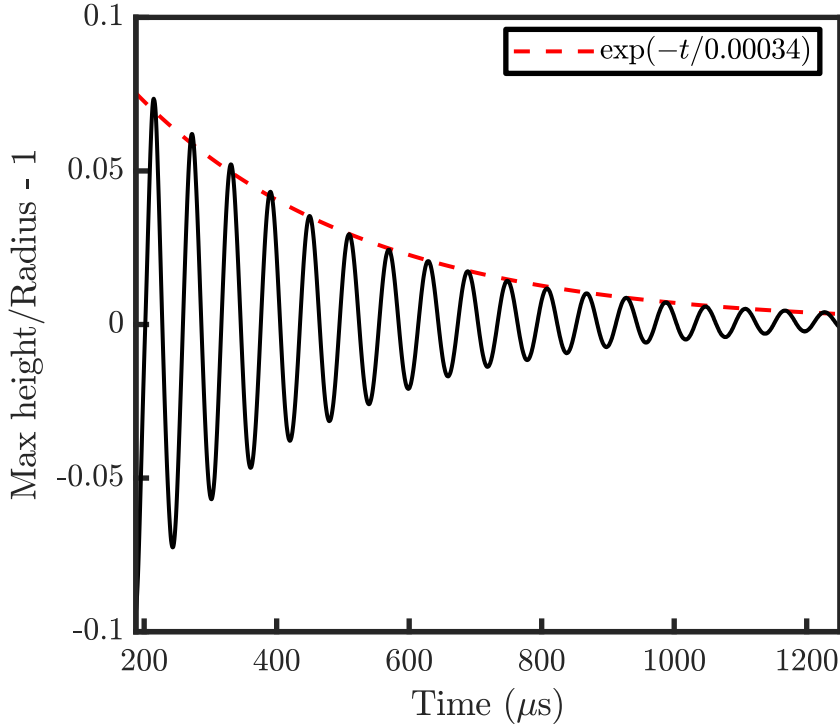
Figure 6.2: The amplitude-time curve of the shape oscillation of a droplet with equilibrium radius $R_0 = 34$ µm. The dashed line shows the fitting of the equation (6.3) to the amplitude data here.

6.3 Dynamic Surface Tension During Jetting

In a surfactant solution, the surface tension is a function of the concentration of the surfactants on the interface. In §5.3, we presented the results of the surfactant distribution along the droplet during the jet process, where the Langmuir-Frumkin surface equation of state (4.8) is used to determine the surface tension and we impose a minimum surface tension equal to the equilibrium surface tension of $0.035\,\mathrm{N\,m^{-1}}$. Initially there is a non-uniform distribution, however for the strong surfactant solution, the surfactant concentration on the surface of the main droplet becomes uniform at the late stages of the process (figure 5.6). Therefore, we expect the drop to have a uniform surface tension but lower than that of the pure solution. In figure 6.3, the pure solution and the surfactant solution droplets are shown at the end of the drop formation process when the droplets have relaxed to a spherical shape and no longer oscillate and therefore we expect no changes in the distribution or surface tension. The surface is coloured depending on the surface tension on the interface. The surfactant solution has a lower, uniform concentration than water.
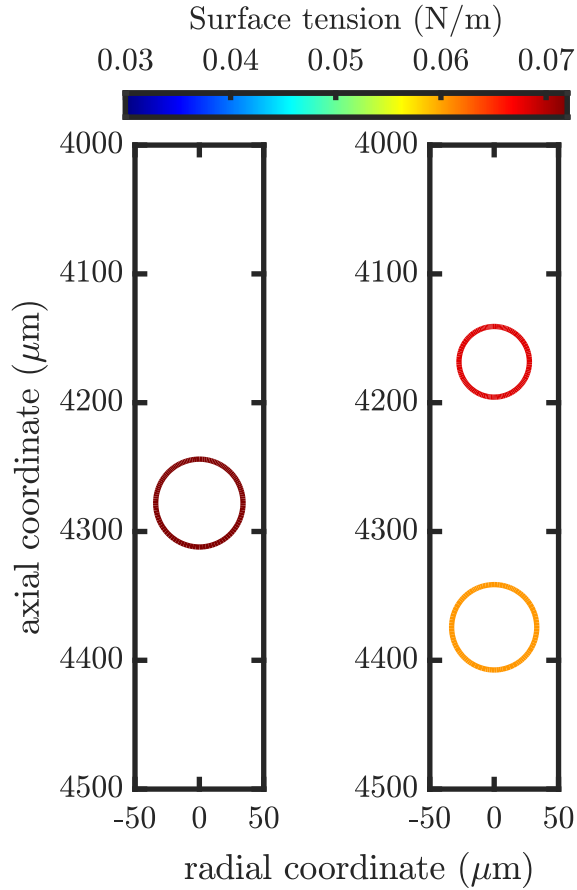
Figure 6.3: Surface tension along the interface of (left) water solution and (right) surfactant solution with surfactant strength of $\beta = 1$ at the final stage of the jet process, where the droplet has reached the equilibrium radius. Both cases have a uniform surface tension along the interface with the surfactant solution showing a lower value than that of the pure solution.

6.4   Drop Oscillation

We now turn our focus to the drop oscillations. In order to achieve a sufficient number of oscillations, the drop speed needs to be reduced to lower values compared to chapters 3 and 5. For this study, an $R_0 = 34$ µm droplet is produced, with a viscosity of $0.001 \, \mathrm{N\,s\,m^{-2}}$ and a surface tension of $0.07 \, \mathrm{N\,m^{-1}}$ at a prescribed speed of $3 \, \mathrm{m\,s^{-1}}$. With the pure solution parameters we have an Ohnesorge number of 0.017 and hence we are in the regime where the irrotational solution (6.4) and (6.5) is valid. We use the Langmuir-Frumkin equation of state for the surface tension calculation,

$$\gamma = 1 + \beta \ln (1 - C) . \tag{6.6}$$

imposing a minimum surface tension equal to the equilibrium surface tension of $0.035 \, \mathrm{N\,m^{-1}}$.

In figure 6.4 we plot the maximum height as a function of time for drops with different values of the surfactant strength parameter β. As with the pure fluid case shown in figure 6.2, the drop oscillations are initiated by the absorption of the ligament into the main drop.
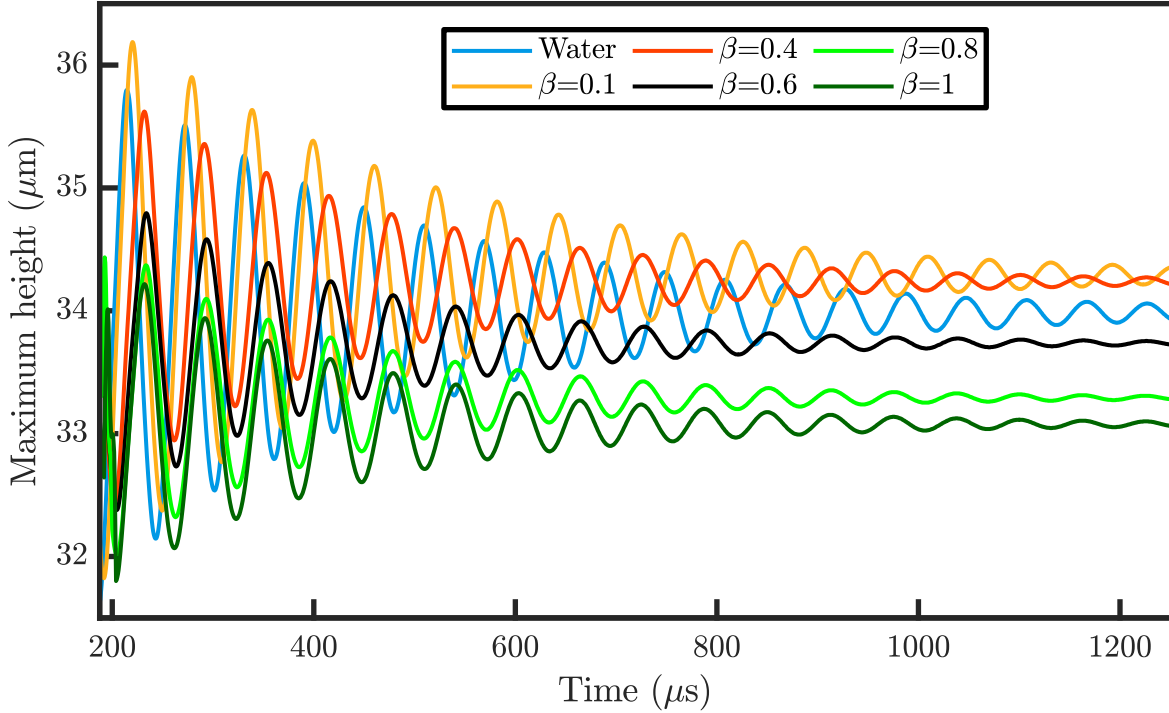
Figure 6.4: Shape oscillation of water and different surfactant solutions at a drop speed of $3\,\mathrm{m\,s^{-1}}$. The initial rapid change is not included in the decay fitting since it is outside the range of the linear model validity.

The equilibrium drop radius is taken as the mean height of the drop oscillations from figure 6.4. In figure 6.5, the estimated equilibrium drop radius is shown for different surfactant strengths. This shows a small increase and then a decrease in drop size with surfactant strength. Although there is a small decrease of around $1\,\mathrm{\mu m}$ in the drop radius with an increase of the surfactant strength, there is not a strong dependence on surfactant strength. The droplet radius depends more critically on the form of the driving waveform, which is kept the same for all the fluids and results in a drop of a similar speed and break-up behaviour (with one satellite formed). The volume of the fluid ejected remains the same for every surfactant solution, however there is a change in the proportion in the satellite drop. More fluid ends up in the satellite for larger β and therefore there is a decrease in the main droplet size.
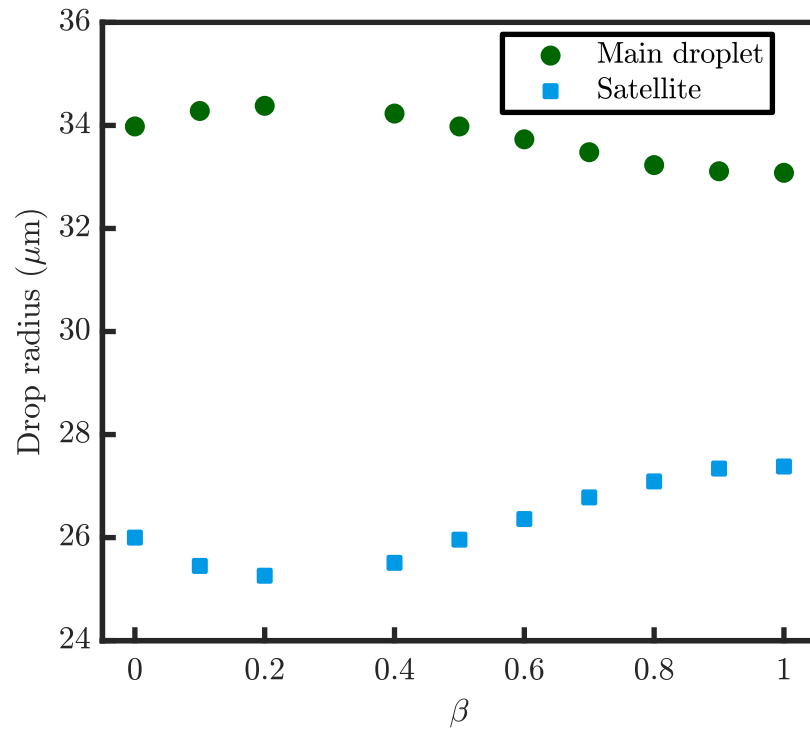
Figure 6.5: The drop radius for the main and the satellite droplet of pure water and different surfactant solutions. The main drop radius decreases with the increasing surfactant strength while the satellite radius increases.
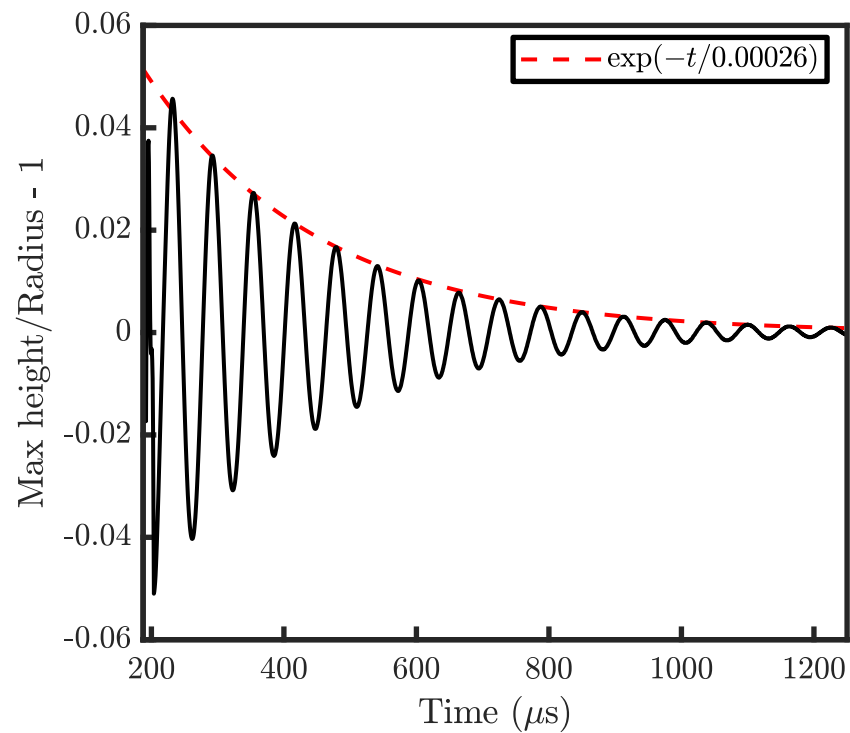
Figure 6.6: The amplitude-time curve of the shape oscillation of a droplet with equilibrium radius $R_0 = 33\,\mu\text{m}$. The dashed line shows the fitting of the equation (6.3) to the amplitude data here.

The amplitude is large at the early stages of the drop oscillation and so is strictly outside the validity of the linear model, which is limited to amplitudes of less than 10%. Moreover, the droplet shape contains important contributions from modes higher than $l = 2$. To avoid these issues when determining the rate of decay of the fundamental mode, we fit equation (6.3) to the later stages, when the amplitude is within the applicable limit of the linear theory and the higher modes have decayed.

In figure 6.6, the amplitude of the drop oscillation is fitted with an exponential decay of the functional form (6.3) for the $\beta = 1$ surfactant solution. Comparing with figure 6.2, it can be seen that the decay of the oscillations remains exponential, but that the timescale for the decay is shorter than for the case of pure water.
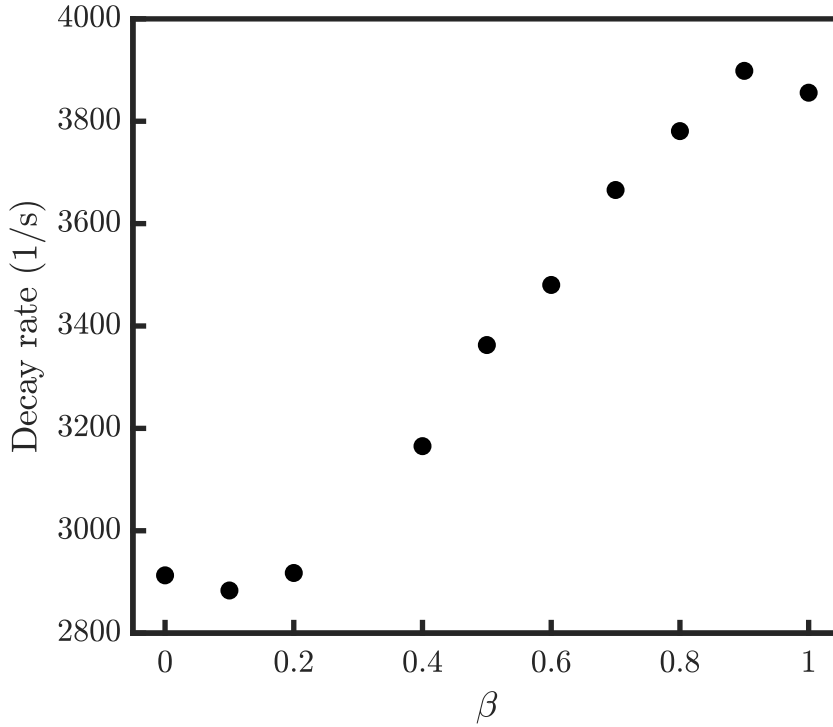
Figure 6.7: Decay rate of the drop oscillation amplitudes for different surfactant strengths.

For each value of β, the decay rate and frequency of the oscillations is estimated by fitting equation (6.3) in the amplitude-time curve of the shape oscillation, as seen in figures 6.2 and 6.6, and are presented in figures 6.7 and 6.8. The decay rate increases significantly with the surfactant strength, whereas there is only a small change in the frequency of 5%. This decrease corresponds to a decrease of 10% in the surface tension, so the equilibrium surface tension of the total drop decreases from $0.072\,\mathrm{N\,m^{-1}}$ to $0.065\,\mathrm{N\,m^{-1}}$. This result runs counter to the interpretation of the frequency and decay using equations (6.4) and (6.5), as an increase in the rate

of decay would suggest an increase in viscosity as opposed to a change in the surface tension. Yet in all these simulations the viscosity of the fluid is the same. Therefore this result shows a different behaviour of the surface because of the surfactants on the interface.
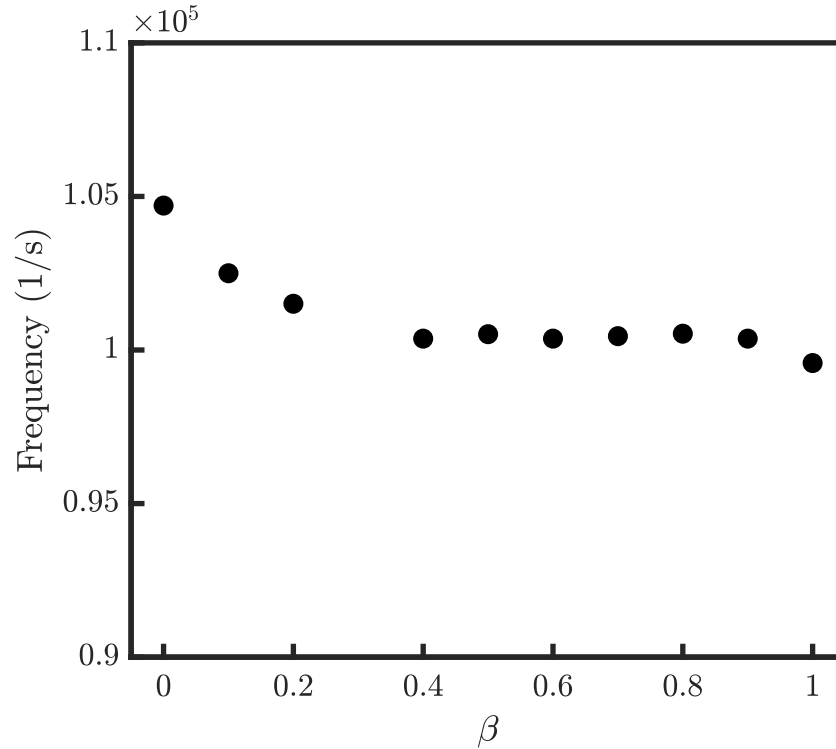
Figure 6.8: Frequency of the drop oscillation amplitudes for different surfactant strengths. There is a small decrease of 5% in the frequency with an increase in the surfactant strength.

To look into this in more depth, we look at the flow inside the droplet at the early stages of oscillation, where the amplitude is large enough to be visible. In figures 6.10 and 6.11, the internal flows within drops of pure water ($\beta = 0$) and with $\beta = 1$ are shown at four different stages of the first oscillation cycle, as indicated in figure 6.9. These are: at the maximum height; at the minimum height; at the equilibrium radius, when the drop height is equal to the drop radius and the subsequent time. To show the internal flow, the mean velocity is subtracted from the velocity at each point so that the velocity arrow shows the velocity in the co-moving domain of the drop.
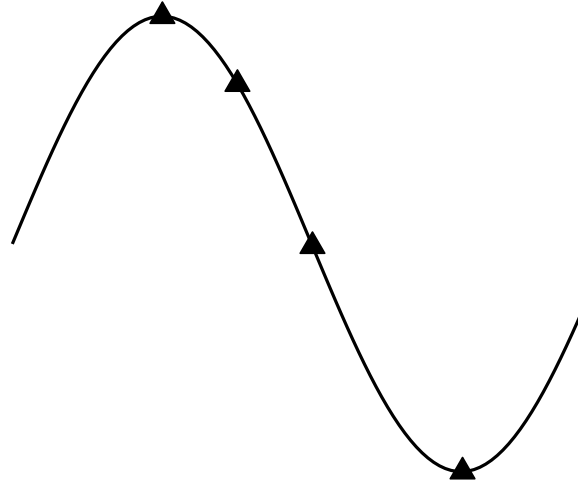
Figure 6.9: Different stages of the drop oscillation cycle where we observe the flow pattern inside the droplet. From left to right: (i) maximum height; (ii) in between stage; (iii) drop is at the equilibrium radius; (iv) minimum height.

(a) At maximum peak

(b) In between peak and equilibrium radius
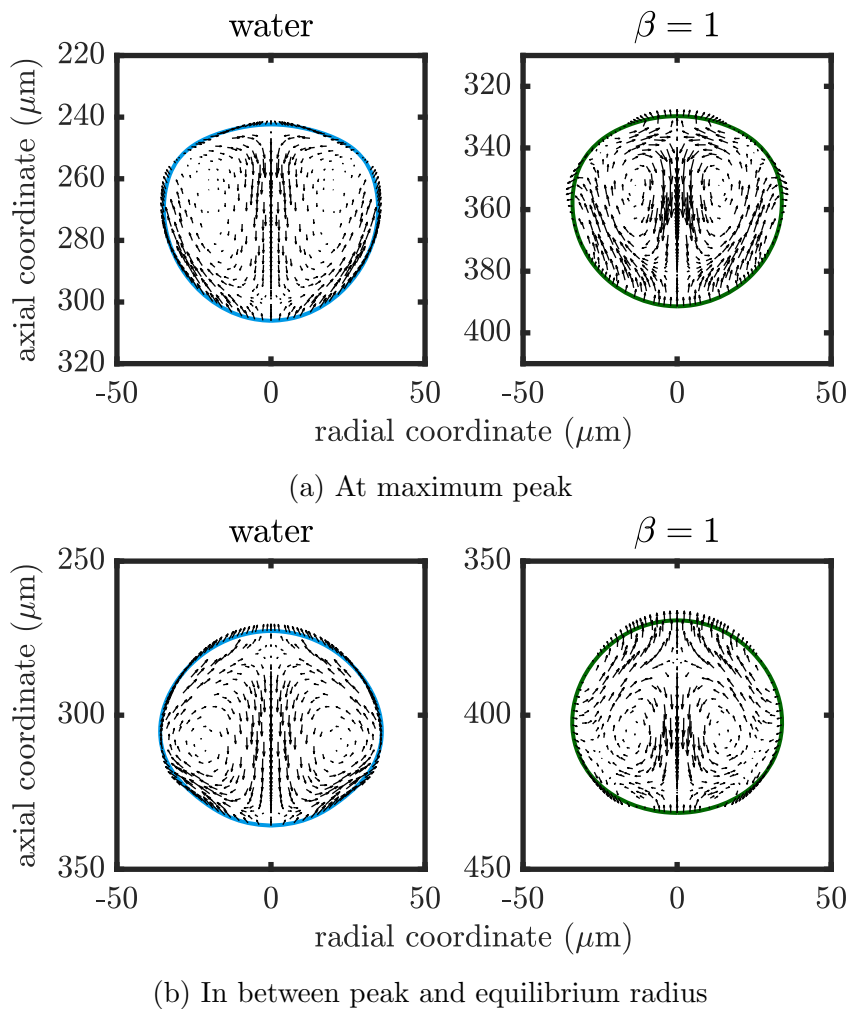
Figure 6.10: Flow relative to the mean velocity inside the droplet normalised by the head drop speed for pure water and for surfactant solution with $\beta = 1$ for the first two stages of the oscillation, as indicated in figure 6.4.

(a) At equilibrium radius

(b) At minimum peak
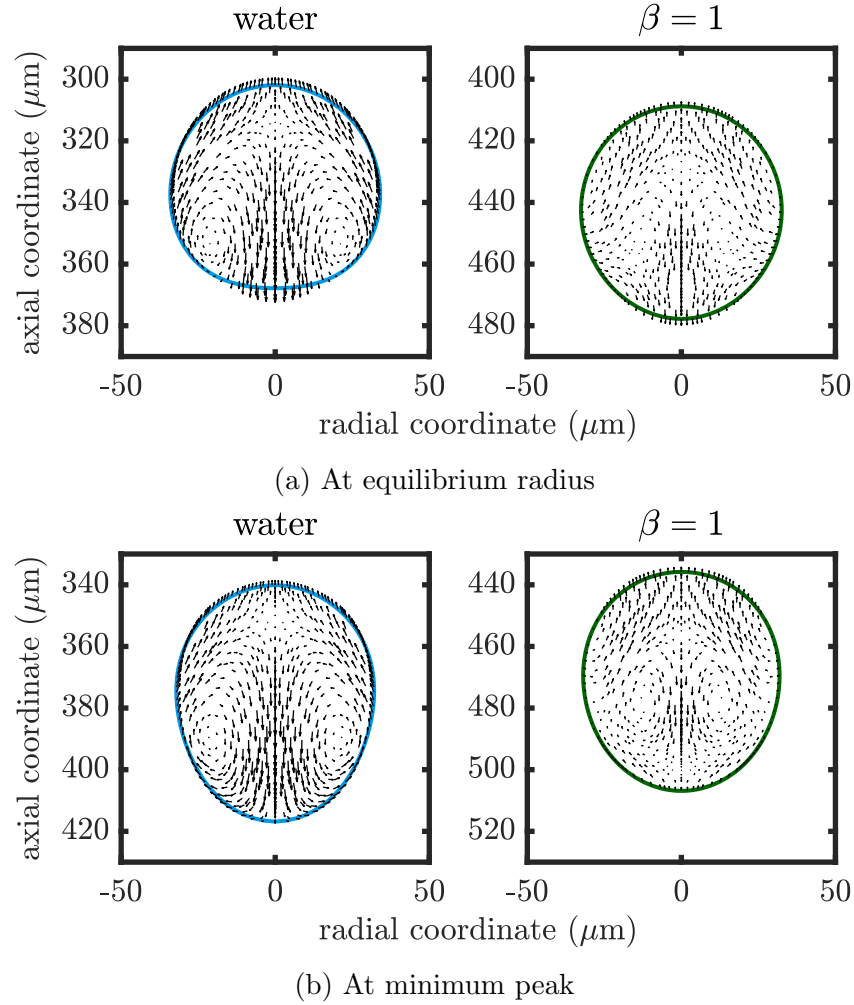
Figure 6.11: Flow relative to the mean velocity inside the droplet normalised by the head drop speed for pure water and for surfactant solution with $\beta = 1$ for the last two stages of the oscillation, as indicated in figure 6.4.

At the maximum height, the flow pattern in both the water and surfactant drops is formed from a jet along the axis caused by the impact of the ligament driving a recirculation cell shown in figure 6.10a. In the case of the pure water drop, this cell occupies the entire drop with the return flow at the drop surface. However for the surfactant coated drop, the return flow is within the interior with the velocity on the drop surface lower in magnitude and directed radially. Note that since this time corresponds to the maximum amplitude of the $l = 2$ mode, the velocity is not affected by this mode. Therefore to see the internal flow corresponding to this mode we need to examine the flow at the time when the velocity generated by this mode is at its maximum, which is approximately at the time when the maximum height is equal to the drop radius shown in figure 6.11a. At this time distortions in the shape are due to higher modes which are larger for the water drop. In both drops, the flow now consists of a superposition of the recirculation cell seen in figure 6.10a and the extensional flow due to the $l = 2$ oscillation. The latter dominates near the surface

whereas the flow near the centre is similar to that at the time shown in figure 6.10a. Again, comparing the water and the surfactant drops, the main difference is that the surface flow is small in magnitude and radially directed in the case of the surfactant drop. At the minimum height (figure 6.11b), we see that the recirculatory flow has decayed more for the surfactant covered drop than is for the water drop.

In figures 6.10 and 6.11, we see that the effect of the surfactant in the solution is to reduce the tangential velocity on the surface compared to the case of pure water. This is because the Marangoni forces act to oppose the gradients of surfactant concentration on the surface, by redistributing surfactants on the surface, producing a surface force that opposes any tangential surface velocity, effectively rigidifying the surfaces.

In the pure water case, the initial recirculation caused by the ligament retraction is evident in every stage of the oscillation. However, when surfactants are present, this flow decays much more rapidly due to the change in boundary condition at the drop surface from zero tangential stress to what is effectively no-slip, as surfactants rigidify the surface. As a consequence, the recirculation is confined to the centre of the droplet and dissipates faster. While this is not the velocity associated with the $l = 2$ mode, the change in boundary condition also acts to dissipate this mode more quickly. Thus, rather than a change in frequency due to the reduction in the normal force $\gamma \nabla_s \cdot \mathbf{nn}$, the main effect of surfactants on drop oscillation is to increase the decay rate of the oscillations arising from the tangential Marangoni force $\nabla_s \gamma$.

6.5   Conclusions

In this chapter, we analysed the effect of surfactants on drop shape oscillations. The key observation here is that Marangoni forces increase the decay rate of the oscillation with the surfactant strength and that this effect is larger than the change in the oscillation frequency. Consequently, care needs to be taken in the interpretation of drop oscillation experiments on complex fluids where surfactants are present as an enhanced rate of decay of oscillations may be due to the surfactants rather than an increased internal viscosity of the drop.

Chapter 7

Conclusions

In this chapter we give a brief summary of the key results from this thesis. Following this, topics of future work are discussed in terms of extending the model to incorporate additional physical processes. In closing, we mention additional applications whose advancement could benefit from our novel results.

7.1 An Overview

Understanding how the addition of surfactants in inks affects their performance requires gaining an understanding of their behaviour during drop formation. This includes several stages from the very early surface generation to jet break-up. In this thesis we have discussed the following problems:

- the effect of viscosity and surface tension on the jetting behaviour for simple Newtonian fluids;

- the transport of surfactants on the newly formed interface;

- the effect of surfactant strength on the surfactant distribution and therefore the jet break-up;

- the effect of surfactants on shape oscillations of drops.

Based on the numerical method of Harlen et al. (1995); Morrison and Harlen (2010), we extended the existing simulation code for jetting of Newtonian fluids to include prediction of the surfactant distribution coupled to the surface

tension via an isotherm. The results for the jetting behaviour have been validated against experimental data. Here we summarise our findings.

Surfactants generally cannot be seen directly and their behaviour is typically understood based on how they modify flows. Surfactant distributions are thus typically inferred from observable fluid phenomena like measured fluid velocity fields, free-surface dynamics or Laplace pressure measurements. Connecting measurements and observations with the underlying surfactant fields however, requires a model for the dynamics and mechanics of surfactant transport. Using the Langmuir-Frumkin surface equation of state, which predicts the surface tension based on the surfactant concentration, a local in space and time-dependent surface tension is computed. This gives rise to Marangoni stress which affects the new surface formation significantly.

An important observation is that the surfactants stay at the head of the droplet during the whole jetting process and only for strong surfactants there is a more uniform distribution at later times. At the length- and timescales of inkjet printing, the surfactant diffusion on the interface is significantly slower compared to the new surface generation and surface advection and therefore is not important for the transport along the interface. The dominant mechanism for the distribution is the surface velocity and includes the Marangoni flows which arise from the large surfactant concentration gradients on the droplet interface.

These large concentration gradients result in a strong Marangoni stress around the vicinity of the neck. This delays the break-off time and for some cases, it can even prevent the formation of any satellites. The stronger the surfactant is, the later the break-off happens. By examining the thinning rate of the neck radius, we saw that this system follows the prediction of Day et al. (1998) for the thinning of an inviscid fluid but the increasing surfactant strength slows it down. Therefore, we can conclude that the surfactants do not affect the Newtonian properties of the fluid however they change the dynamics of the break-up by affecting the surface tension locally.

Although our model assumes that the viscosity of the bulk fluid is not affected by surfactants, our study on the drop oscillations showed that the there is a significant increase in the decay rate of the oscillation. This method has been used to measure the instantaneous surface tension and the viscosity of fluids at the point of drop formation. Our study shows that the interpretation of these measurements should be careful when surfactants are present since the Marangoni forces result in an enhanced decay rate that is not caused by an actual increase in the viscosity of the drop.

7.1.1 Implications for inkjet printing

In terms of the effect of surfactants on inkjet printing, the main conclusion of the thesis is that for the typical small molecule surfactants such as Triton X-100 and Surfynol 465 for $\beta = 0.1$ to 0.2, the presence of surfactants does not greatly change jet break-up and drop formation for an inkjet printer compared to the same fluid in the absence of surfactant.

The rapid expansion of the interface leaves much of the surface surfactant-free and while Marangoni stresses do affect the break-off, for these surfactants the effect is weak. This is confirmed by experimental observations that find little difference between the drop formation with and without surfactants. Our simulations do however suggest that stronger surfactants with $\beta > 0.5$ would promote an effect. We also found that fluids with surfactants printed more stably than fluids with a high surface tension, which tended to flood the print-head.

7.2 Future Work

This thesis has looked into more detail the addition of surfactants in the inks used in the DOD method of inkjet printing. Even though we have presented a detailed model and extended analysis of the effect the surfactants have on jet break-up, we have omitted some complications and subtleties that impact many different fields of science, industry and life.

7.2.1 Solubility

In this work, we neglected the exchange of surfactants between the bulk and the surface. On the timescales of inkjet printing of microseconds, the bulk exchange can be negligible, therefore this assumption is valid. However, for different applications or larger size droplets, the effect of solubility can become important. When a new surface is created, it is initially free of surfactants. The gradual adsorption of surfactants on the interface from the bulk results in a non-uniform decrease of surface tension with time. Therefore, the transfer of surfactant to and from the interface can diminish the magnitude of surfactant gradients.

Many surfactants are soluble, meaning that the surface excess concentration of adsorbed surfactants equilibrates with the bulk concentration according to

an isotherm. When a drop is initially coated with soluble surfactant at surface coverage and then deformed to create an extra area, the interfacial concentration drops below its equilibrium with the bulk concentration. Bulk surfactant is then driven to adsorb to the interface, until the equilibrium surface coverage is restored. At steady state, the surface tension of the drop is thus equal to the initial, equilibrium value which is lower than the clear interface surface tension.

Milliken and Leal (1994) studied the effect of solubility in the drop deformation in an extensional flow and showed that in the presence of a soluble surfactant the drop deformation lies between the insoluble surfactant case and the uniform surfactant coverage case. Most importantly though, their results showed that while the insoluble surfactant can substantially retard the drop interface, a soluble surfactant remobilises the interface and therefore the interfacial velocity is different. Other studies of the effect of solubility have examined a rising bubble (Holbrook and Levan, 1983a,b), while more recent work of Kovalchuk et al. (2016) looked at the solubility effect on the satellite formation using experiments on liquid bridges. The adsoprtion of the surfactant onto the surface of a growing and detaching droplet is a slow diffusion-controlled process and therefore the dynamic surface tension can deviate considerable from the equilibrium value (MacLeod and Radke, 1994). As Stubenrauch et al. (2005) have shown, the dynamic surface tension of an aqueous solution with a soluble surfactant at a concentration slightly above CMC reaches the equilibrium value at a time exceeding $10\,\mathrm{s}$ and the equilibration time increases with a decrease of the concentration. Theoretical and numerical studies have been conducted looking at the effect of solubility on liquid bridges and filaments (Milliken and Leal, 1994; Hansen et al., 1999; Craster et al., 2009). It has been shown that both stabilisation mechanisms found for the case of insoluble surfactants also apply for the soluble surfactants and their importance depends on surfactant concentration and the presence of micelles. Craster et al. (2009) predicted that Marangoni stresses can cause formation of large satellite droplets at high surfactant concentrations.

Monolayers of soluble surfactants, called Gibbs monolayers, represent an equilibrium between surfactants adsorbed at the interface (with concentration Γ) and those dissolved in the bulk (with concentration c_b). Detailed balance must hold for adsorbed and dissolved surfactants to be in equilibrium: as many surfactants must adsorb to a surface as desorb in any given time. For this to happen spontaneously, the two states must be equivalent from a free energy standpoint. Adding one surfactant to the monolayer costs energy, the chemical potential $\mu_s(\Gamma)$ of the adsorbed surfactant. This free energy must be identical to the free energy liberated by removing that surfactant from the subphase - represented by the chemical potential $\mu_b(c)$ of the surfactant in the bulk. In short, equilibrium between dissolved

and adsorbed surfactant requires

$$\mu_s(\Gamma) = \mu_b(c)\,,$$

which defines the equilibrium isotherm $\Gamma(c)$.

When surfactants are sufficiently dilute in solution and adsorbed surfactants form an ideal gas monolayer, they have an ideal chemical potential. Then by equating the chemical potentials, we get a linear relation between adsorbed and bulk concentrations,

$$\Gamma^{\text{ideal}} = K^{\text{ideal}}c\,, \tag{7.1}$$

where K^{ideal} is an equilibrium constant for adsorption.

Equilibrium between surfactants adsorbed at an interface and dissolved in the subphase can also be determined by explicitly balancing adsorption and desorption fluxes. In fluid mechanics, this approach is important as it connects the equilibrium arguments and measurements to Marangoni stresses and dynamical processes in surfactant systems. The simplest expressions and desorption fluxes, which are valid for ideal mixtures, is to take the adsorption flux, $\dot{\jmath}_a$, to be proportional to the bulk concentration c_b and the desorption flux, $\dot{\jmath}_d$, to be proportional to the adsorbed concentration Γ,

$$\begin{aligned}
\dot{\jmath}_a &= k_a c \\
\dot{\jmath}_d &= k_d \Gamma\,.
\end{aligned}$$

These fluxes balance at equilibrium, $\dot{\jmath}_a = \dot{\jmath}_d$, giving

$$\Gamma^{\text{ideal}} = \frac{k_a}{k_d}c \equiv K^{\text{ideal}}c$$

reproducing the Henry isotherm equation (7.1). Note that each individual rate constant k_a and k_d can not be determined from an equilibrium; however, the ratio of the two is set by thermodynamics.

Surfactants do not always show ideal behaviour. The most common example is micellisation when above CMC, some surfactants spontaneously aggregate to form micelles. Micellisation provides an energetic alternative to further interfacial adsorption: once conditions favour micelle formation, adding further surfactants tends to form additional micelles rather than increase interfacial concentration. The CMC is estimated by identifying the bulk concentration at which the surface tension, and therefore the surface concentration, becomes approximately constant.

7.2.2 Coalescence

Surfactant may provide additional energetic barriers to droplet coalescence. Surfactants on either side of a liquid film may repel each other and thus retard or arrest the thinning of the film (Bibette et al., 1992; Stancik et al., 2004). The recent work of Sykes et al. (2020) studied the effect of different surface tension droplets in the surface jet and the internal mixing of impacting droplets. By introducing surface tension differences between the coalescing droplets, they showed that the surface jet can be either enhanced or suppressed via a Marangoni flow. The influence of the relative surface tension on the long-term dynamics and mixing efficiency has been considered however only on Newtonian fluids.

The addition of surfactants will enhance further the existent surface tension gradient and it will also create further local gradients due to the non-uniform surfactant distribution. The competitive timescales here will be different compared to the inkjet printing ones. The coalescence of the droplets can be faster than the surface generation, however the generation of the surface jet and the duration of the mixing inside the droplet are sufficiently long for surfactants to diffuse from the bulk to the interface. The induced Marangoni flows can be enhanced or suppressed depending on the existing surface tension gradient between the sessile and the impacted droplet.

Special consideration will need to be taken both in the numerical approach as well as in experiments. Experimentally, the timescales are already very small for the cameras to capture the evolution of the surface and the surfactants themselves are effectively invisible to most techniques. Numerically, the competitive timescales can create convergence issues and therefore a different scheme will need to taken into account. A suggestion is to use an implicit-explicit approach, where there will be two different timesteps for each process, i.e. the coalescence and the transport.

7.3 Extended Applications

Surfactants control the initiation, dynamics and behaviour of other processes besides droplet formation and coalescence. We will now discuss paradigmatic problems of fluid mechanics that are impacted by surfactants: thin films and foams. Our work in droplets and the modelling approaches we developed can be applied and extended to these problems. The specificity of these problems is given by the choice of the geometry and boundary conditions, which can be incorporated in our framework.

However, these problems are not an immediate extension of our work and additional physical mechanisms may need to be considered for a complete model.

7.3.1 Thin films: thickness of coating and surfactants

Thin fluid films are central to engineering and biophysical flows, many of which involve surfactants. Blinking involves the dynamics of a tear film, breathing includes the dynamics of an the alveolar fluid film and painting leaves a thin liquid film that eventually dries. Industrial machinery is often coated with thin films of lubricant, parts and products are coated by flowing a liquid film over the object. The effects of surface viscosity and Marangoni flows can not always be neatly differentiated in many of these applications, as with surfactant-covered drops and bubbles, oscillatory compression of interfaces and damping of surface waves.

Dip coating is perhaps the easiest way to deposit a thin liquid film on an object, in which the object is immersed in a liquid reservoir and then pulled out. The thickness h_{LLD} of the entrained liquid layer depends on the velocity v of the substrate and the density, viscosity and surface tension of the liquid being drawn out as given by the classic Landau-Levich-Derjaguin (LLD) law,

$$\frac{h_{\mathrm{LLD}}}{l_c} \approx 0.946 \mathrm{Ca}^{2/3} \,,$$

where

$$l_c = \sqrt{\frac{\gamma}{\rho g}} \,,$$

is the capillary length (Levich and Landau, 1942; Quéré, 1999) and $\mathrm{Ca} = \mu v/\gamma$ is the capillary number.

The fluid being drawn out of the bath is rarely pure in most applications and it has long been known that surfactants enhance the thickness h_0 of the film. Reverse Marangoni stresses and possibly surface rheological stresses immobilise the interface, dragging excess liquid along with the surface. Adapting the LLD law to accommodate various surfactant processes requires a description of the fluid dynamics of the entrained film.

Surfactants give rise to Marangoni and surface viscous forces that resist interfacial stretching. Surface fluid flows establish gradients in surface concentration, which exert reverse Marangoni stresses. Adsorption and desorption weakens the Marangoni effect and reduces the thickening factor (Ou Ramdane and Quéré, 1997). However, as with oscillating droplets the distinct effects of adsorption/desorption

and intrinsic surface viscosities are not easy to differentiate. The role of surface viscosity in dip coating has only recently gained attention (Scheid et al., 2010; Delacotte et al., 2012; Seiwert et al., 2014) in systems with negligible Marangoni forces, e.g. when rapid adsorption/desorption eliminates surface tension gradients.

Effective surfactant exchange requires the film to be thicker than the depletion depth so as not to be constrained (Quéré, 1999; Delacotte et al., 2012) by the lack of sufficient dissolved molecules. Suppressing Marangoni flows therefore requires large surfactant concentrations, large withdrawing velocities and eliminating energetic barriers to adsorption. Delacotte et al. (2012) measured enhanced film thickness in unconfined films despite the rapid adsorption, suggesting that surface viscosity does indeed play a role in immobilising interfaces. However, the two surface viscosities, the intrinsic surface shear and surface dilatation, still remain indistinguishable in 1D surface deformations.

7.3.2 Foams: surfactant and macroscopic flows

Foams are examples of complex multiphase materials, with ubiquitous applications in the kitchen, cleaning, packaging and superlight construction materials, like metal foams. For our discussions, aqueous foams are more relevant, which are stabilised against rupture by adsorbed surfactant molecules. The type and rheology of the surfactant influences its stability and its macroscopic flow (Cohen-Addad et al., 2013).

An interesting problem is foam drainage, the gravity-driven flow of liquid within an aqueous foam. The geometry of soap foams is complicated, but can be described by few basic rules of energy minimisation, as first described by Joseph Plateau in the 19th century (Manikantan and Squires, 2020). The liquid content in a foam resides mostly in a network of channels connected to each other at nodes, where four channels meet in a tetrahedral configuration.

Surfactants modify fluid flow within these channels and nodes, systematically altering macroscopic foam drainage. A qualitative picture of how surfactant processes impact measurable macroscopic foam properties can be gained by using a surfactant transport model accounting for flow within channels and nodes and using a macroscopic model linking all surfactant processes into course-grained coefficients. Durand and Langevin (2002) solved the surfactant concentration equation coupled to the drainage equation for each channel. A generalised 3D foam drainage equation can be derived where all numerical constants depend on the particular geometry of

the Plateau borders (Koehler et al., 2000).

There are two distinct limit regimes where the channels can be treated differently. When the surface diffusion is weak and therefore the Marangoni flows are strongest, the channels are essentially no-slip walls and bulk fluid flow is Poiseuille-like. When the surface diffusion is strong and quickly eliminates surface concentration gradients, the Marangoni flows are weakened and therefore the surface is completely stress-free.

Forced foam drainage experiments introduce fluid at flow rate Q into a dry foam from the top and track the velocity v of a wet front as it moves through the foam. Experimentally, it is found that the front moves at a velocity

$$v \propto Q^\alpha \,,$$

where the exponent α is typically between 1/3 and 1/2 (Verbist et al., 1996; Koehler et al., 2000; Durand and Langevin, 2002). Surfactant processes change the character of drainage based on the extent of surface immobilisation and therefore impact this exponent in a measurable way. Durand and Langevin (2002) measured the exponent α to transition between the two types of flow upon modifying surface rheology which is referred to as 'Kraynik criterion'.

What was previously attributed to dissipation due to surface shear viscosity might arise from an intrinsic surface dilatational viscosity due to Marangoni stresses with finite-time adsorption/desorption or some combination. More generally therefore, the transition from one drainage regime to the other should depend on the degree of immobilisation.

Bibliography

Ainsley, C., Reis, N., and Derby, B. 2002. Freeform fabrication by controlled droplet deposition of powder filled melts. *Journal of Materials Science.* **37**(15), pp. 3155–3161. Cited on p. 1.

Alart, P., Maisonneuve, O., and Rockafellar, R. T. 2006. *Nonsmooth mechanics and analysis: theoretical and numerical advances*, volume 12. Springer Science & Business Media. Cited on p. 3.

Alvarez, N. J., Walker, L. M., and Anna, S. L. 2010. Diffusion-limited adsorption to a spherical geometry: The impact of curvature and competitive time scales. *Physical Review E.* **82**(1), pp. 011604. Cited on pp. 20 and 103.

Ambravaneswaran, B. and Basaran, O. A. 1999. Effects of insoluble surfactants on the nonlinear deformation and breakup of stretching liquid bridges. *Physics of Fluids.* **11**(5), pp. 997–1015. Cited on pp. 13 and 82.

Anthony, C. R., Kamat, P. M., Harris, M. T., and Basaran, O. A. 2019. Dynamics of contracting filaments. *Physical Review Fluids.* **4**(9), pp. 093601. Cited on p. 36.

Basaran, O. A., Gao, H., and Bhat, P. P. 2013. Nonstandard inkjets. *Annual Review of Fluid Mechanics.* **45**, pp. 85–113. Cited on pp. 3, 4, 5, 16, and 35.

Batchelor, G. K. 2000. *An introduction to fluid dynamics.* Cambridge university press. Cited on p. 23.

Becker, E., Hiller, W., and Kowalewski, T. 1991. Experimental and theoretical investigation of large-amplitude oscillations of liquid droplets. *Journal of Fluid Mechanics.* **231**, pp. 189–210. Cited on pp. 102 and 105.

Becker, E., Hiller, W., and Kowalewski, T. 1994. Nonlinear dynamics of viscous droplets. *Journal of Fluid Mechanics.* **258**, pp. 191–191. Cited on pp. 103 and 104.

Bibette, J., Morse, D. C., Witten, T., and Weitz, D. 1992. Stability criteria for emulsions. *Physical Review Letters.* **69**(16), pp. 2439. Cited on p. 120.

Brenn, G. and Teichtmeister, S. 2013. Linear shape oscillations and polymeric time scales of viscoelastic drops. *Journal of Fluid Mechanics.* **733**, pp. 504. Cited on p. 102.

Castrejon-Pita, A. A., Castrejon-Pita, J. R., and Hutchings, I. M. 2012. Breakup of liquid filaments. *Physical Review Letters.* **108**(7), pp. 074506. Cited on pp. 36 and 53.

Castrejón-Pita, J., Morrison, N., Harlen, O., Martin, G., and Hutchings, I. 2011. Experiments and lagrangian simulations on the formation of droplets in drop-on-demand mode. *Physical Review E.* **83**(3), pp. 036306. Cited on pp. 6, 26, and 36.

Chandrasekhar, S. 1959. The oscillations of a viscous liquid globe. *Proceedings of the London Mathematical Society.* **3**(1), pp. 141–149. Cited on pp. 103 and 105.

Chang, C.-H. and Franses, E. I. 1995. Adsorption dynamics of surfactants at the air/water interface: a critical review of mathematical models, data, and mechanisms. *Colloids and Surfaces A: Physicochemical and Engineering Aspects.* **100**, pp. 1–45. Cited on pp. 18, 55, and 103.

Cohen-Addad, S., Höhler, R., and Pitois, O. 2013. Flow in foams and flowing foams. *Annual Review of Fluid Mechanics.* **45**. Cited on pp. 13 and 122.

Craster, R., Matar, O., and Papageorgiou, D. 2002. Pinchoff and satellite formation in surfactant covered viscous threads. *Physics of Fluids.* **14**(4), pp. 1364–1376. Cited on pp. 14 and 82.

Craster, R., Matar, O., and Papageorgiou, D. 2009. Breakup of surfactant-laden jets above the critical micelle concentration. *Journal of Fluid Mechanics.* **629**, pp. 195–219. Cited on p. 118.

Darhuber, A. A. and Troian, S. M. 2005. Principles of microfluidic actuation by modulation of surface stresses. *Annual Review of Fluid Mechanics.* **37**, pp. 425–455. Cited on p. 13.

Davis, R. and Acrivos, A. 1966. The influence of surfactants on the creeping motion of bubbles. *Chemical Engineering Science.* **21**(8), pp. 681–685. Cited on p. 16.

Day, R. F., Hinch, E. J., and Lister, J. R. 1998. Self-similar capillary pinchoff of an inviscid fluid. *Physical Review Letters.* **80**(4), pp. 704. Cited on pp. 11, 88, 92, 93, 94, 100, and 116.

de Jong, J., de Bruin, G., Reinten, H., van den Berg, M., Wijshoff, H., Versluis, M., and Lohse, D. 2006. Air entrapment in piezo-driven inkjet printheads. *The Journal of the Acoustical Society of America.* **120**(3), pp. 1257–1265. Cited on p. 36.

Deen, W. M. 1998. *Analysis of transport phenomena.* Oxford University Press New York. Cited on p. 27.

Delacotte, J., Montel, L., Restagno, F., Scheid, B., Dollet, B., Stone, H. A., Langevin, D., and Rio, E. 2012. Plate coating: influence of concentrated surfactants on the film thickness. *Langmuir.* **28**(8), pp. 3821–3830. Cited on p. 122.

Derby, B. 2010. Inkjet printing of functional and structural materials: fluid property requirements, feature stability, and resolution. *Annual Review of Materials Research.* **40**, pp. 395–414. Cited on pp. 8 and 35.

Dijksman, J. 1984. Hydrodynamics of small tubular pumps. *Journal of Fluid Mechanics.* **139**, pp. 173–191. Cited on p. 75.

Dijksman, J. 1998. Hydro-acoustics of piezoelectrically driven ink-jet print heads. *Flow, Turbulence and Combustion.* **61**(1-4), pp. 211–237. Cited on p. 75.

Dong, H., Carr, W. W., and Morris, J. F. 2006. An experimental study of drop-on-demand drop formation. *Physics of Fluids.* **18**(7), pp. 072102. Cited on pp. 36, 37, 40, and 46.

Durand, M. and Langevin, D. 2002. Physicochemical approach to the theory of foam drainage. *The European Physical Journal E.* **7**(1), pp. 35–44. Cited on pp. 122 and 123.

Eastoe, J. and Dalton, J. 2000. Dynamic surface tension and adsorption mechanisms of surfactants at the air–water interface. *Advances in Colloid and Interface Science.* **85**(2-3), pp. 103–144. Cited on pp. 19 and 103.

Eggers, J. 1993. Universal pinching of 3d axisymmetric free-surface flow. *Physical Review Letters.* **71**(21), pp. 3458. Cited on p. 11.

Eggers, J. 1997. Nonlinear dynamics and breakup of free-surface flows. *Reviews of Modern Physics.* **69**(3), pp. 865. Cited on p. 10.

Eggers, J. and Villermaux, E. 2008. Physics of liquid jets. *Reports on Progress in Physics.* **71**(3), pp. 036601. Cited on p. 12.

Eggleton, C. D., Pawar, Y. P., and Stebe, K. J. 1999. Insoluble surfactants on a drop in an extensional flow: a generalization of the stagnated surface limit to deforming interfaces. *Journal of Fluid Mechanics.* **385**, pp. 79–99. Cited on p. 13.

Ferri, J. K. and Stebe, K. J. 1999. Soluble surfactants undergoing surface phase transitions: A maxwell construction and the dynamic surface tension. *Journal of Colloid and Interface Science.* **209**(1), pp. 1–9. Cited on p. 20.

Ferri, J. K. and Stebe, K. J. 2000. Which surfactants reduce surface tension faster? a scaling argument for diffusion-controlled adsorption. *Advances in Colloid and Interface Science.* **85**(1), pp. 61–97. Cited on p. 103.

Franses, E. I., Basaran, O. A., and Chang, C.-H. 1996. Techniques to measure dynamic surface tension. *Current Opinion in Colloid & Interface Science.* **1**(2), pp. 296–303. Cited on pp. 16, 101, and 103.

Frumkin, A. 1925. Electrocapillary curve of higher aliphatic acids and the state equation of the surface layer. *Zeitschrift für Physikalische Chemie.* **116**, pp. 466–470. Cited on p. 19.

Gresho, P. and Sani, R. 1998. Incompressible flow and the finite element method. volume 2: Incompressible flow and finite element. Cited on p. 27.

Hansen, S., Peters, G., and Meijer, H. 1999. The effect of surfactant on the stability of a fluid filament embedded in a viscous fluid. *Journal of Fluid Mechanics.* **382**, pp. 331–349. Cited on p. 118.

Harlen, O., Rallison, J., and Szabo, P. 1995. A split lagrangian-eulerian method for simulating transient viscoelastic flows. *Journal of Non-Newtonian Fluid Mechanics.* **60**(1), pp. 81–104. Cited on pp. 26, 34, 58, 59, and 115.

Hiller, W. and Kowalewski, T. 1989. Surface tension measurements by the oscillating droplet method. *PhysicoChemical Hydrodynamics.* **11**, pp. 103–112. Cited on p. 102.

Hoath, S., Martin, G., Castrejón-Pita, R., and Hutchings, I. Satellite formation in drop-on-demand printing of polymer solutions. In *NIP & Digital Fabrication Conference*, volume 2007, pp. 331–335. Society for Imaging Science and Technology, 2007. Cited on p. 1.

Hoath, S., Jung, J., and Hutchings, I. M. 2013. A simple criterion for filament break-up in drop-on-demand inkjet printing. *Physics of Fluids.* **25**, pp. 021701. Cited on pp. 7, 8, and 53.

Hoath, S. D. 2016. *Fundamentals of Inkjet Printing: The Science of Inkjet and Droplets.* John Wiley & Sons. Cited on pp. 2, 3, 4, 5, 44, and 52.

Hoath, S. D., Harlen, O. G., and Hutchings, I. M. 2012. Jetting behavior of polymer solutions in drop-on-demand inkjet printing. *Journal of Rheology.* **56**(5), pp. 1109–1127. Cited on p. 36.

Hoath, S. D., Hsiao, W.-K., Martin, G. D., Jung, S., Butler, S. A., Morrison, N. F., Harlen, O. G., Yang, L. S., Bain, C. D., and Hutchings, I. M. 2015. Oscillations of aqueous pedot: Pss fluid droplets and the properties of complex fluids in drop-on-demand inkjet printing. *Journal of Non-Newtonian Fluid Mechanics.* **223**, pp. 28–36. Cited on pp. 102 and 103.

Holbrook, J. A. and Levan, M. D. 1983a. Retardation of droplet motion by surfactant. part 1. theoretical development and asymptotic solutions. *Chemical Engineering Communications.* **20**(3-4), pp. 191–207. Cited on pp. 16 and 118.

Holbrook, J. A. and Levan, M. D. 1983b. Retardation of droplet motion by surfactant. part 2. numerical solutions for exterior diffusion, surface diffusion, and adsorption kinetics. *Chemical Engineering Communications.* **20**(5-6), pp. 273–290. Cited on p. 118.

Hutchings, I., Martin, G., and Hoath, S. 2007. High speed imaging and analysis of jet and drop formation. *Journal of Imaging Science and Technology.* **51**(5), pp. 438–444. Cited on pp. 35 and 36.

Hutchings, I. M. and Martin, G. D. 2012. *Inkjet technology for digital fabrication.* John Wiley & Sons. Cited on pp. 2 and 52.

Ishiwata, T. and Sakai, K. 2014. Dynamic surface tension measurement with temporal resolution on microsecond scale. *Applied Physics Express.* **7**(7), pp. 077301. Cited on p. 102.

Jin, F., Balasubramaniam, R., and Stebe, K. J. 2004. Surfactant adsorption to spherical particles: The intrinsic length scale governing the shift from diffusion to kinetic-controlled mass transfer. *The Journal of Adhesion.* **80**(9), pp. 773–796. Cited on p. 20.

Kalogirou, A. 2018. Instability of two-layer film flows due to the interacting effects of surfactants, inertia, and gravity. *Physics of Fluids.* **30**(3), pp. 030707. Cited on p. 14.

Kamat, P. M., Wagoner, B. W., Thete, S. S., and Basaran, O. A. 2018. Role of marangoni stress during breakup of surfactant-covered liquid threads: Reduced

rates of thinning and microthread cascades. *Physical Review Fluids.* **3**(4), pp. 043602. Cited on pp. 14 and 82.

Khismatullin, D. B. and Nadim, A. 2001. Shape oscillations of a viscoelastic drop. *Physical Review E.* **63**(6), pp. 061508. Cited on pp. 102 and 103.

Koehler, S. A., Hilgenfeldt, S., and Stone, H. A. 2000. A generalized view of foam drainage: experiment and theory. *Langmuir.* **16**(15), pp. 6327–6341. Cited on p. 123.

Kovalchuk, N. M., Nowak, E., and Simmons, M. J. 2016. Effect of soluble surfactants on the kinetics of thinning of liquid bridges during drops formation and on size of satellite droplets. *Langmuir.* **32**(20), pp. 5069–5077. Cited on p. 118.

Kyser, E. L. and Sears, S. B. Method and apparatus for recording with writing fluids and drop projection means therefor, Mar. 23 1976. US Patent 3,946,398. Cited on p. 4.

Lamb, H. 1932. *Hydrodrynamics.* Cambridge University Press, 6th edition. Cited on pp. 103, 104, and 105.

Langmuir, I. 1918. The adsorption of gases on plane surfaces of glass, mica and platinum. *Journal of the American Chemical Society.* **40**(9), pp. 1361–1403. Cited on p. 18.

Laplace, P. 1805. Mechanique celeste supplement aux libre. *Courier: Paris.* Cited on p. 9.

Le, H. P. 1998. Progress and trends in ink-jet printing technology. *Journal of Imaging Science and Technology.* **42**(1), pp. 49–62. Cited on p. 3.

Leal, L. G. 1992. *Laminar Flow and Convective Transport Processes: Scaling Principles and Asymptotic Analysis.* Butterworth-Heinemann Series in Chemical Engineering. Cited on pp. 23 and 25.

Lee, T.-M., Kang, T. G., Yang, J.-S., Jo, J., Kim, K.-Y., Choi, B.-O., and Kim, D.-S. 2008. Drop-on-demand solder droplet jetting system for fabricating microstructure. *IEEE Transactions on Electronics Packaging Manufacturing.* **31**(3), pp. 202–210. Cited on p. 1.

Levich, B. and Landau, L. 1942. Dragging of a liquid by a moving plate. *Acta Physicochim. URSS.* **17**, pp. 42. Cited on p. 121.

Li, R., Ashgriz, N., Chandra, S., and Andrews, J. R. 2008. Contraction of free liquid ligaments. *AIChE Journal.* **54**(12), pp. 3084–3091. Cited on pp. 24 and 36.

Liao, Y.-C., Subramani, H. J., Franses, E. I., and Basaran, O. A. 2004. Effects of soluble surfactants on the deformation and breakup of stretching liquid bridges. *Langmuir.* **20**(23), pp. 9926–9930. Cited on pp. 13, 19, and 56.

Liao, Y.-C., Franses, E. I., and Basaran, O. A. 2006. Deformation and breakup of a stretching liquid bridge covered with an insoluble surfactant monolayer. *Physics of Fluids.* **18**(2), pp. 022101. Cited on pp. 13, 19, and 56.

Loshak, J. and Byers, C. H. 1973. Forced oscillations of drops in a viscous medium. *Chemical Engineering Science.* **28**(1), pp. 149–156. Cited on p. 101.

Lucassen, J. and Hansen, R. S. 1966. Damping of waves on monolayer-covered surfaces: I. systems with negligible surface dilational viscosity. *Journal of Colloid and Interface Science.* **22**(1), pp. 32–44. Cited on p. 13.

MacLeod, C. and Radke, C. 1994. Surfactant exchange kinetics at the air/water interface from the dynamic tension of growing liquid drops. *Journal of Colloid and Interface Science.* **166**(1), pp. 73–88. Cited on p. 118.

Mandrycky, C., Wang, Z., Kim, K., and Kim, D.-H. 2016. 3d bioprinting for engineering complex tissues. *Biotechnology advances.* **34**(4), pp. 422–434. Cited on p. 1.

Manikantan, H. and Squires, T. M. 2020. Surfactant dynamics: hidden variables controlling fluid flows. *Journal of Fluid Mechanics.* **892**. Cited on p. 122.

Marangoni, C. 1871. Ueber die ausbreitung der tropfen einer flüssigkeit auf der oberfläche einer anderen. *Annalen der Physik.* **219**(7), pp. 337–354. Cited on p. 80.

Martin, G. D., Hutchings, I. M., and Hoath, S. D. Jet formation and late-stage ligament instability in drop-on-demand printing. In *NIP & Digital Fabrication Conference*, volume 2006, pp. 95–98. Society for Imaging Science and Technology, 2006. Cited on p. 36.

Martin, G. D., Hoath, S. D., and Hutchings, I. M. Inkjet printing-the physics of manipulating liquid jets and drops. In *Journal of Physics: Conference Series*, volume 105, pp. 012001. IOP Publishing, 2008. Cited on pp. 2, 5, 35, and 102.

Matsumoto, T., Nakano, T., Fujii, H., Kamai, M., and Nogi, K. 2002. Precise measurement of liquid viscosity and surface tension with an improved oscillating drop method. *Physical Review E.* **65**(3), pp. 031201. Cited on p. 101.

McGough, P. T. and Basaran, O. A. 2006. Repeated formation of fluid threads in breakup of a surfactant-covered jet. *Physical Review Letters*. **96**(5), pp. 054502. Cited on p. 14.

McKinley, G. H. and Renardy, M. 2011. Wolfgang von ohnesorge. *Physics of Fluids*. **23**(12), pp. 127101. Cited on pp. 8, 9, 37, and 52.

Miller, R., Joos, P., and Fainerman, V. B. 1994. Dynamic surface and interfacial tensions of surfactant and polymer solutions. *Advances in Colloid and Interface Science*. **49**, pp. 249–302. Cited on p. 101.

Milliken, W., Stone, H. A., and Leal, L. 1993. The effect of surfactant on the transient motion of newtonian drops. *Physics of Fluids A: Fluid Dynamics*. **5**(1), pp. 69–79. Cited on p. 13.

Milliken, W. J. and Leal, L. G. 1994. The influence of surfactant on the deformation and breakup of a viscous drop: The effect of surfactant solubility. *Journal of Colloid and Interface Science*. **166**(2), pp. 275–285. Cited on pp. 13 and 118.

Morrison, N. F. and Harlen, O. G. 2010. Viscoelasticity in inkjet printing. *Rheologica Acta*. **49**(6), pp. 619–632. Cited on pp. ii, 6, 24, 26, 36, 58, and 115.

Murphy, S. V. and Atala, A. 2014. 3d bioprinting of tissues and organs. *Nature Biotechnology*. **32**(8), pp. 773–785. Cited on p. 1.

Muzzio, F., Tjahjadi, M., and Ottino, J. M. 1991. Self-similar drop-size distributions produced by breakup in chaotic flows. *Physical Review Letters*. **67**(1), pp. 54. Cited on p. 36.

Nelson, A. R. and Gokhale, N. R. 1972. Oscillation frequencies of freely suspended water drops. *Journal of Geophysical Research*. **77**(15), pp. 2724–2727. Cited on p. 102.

Notz, P. K. and Basaran, O. A. 2004. Dynamics and breakup of a contracting liquid filament. *Journal of Fluid Mechanics*. **512**, pp. 223–256. Cited on p. 36.

Notz, P. K., Chen, A. U., and Basaran, O. A. 2001. Satellite drops: Unexpected dynamics and change of scaling during pinch-off. *Physics of Fluids*. **13**(3), pp. 549–552. Cited on p. 14.

Ohl, C., Tijink, A., and Prosperetti, A. 2003. The added mass of an expanding bubble. *Journal of Fluid Mechanics*. **482**, pp. 271–290. Cited on p. 103.

Ou Ramdane, O. and Quéré, D. 1997. Thickening factor in marangoni coating. *Langmuir*. **13**(11), pp. 2911–2916. Cited on p. 121.

Papageorgiou, D. T. 1995. On the breakup of viscous liquid threads. *Physics of Fluids*. **7**(7), pp. 1529–1544. Cited on p. 11.

Plateau, J. 1873. Experimental and theoretical statics of liquids subject to molecular forces only. Cited on pp. 6 and 7.

Plateau, M. 1856. Xxxvii. on the recent theories of the constitution of jets of liquid issuing from circular orifices. *The London, Edinburgh, and Dublin Philosophical Magazine and Journal of Science*. **12**(79), pp. 286–297. Cited on p. 10.

Prosperetti, A. 1980. Free oscillations of drops and bubbles: the initial-value problem. *Journal of Fluid Mechanics*. **100**(2), pp. 333–347. Cited on pp. 103, 104, and 105.

Quéré, D. 1999. Fluid coating on a fiber. *Annual Review of Fluid Mechanics*. **31**(1), pp. 347–384. Cited on pp. 13, 121, and 122.

Quintans Carou, J., Mottram, N. J., Wilson, S. K., and Duffy, B. R. 2007. A mathematical model for blade coating of a nematic liquid crystal. *Liquid Crystals*. **34**(5), pp. 621–631. Cited on p. 1.

Rayleigh, L. 1878. On the instability of jets. *Proceedings of the London Mathematical Society*. **1**(1), pp. 4–13. Cited on pp. 6, 7, and 10.

Rayleigh, L. 1879. On the capillary phenomena of jets. *Proceedings of the Royal Society of London*. **29**(196-199), pp. 71–97. Cited on pp. 3, 103, and 104.

Rayleigh, L. 1892. Xvi. on the instability of a cylinder of viscous liquid under capillary force. *The London, Edinburgh, and Dublin Philosophical Magazine and Journal of Science*. **34**(207), pp. 145–154. Cited on p. 10.

Robinson, J., Sutton, C., and Reid, G. 2014. Dilute triton x-100 in water as a reference liquid for hydrometer calibration using cuckow's method. *Measurement*. **57**, pp. 132–137. Cited on pp. 76 and 78.

Roché, M., Aytouna, M., Bonn, D., and Kellay, H. 2009. Effect of surface tension variations on the pinch-off behavior of small fluid drops in the presence of surfactants. *Physical Review Letters*. **103**(26), pp. 264501. Cited on p. 14.

Ronay, M. 1978. Determination of the dynamic surface tension of liquids from the instability of excited capillary jets and from the oscillation frequency of drops issued from such jets. *Proceedings of the Royal Society of London. A. Mathematical and Physical Sciences*. **361**(1705), pp. 181–206. Cited on p. 101.

Rosen, M. J. and Kunjappu, J. T. 2012. *Surfactants and interfacial phenomena.* John Wiley & Sons. Cited on p. 13.

Roth, E. A., Xu, T., Das, M., Gregory, C., Hickman, J. J., and Boland, T. 2004. Inkjet printing for high-throughput cell patterning. *Biomaterials.* **25**(17), pp. 3707–3715. Cited on p. 1.

Savart, F. 1833. Mémoire sur la constitution des veines liquids lancées par des orifices circulaires en mince paroi. *Annales de Chimie et de Physique.* **53**, pp. 337–386. Cited on pp. 3 and 10.

Scheid, B., Delacotte, J., Dollet, B., Rio, E., Restagno, F., Van Nierop, E., Cantat, I., Langevin, D., and Stone, H. A. 2010. The role of surface rheology in liquid film formation. *EPL (Europhysics Letters).* **90**(2), pp. 24002. Cited on pp. 13 and 122.

Schulkes, R. 1996. The contraction of liquid filaments. *Journal of Fluid Mechanics.* **309**, pp. 277–300. Cited on p. 36.

Seiwert, J., Dollet, B., and Cantat, I. 2014. Theoretical study of the generation of soap films: role of interfacial visco-elasticity. *Journal of Fluid Mechanics.* **739**, pp. 124. Cited on p. 122.

Shen, A. Q., Gleason, B., McKinley, G. H., and Stone, H. A. 2002. Fiber coating with surfactant solutions. *Physics of Fluids.* **14**(11), pp. 4055–4068. Cited on p. 13.

Smith, W. R. 2010. Modulation equations for strongly nonlinear oscillations of an incompressible viscous drop. *Journal of Fluid Mechanics.* **654**, pp. 141. Cited on p. 105.

Staat, H. J., van der Bos, A., van den Berg, M., Reinten, H., Wijshoff, H., Versluis, M., and Lohse, D. 2017. Ultrafast imaging method to measure surface tension and viscosity of inkjet-printed droplets in flight. *Experiments in Fluids.* **58**(1), pp. 2. Cited on pp. 102 and 103.

Stancik, E. J., Kouhkan, M., and Fuller, G. G. 2004. Coalescence of particle-laden fluid interfaces. *Langmuir.* **20**(1), pp. 90–94. Cited on p. 120.

Stone, H. A. 1990. A simple derivation of the time-dependent convective-diffusion equation for surfactant transport along a deforming interface. *Physics of Fluids A: Fluid Dynamics.* **2**(1), pp. 111–112. Cited on p. 56.

Stone, H. A. and Leal, L. G. 1990. The effects of surfactants on drop deformation and breakup. *Journal of Fluid Mechanics.* **220**, pp. 161–186. Cited on pp. 13 and 56.

Stubenrauch, C., Fainerman, V., Aksenenko, E., and Miller, R. 2005. Adsorption behavior and dilational rheology of the cationic alkyl trimethylammonium bromides at the water/air interface. *The Journal of Physical Chemistry B.* **109**(4), pp. 1505–1509. Cited on p. 118.

Stückrad, B., Hiller, W., and Kowalewski, T. 1993. Measurement of dynamic surface tension by the oscillating droplet method. *Experiments in Fluids.* **15**(4-5), pp. 332–340. Cited on p. 102.

Sykes, T. C., Castrejón-Pita, A. A., Castrejón-Pita, J. R., Harbottle, D., Khatir, Z., Thompson, H. M., and Wilson, M. C. 2020. Surface jets and internal mixing during the coalescence of impacting and sessile droplets. *Physical Review Fluids.* **5**(2), pp. 023602. Cited on p. 120.

Tasoglu, S. and Demirci, U. 2013. Bioprinting for stem cell research. *Trends in Biotechnology.* **31**(1), pp. 10–19. Cited on p. 1.

Tekin, E., Smith, P. J., and Schubert, U. S. 2008. Inkjet printing as a deposition and patterning tool for polymers and inorganic particles. *Soft Matter.* **4**(4), pp. 703–713. Cited on p. 1.

Tian, Y., Holt, R. G., and Apfel, R. E. 1995. Investigations of liquid surface rheology of surfactant solutions by droplet shape oscillations: theory. *Physics of Fluids.* **7**(12), pp. 2938–2949. Cited on p. 103.

Tian, Y., Holt, R. G., and Apfel, R. E. 1997. Investigation of liquid surface rheology of surfactant solutions by droplet shape oscillations: Experiments. *Journal of Colloid and Interface Science.* **187**(1), pp. 1–10. Cited on p. 103.

Timmermans, M.-L. E. and Lister, J. R. 2002. The effect of surfactant on the stability of a liquid thread. *Journal of Fluid Mechanics.* **459**, pp. 289–306. Cited on p. 82.

Tjahjadi, M., Stone, H. A., and Ottino, J. M. 1992. Satellite and subsatellite formation in capillary breakup. *Journal of Fluid Mechanics.* **243**, pp. 297–317. Cited on p. 36.

Trinh, E. and Wang, T. 1982. Large-amplitude free and driven drop-shape oscillations: experimental observations. *Journal of Fluid Mechanics.* **122**, pp. 315–338. Cited on p. 101.

Trinh, E., Marston, P., and Robey, J. 1988. Acoustic measurement of the surface tension of levitated drops. *Journal of Colloid and Interface Science*. **124**(1), pp. 95–103. Cited on p. 102.

Troian, S., Herbolzheimer, E., and Safran, S. 1990. Model for the fingering instability of spreading surfactant drops. *Physical Review Letters*. **65**(3), pp. 333. Cited on p. 13.

van der Bos, A., Zijlstra, A., Gelderblom, E., and Versluis, M. 2011. ilif: illumination by laser-induced fluorescence for single flash imaging on a nanoseconds timescale. *Experiments in Fluids*. **51**(5), pp. 1283–1289. Cited on p. 76.

Velentine, R., Sather, N., and Heideger, W. 1965. The motion of drops in viscous media. *Chemical Engineering Science*. **20**(8), pp. 719–728. Cited on p. 102.

Verbist, G., Weaire, D., and Kraynik, A. 1996. The foam drainage equation. *Journal of Physics: Condensed Matter*. **8**(21), pp. 3715. Cited on p. 123.

von Szyszkowski, B. 1908. Experimentelle studien über kapillare eigenschaften der wässerigen lösungen von fettsäuren. *Zeitschrift für Physikalische Chemie*. **64**(1), pp. 385–414. Cited on p. 19.

Westborg, H. and Hassager, O. 1989. Creeping motion of long bubbles and drops in capillary tubes. *Journal of Colloid and Interface Science*. **133**(1), pp. 135–147. Cited on pp. 26 and 28.

Wijshoff, H. 2010. The dynamics of the piezo inkjet printhead operation. *Physics Reports*. **491**(4-5), pp. 77–177. Cited on p. 102.

Wong, C. 1976. Limits of the nuclear viscosity coefficient in the liquid-drop model. *Physics Letters B*. **61**(4), pp. 321–323. Cited on p. 102.

Xu, Q., Liao, Y.-C., and Basaran, O. A. 2007. Can surfactant be present at pinch-off of a liquid filament? *Physical Review Letters*. **98**(5), pp. 054503. Cited on p. 82.

Yang, L. and Bain, C. D. Liquid jet instability and dynamic surface tension effect on breakup. In *NIP & Digital Fabrication Conference*, volume 2009, pp. 79–82. Society for Imaging Science and Technology, 2009. Cited on pp. 74 and 78.

Yang, L., Kazmierski, B. K., Hoath, S. D., Jung, S., Hsiao, W.-K., Wang, Y., Berson, A., Harlen, O., Kapur, N., and Bain, C. D. 2014. Determination of dynamic surface tension and viscosity of non-newtonian fluids from drop oscillations. *Physics of Fluids*. **26**(11), pp. 113103. Cited on pp. 74, 102, and 103.

Young, T. et al. 1805. Iii. an essay on the cohesion of fluids. *Philosophical Transactions of the Royal Society of London.* **95**, pp. 65–87. Cited on p. 9.

Zoltan, S. I. Pulsed droplet ejecting system, Aug. 8 1972. US Patent 3,683,212. Cited on p. 4.